VISIONS•SCIENCE•TECHNOLOGY•RESEARCH HIGHLIGHTS

Dissertation
14

Microsystems for Biological Cell Characterization

Anna Rissanen

VTT SCIENCE 14

Microsystems for Biological Cell Characterization

Anna Rissanen

Thesis for the degree of Doctor of Science in Technology to be presented with due permission of the School of Electrical Engineering for public examination and debate in Auditorium S1 at Aalto University (Espoo, Finland) on the 19th of October, 2012, at 12 noon.

ISBN 978-951-38-7475-9 (soft back ed.)
ISSN 2242-119X (soft back ed.)

ISBN 978-951-38-7931-0 (URL: http://www.vtt.fi/publications/index.jsp)
ISSN 2242-1203 (URL: http://www.vtt.fi/publications/index.jsp)

JULKAISIJA – UTGIVARE – PUBLISHER

VTT
PL 1000 (Tekniikantie 4 A, Espoo)
02044 VTT
Puh. 020 722 111, faksi 020 722 7001

VTT
PB 1000 (Teknikvägen 4 A, Esbo)
FI-02044 VTT
Tfn +358 20 722 111, telefax +358 20 722 7001

VTT Technical Research Centre of Finland
P.O. Box 1000 (Tekniikantie 4 A, Espoo)
FI-02044 VTT, Finland
Tel. +358 20 722 111, fax + 358 20 722 7001

Kopijyvä Oy, Kuopio 2012

Microsystems for Biological Cell Characterization

[Mikrosysteemit solujen karakterisointiin]. **Anna Rissanen.** Espoo 2012. VTT Science 14. 130 p.

Abstract

This thesis describes three techniques for the characterization of living cells using micro-electro-mechanical systems (MEMS) based devices. The study of cellular function and structure is essential for bioprocess control, disease diagnosis, patient treatment and drug discovery. Microsystem technology enables characterization of very small samples, minimal use of expensive reagents, testing of multiple samples in parallel, and point-of-care testing, all of which increase throughput and reduce the analysis cost. The three characterization techniques presented in this thesis could be integrated into a microfluidic cellular total analysis system to obtain complementary information of cellular function.

The first part of the thesis presents the characterization of bovine adrenal cortex capillary endothelial cells by impedance spectroscopy in a microsystem which was realized using microfabrication techniques. The microsystem consists of a small-volume cell culture area defined on PDMS walls on a glass substrate with gold electrodes coated with a self-assembled monolayer to enable cell attachment. As the main result, it was possible to monitor the capillary formation of BACC endothelial cells in a microsystem using impedance spectroscopy.

The second part describes calorimetric characterization of *Saccharomyces cerevisiae* yeast cells using a MEMS-based nanocalorimetric microsensor. The cells are introduced to the sensor membrane in small droplets (~1 µl), and the sensor thermopile voltage output is compared to the output of the reference water droplet to extract the effect of sample evaporation.

The third part describes the design, process integration and fabrication of an electrically tunable Fabry-Perot interferometer (FPI) monolithically integrated on a photodiode for visible spectrum measurements. The options for the process integration of separate FPI optical filters are presented. The application of miniature spectrometers based on MEMS FPI technology in biological cell characterization is discussed.

Keywords BioMEMS, impedance spectroscopy, MEMS nanocalorimeter, Fabry-Perot interferometer, microspectrometers, *Saccharomyces cerevisiae*, yeast, cell measurement

Mikrosysteemit solujen karakterisointiin

[Microsystems for Biological Cell Characterization]. **Anna Rissanen.** Espoo 2012.
VTT Science 14. 130 s.

Tiivistelmä

Tämä väitöskirja käsittää kolme erilaista mikroelektromekaanisiin systeemeihin (MEMS) perustuvaa menetelmää elävien solujen karakterisoimiseksi. Solutoimintojen ja rakenteen karakterisointi on tärkeää bioprosessien kontrolloinnissa, sairauksien diagnosoinnissa, potilaiden hoidossa ja uusien lääkkeiden tutkimuksessa. Mikrosysteemitekniikka mahdollistaa hyvin pienien näytemäärien yhtäaikaisen karakterisoinnin ja paikan päällä testauksen sekä minimoi kalliiden reaktioaineiden käytön, lisäten näin läpimenoa ja vähentäen analyysin hintaa. Nämä kolme tässä väitöskirjassa esitettyä karakterisointitekniikkaa on mahdollista yhdistää osaksi mikrofluidistista solujen kokonaisanalyysisysteemiä ja saada näin toinen toistaan täydentävää mittausinformaatiota solujen toiminnoista.

Ensimmäinen osa käsittää naudan lisämunuaiskuoren kapillaariendoteelisolujen (BACC) monitoroinnin impedanssispektrometrialla mikrosysteemissä, joka on toteutettu mikrotyöstötekniikoita käyttäen. Mikrosysteemi koostuu pienen tilavuuden PDMS (polydimetyylisiloksaani) seinillä rajatusta soluviljelyalueesta lasialustalle, johon on kuvioitu kultaelektrodit ja SAM-kalvo solujen kiinnittymisen mahdollistamiseksi. Keskeisenä tuloksena voitiin todeta, että BACC-endoteelisolujen kapillaarien muodostumista oli mahdollista monitoroida mikrosysteemissä käyttäen impedanssispektrometriaa.

Toisessa osiossa kuvataan *Saccharomyces cerevisiae* -hiivasolujen kalorimetristä monitorointia käyttäen nanokalorimetristä MEMS-mikroanturia. Solut tuodaan anturille pienissä pisaroissa (~µl) ja anturin termoparin jänniteulostuloa verrataan referenssinestepisaran jännitteeseen, jotta haihtumisen aiheuttama lämpöhäviö voidaan kompensoida.

Kolmas osio käsittää näkyvän valon spektrin mittaamiseen tarkoitetun monoliittisesti fotodiodille integroidun sähköisesti säädettävän Fabry-Perot-interferometrin (FPI) suunnittelun, prosessi-integraation ja valmistuksen. Myös erillisten FPI-suodattimien prosessi-integraation vaihtoehdot esitetään. Mikromekaanisiin FPI-suodattimiin perustuvien miniatyyrispektrometrien soveltamista biologisiin solumittauksiin käsitellään ja havainnollistetaan esimerkein.

Avainsanat BioMEMS, impedance spectroscopy, MEMS nanocalorimeter, Fabry-Perot interferometer, microspectrometers, *Saccharomyces cerevisiae*, yeast, cell measurement

Preface

This thesis is a *monograph*, however, parts of the thesis are based on own publications [1]–[6] with related work also in [7] and [8]. The objectives, organization and author's contribution are presented in more detail in Chapters 1.2–1.4. The reason for choosing this book format over the more commonly used article dissertation is in the structure of the work presented in this thesis; the topic is highly interdisciplinary in scope, covering a very broad range of systems and methods. With this monograph format, I wanted to bring more focus into the study.

I started my career as a researcher at VTT in 2003 and since then, most of my project work has been related to surface micro(opto)electromechanical sensor (MEMS) research and process development, including structural design and fabrication process integration. However, on the side of my main work activities, I've also had opportunities to cross the disciplines of MEMS and biology, these explorations forming the backbone of this thesis. Realizing this work within a research team that does not specialize in BioMEMS has been a challenge that I have embraced and enjoyed, although it has also proven to be a time-consuming choice. While there are those who prefer narrow, focused research topic, that is not my approach. My hope is that this work will succeed in showing the range of advantages and disadvantages of the chosen MEMS-based characterization methods, including electrical, thermal and optical characterization of cells. When talking about micro total analysis systems, I believe that the use of multiple research methods is more than justified by the complementary knowledge gained in return. This said, I wish to thank the pre-examiners Prof. Ellis Meng and Prof. Jukka Lekkala for their dedicated work. Based on their review and feedback I think I may have achieved my goal.

These two pages are a unique opportunity to express gratitude and there are many people I wish to thank for these past years, starting from my instructor Prof. Sami Franssila and supervisor Prof. Ilkka Tittonen. You gave me the first inspiration around year 2000 to get into the field of micromachining and your guidance extends several years back to the time of my undergrad studies. Without your comments and support on times of doubt, this thesis would not have been finished. I would like to thank Rec.Prof. Hannu Kattelus for believing in me back in 2003 and giving me the chance to work at VTT, supporting me in both my M.Sc. thesis and later in my choice of topic for the doctoral thesis. I wish to acknowledge Päivi Heimala, the pioneer and the corner stone of bioresearch within microelectronics at VTT, thank you for your encouragement and support. I also wish to thank Prof. Fujii and all the Fujita lab members and co-authors for their advice and support with cell impedance measurements and the interdisciplinary times in Japan back in year 2004.

Furthermore, I would like to thank several colleagues at VTT, including "father of the FPIs" Martti Blomberg, who got me hooked on the possibilities of surface micromachining, as well as Mari Laamanen, Mikko Tuohiniemi and Meeri Partanen for willingness to share their exceptional knowledge with me. Thanks to Jarkko Antila for bringing enthusiasm and purpose into the world of FPIs; thanks also to the rest of the "fellowship of the fabry" upstairs, including Heikki Saari, Uula Kantojärvi, Rami Mannila, Altti Akujärvi, Christer Holmlund and others, for our discussions covering ideal FPIs, toilet bowl cameras, flying ball grills and basically any good/bad/strange ideas. Thanks to Jaakko Saarilahti and Ari Häärä for guidance on calorimetric measurements and Kai Kolari for support. Thanks to our ALD expert Riikka Puurunen and our plasma etch guru James Dekker. Thanks to Panu Pekko for answering all kinds of stupid questions over the years and letting me steal chip boxes all the time. Thanks to Heini Saloniemi for countless HF etchings and for cleaning up of the mess of my broken FPI membranes. Thanks to Philippe Monnoyer, Heikki Viljanen, Pradeep Dixit, Gao Feng and all the rest of the colleagues in our center for encouragement and excellent lunch discussions. Last but not the least, thank you Jyrki Kiihamäki for kicking me in the butt to finish this book, I really appreciate you taking interest in the work and supporting me. To summarize, I've been lucky to work with the most delightful and supporting people for the past 10 years, with willingness to help others no matter how busy they are.

Finally, I would like to thank my family, friends and relatives. Laura, you made me believe in going through with this in the first place. My husband Jaakko, thank you for everything. Building a house for us and finishing a thesis are tough projects to fit within the same year. Your patience and calmness completes the shortcomings of my mind. Thanks to my sons for taking interest in my work while writing late evenings at home – Niilo for giving good suggestions on what kind of devices should be made and Eemil (at age 4) for getting inspired to write his own "papana-thesis". Thanks to my sisters Ellu and Kata for the tear laughs over the years and to my extended family Simmerman for giving me the chance to get inspired about sciences in the most unique engineering environment one can imagine (volcanoes of Hawaii). Kiitos Mummi, also remembering Vaari, a dedicated self-learner who built an engineering business & factory on his own. Thanks to Äiti and Isä for putting up with a strong-headed daughter with a lot of good and not so good ideas, for letting me climb my bear mountains and dive the oceans.

Espoo, August 2012

Anna Rissanen

Academic Dissertation

Supervisor Professor Ilkka Tittonen
Micro and quantum systems
Department of Micro- and Nanosciences
Aalto University, School of Electrical Engineering, Finland

Instructor Professor Sami Franssila
Microfabrication
Department of Materials Science and Engineering
Aalto University, School of Chemical Technology, Finland

Reviewers Professor Jukka Lekkala, Head of Dep.
Department of Automation Science and Engineering
Tampere University of Technology, Finland

Professor Ellis Meng
Biomedical Microsystems Laboratory
USC University of Southern California
California, United States

Opponent Professor Pasi Kallio
Micro- and nanosystems research group
Department of Automation Science and Engineering
Tampere University of Technology, Finland

.

Contents

List of abbreviations

11-MUA	11-Mercaptoundecanoic acid
AC	Alternating current
Al	Aluminium
ALD	Atomic layer deposition
BACC-EC	Bovine adrenal cortex capillary endothelial cell
BioMEMS	MEMS for biological applications
BSA	Bovine serum albumin
DEP	Dielectrophoresis
DI	Deionized
CFU	Cell fermentation unit
CTE	Coefficient of thermal expansion
DMEM	Dulbecco’s modified Eagle’s medium
DTS	Dodecyltrichlorosilane
ECFP	Enhanced cyan fluorescent protein
EDTA	Ethylenediaminetetraacetic acid
EG-VEGF	Endocrine gland-derived vascular endothelial growth factor
EHP	Electron-hole pair
EIS	Electrical impedance spectrometry
EP	Electrode pair
EtOH	Ethanol
EYFP	Enhanced yellow fluorescent protein
FBF	Fibroblast growth factor
FBS	Fetal bovine serum
FPI	Fabry-Perot interferometer
FSR	Free spectral range
FT-IR	Fourier transform infrared
FWHM	Full width at half maximum
GFP	Green fluorescent protein

HDT	Hexadecanethiol
HEPES	4-(2-hydroxyethyl)-1-piperazineethanesulfonic acid
HUVEC	Human umbilical vein endothelial cell
IC	Integrated circuit
IPA	Isopropanol
IR	Infrared
LIF	Laser induced fluorescence
LOC	Lab-on-a-chip
MEMS	Micro-electro-mechanical systems
MOEMS	Micro-opto-electro-mechanical systems
NDIR	Non-dispersive infra-red
NEAA	Non-essential amino acid
OTS	Octadecyltrichlorosilane
PBS	Phosphate-buffered saline
PDMS	Polydimethylsiloxane
PRS	Photoresist stripper (O_2 plasma)
QA/QC	Quality assurance / Quality control
rHuEPO	Recombinant human EPO
RIE	Reactive ion etching
SAM	Self-assembled monolayer
Si	Silicon
SiN_x	Silicon nitride, non-stoichiometric
UV	Ultraviolet
VEGF	Vascular endothelial cell growth factor
Vis	Visible
µTAS	Micro total analysis systems

List of symbols

∅	Diameter
A	Absorbance
A_c	Area of the capacitive plates
b	Path length
c	Concentration
c_0	Variable capacitance of the original actuator
c_1	Series capacitance
C	Capacitance
C_c	Capacitive part of the cell layer
C_h	Heat capacity
C_{me}	Capacitance at the medium/electrode interface
d	Distance
e	Molar absorptivity
E_g	Band-gap energy
F	Coefficient of finesse
G	Heat conductance of the thermopile
n	Refractive index
n_j	Refractive index of a layer in Bragg mirror
n_H	High refractive index
n_L	Low refractive index
n_S	Refractive index of substrate
N_F	Reflection finesse
k	interference order
K	Responsivity (V/W)
K_l	Linear spring constant
L_j	Thickness of a layer in Bragg mirror
M_1	Mirror 1 of the Fabry-Perot interferometer
M_2	Mirror 2 of the Fabry-Perot interferometer

P	Thermal power
q	Quantity of heat
R_{cap}	Capillary ratio
R_{conf}	Confluence ratio
R	Reflectance
R_m	Resistance of the culture medium
R_c	Resistive part of the cell layer
R_{ct}	Charge transfer resistance
S	Seebeck coefficient
T	Transmittance
V_o	Output voltage
V_{o1}	Output voltage of the cell droplet
V_{o2}	Output voltage of a reference water droplet
V_a	Applied voltage
V_{PI}	Pull-in voltage
Y	Optical admittance
Z	Impedance
Z'	Real part of impedance
Z''	Imaginary part of impedance
Z_w	Warburg impedance
α	Angle of incoming light
δ	Phase difference
ε_c	Calibration constant
ε_0	Permittivity of the free space
λ	Wavelength
λ_c	Cut-off wavelength
τ	Time constant
ϕ	Phase

1. Introduction

This thesis is an interdisciplinary work ranging in scope from the optical, electrical and materials science of microelectromechanical systems (MEMS) and sensor measurement technology to cell biology. In addition, the devices and characterization methods also represent different technologies and approaches. The first chapter describes the background of the field of MEMS and its application in biological research and explains the composition of this work**,** which aims to underline the common purpose of the used MEMS devices and technologies and how they can complement one another.

1.1 Background

1.1.1 MEMS

Microfabrication and the emergence of microelectromechanical systems (MEMS) have their background in the fabrication technologies developed for processing silicon for the integrated circuit (IC) industry. The IC industry has utilized microfabrication technologies to reduce the size of transistors by narrowing CMOS gate widths, thus enabling the development of high capacity devices with minimal space requirements. Other devices based on the ability to control the conductivity of silicon include photodiodes and photodetectors. MEMS devices, on the other hand, take advantage of the mechanical properties of silicon. Besides electrical functions, MEMS devices usually contain moving parts that allow physical or analytical functions to also be performed. This facilitates the development of microsensors that transform physical or chemical signals from the environment to electrical form. The moving membrane of a MEMS microphone transforms speech whereby the sealed membrane of a MEMS pressure sensor bends according to the air pressure and the resonating structures of force or acceleration sensors respond to the change in velocity. These vibrations or structural movements can, in turn, be read as an electrical signal generated between thin conductive films incorporated into the structures, taking advantage of, for instance, structure capacitance or piezoresistive phenomena.

Microfabrication consists of adding and removing material selectively layer by layer to obtain a complete device structure. Techniques such as thin film deposition, photolithography, etching and bonding are used to create different types of structures such as membranes, cantilevers, valves, vias and reservoirs. The traditional substrate for the MEMS fabrication process is silicon, although new substrate materials used include quartz or fused silica. Depending on the material used in the functional part of the device, two different types of MEMS processing approaches exist: "bulk MEMS" consisting moving parts made of silicon, and "surface MEMS" consisting of functional structures made out of thin films deposited on the substrate. Modern microfabrication techniques allow extremely precise and repeatable processing of features ranging from nanometres to several millimetres in size. MEMS originated in electro-mechanics, but have since been developed for a number of fields of application to include, for example, optical, acoustic, thermal and fluidic MEMS.

1.1.2 BioMEMS and micro total analysis systems (µTAS)

During the last decade there has been growing interest in the use of MEMS in biological applications (BioMEMS). BioMEMS can be categorized into several different fields of interest, such as microfluidics (sample delivery and sorting methods, channels and droplet control), *in vivo* applications (drug delivery, immunoisolation capsules, implants), biosensors (sensors combining biological elements such as antibodies or enzymes to produce the signal, which the sensor converts to electrical form) and microsystems for bioanalytical purposes, referred to as micro total analysis systems (µTAS) or Lab-on-a-chip (LOC). The work reported in this thesis focuses on a subsection of this last category, namely MEMS-based characterization and detection methods that can be used as a part of microfluidic analysis systems due to their miniaturized size. Although fluidic transportation and several types of analysis steps have been miniaturized into Lab-On-Chip devices, many of the employed characterization methods are still in macroscopic form.

Microfluidic systems are miniaturized platforms for chemical and biological research which utilize microfabrication technology to build channels, valves and structures for liquid pumping and flow handling, sample sorting and analysis. The purpose is to integrate laboratory analysis steps such as sample preparation, injection, separation and detection into a single automated device that can perform several functions without human interference. Besides chemical analysis, these devices are suitable for cell analysis, which also requires many sampling and preparation steps (cell sorting, handling, trapping, lysis and analysis). Cell behaviour can thus be studied from single to multi cellular level with precise control of the liquid flow on a micron scale, as well as individual cell handling and manipulation.

The advantage of using MEMS technology for bioanalytical purposes is based on several key aspects. The size and dimensions of MEMS devices is in the same order as that of biological components which, for example, enables the fabrication of devices with physical dimensions the size of cells (10–100 µm). Analysis can be performed in the microenvironment with rapid heat and mass transfer, utilizing extremely small sample and reagent volumes, thus leading to reduced analysis cost.

Several types of microfluidic devices for cell manipulation, treatment and analysis have been introduced during the last decade. The first microfluidic devices were based on silicon microfabrication technology for creating fluid control and transport systems, but since the late 90s and the introduction of soft-lithography and polymer moulding, PDMS has become a popular material in microfluidic devices for cellular research due to its biologically favourable characteristics, such as biocompatibility, transparency and gas permeability [9, 10]. Devices for microfluidic cell manipulation consist of sampling devices (microneedles), trapping and sorting methods using electrical and mechanical filtering techniques, and cell treatment devices for cell lysis and culturing. The term ‘micro total analysis system’ also refers to the integration of sensors and measurement technology in these devices [11]. However, based on the number of published papers covering microfluidics and on the common detection methods used (Figure 1), the focus of research has been on the creation of microfluidics and less on detection and monitoring methods. The topic of this thesis work is therefore highly relevant.

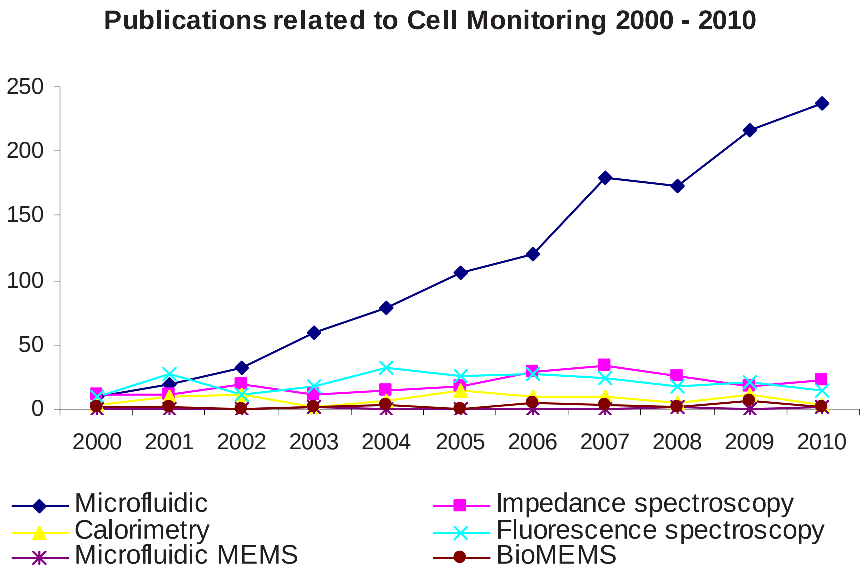

Figure 1. Number of publications containing related search keywords, and related words (cell or tissue or monitoring), excluding fuel and solar cells and atomic and mass spectroscopy from the search results. The search included all major journal databases, such as Wiley, Springer, IEEE, Elsevier and Web of Science.

MEMS-based analysis and monitoring methods have several advantages. Many laboratory bench top analyzers are expensive and their use is therefore limited. Due to the mass production capability of MEMS, measurement devices can be made with low cost but excellent accuracy. In addition, their use is simple in small, portable hand-held devices. The cost of analytical devices integrated into microfluidic systems for cellular analysis can also be made very low, facilitating single-use LOC analyzers. Several different types of measurement and analysis methods can be used simultaneously, adding more versatility to the sample analysis.

Besides analysis in the microenvironment, such as impedance monitoring of cell cultures using device sizes in the order of cell capillaries, as described in this thesis, utilizing MEMS devices for the analysis of cells in the macroscopic environment is also of great interest. In this work, a MEMS device suitable for optical monitoring of biological samples in both the micro- and macroscopic environments is introduced. In the analysis of macro-scale biological samples, such as in the biopharma, biofuel or food production industries, using small and inexpensive MEMS-based sensors facilitates better process control and efficiency due to improved real-time on-line/in-situ monitoring capability [12].

The focus of this thesis is on exploring and developing new MEMS-based characterization or monitoring techniques that can be applied to cell measurement, ranging from electrical and thermal characterization to optical measurements, and on discussing their individual advantages and drawbacks.

1.2 Objectives and organization of the thesis

This thesis is a *monograph*, however, parts of the thesis have been published in [1]–[6], with related work also presented in [7] and [8]. The objective of this thesis was to seek answers for the two main research questions, “Can MEMS-based miniaturized systems and devices provide new complimentary ways of characterizing cells?” and “What are the advantages and disadvantages of these characterization methods?” To serve this purpose, this work introduces microsystems that use different types of characterization techniques for cell analysis and monitoring. The primary focus is on MEMS technology and less on cell biology or measurement science. An overview of the three different characterizations techniques – impedance spectrometry, microcalorimetry and spectroscopy – is presented in Chapter 2.

Experimental work on the three microsystems used for the analysis is presented in Chapters 3 to 6:

Chapter 3 presents the characterization of bovine adrenal cortex capillary endothelial cells by impedance spectroscopy in a microsystem realized using microfabrication techniques. The chapter covers the cell culture experiments, device fabrication, measurements, and analysis of the results.

Chapter 4 describes the calorimetric characterization of *Saccharomyces cerevisiae* yeast cells in using a MEMS-based nanocalorimetric microsensor, with measurements and analysis of the results.

Chapter 5 presents the optical and mask layout design, process integration and fabrication details of an electrically tunable monolithically integrated Fabry-Perot interferometer (FPI), discusses alternative process integration methods to fabricate separate FPIs, and introduces miniaturized spectrometers based on MEMS FPI filters for visible spectrum measurements. The application of the miniature spectrometers to biological cell characterization is discussed and spectral imaging of *Saccharomyces cerevisiae* is demonstrated.

In Chapter 6, a summary and discussion on the scope of the thesis is given.

1.3 Contribution of the thesis

This work contributes to the advancement of microsystems used for cell measurement in the following ways:

- Important cell characterization techniques are reviewed.
- A device capable of successfully maintaining and measuring a culture of adrenal cortex capillary endothelial cells is presented for the first time. It is demonstrated that the capillary formation of the cells can be detected in the measured impedance spectrum. This has important potential applications in drug research where proliferating cancer cells are investigated.
- A thermal nanocalorimetric MEMS sensor is utilized to measure the heat production of *Saccharomyces Cerevisiae* yeast cells for the first time. As reliable thermal measurement of small samples is highly challenging in practice, the present analysis of the issues affecting the measurement is relevant. Improvements in microsystem measurement repeatability are also proposed.
- A novel electrically tunable microspectrometer for the visible spectrum is realized, consisting of a monolithically integrated Fabry-Perot interferometer (FPI) on a photodiode. Also, a separate Fabry-Perot interferometer filter structure is realized using polyimide as the sacrificial layer.
- The potential of MEMS FPI-based biological spectral imaging is discussed and illustrated.
- The presented devices have numerous important applications in biological measurement where fluorescence is used to detect genes, proteins and various intracellular phenomena. They have the potential to replace the expensive spectroscopy equipment used by biologists and the pharmaceutical industry and to add increasing flexibility to the monitoring of biological processes.

1.4 Author’s contribution

The writing of this thesis, including theoretical considerations and analysis of the measurement results, was done solely by the author. In Chapter 3, the device for cell impedance measurements was designed and fabricated by the author with guidance from Vincent Senez and Erwan Lennon (CNRS/IIS). All the experimental work including cell culturing, impedance measurement and the analysis of the results was performed solely by the author. Planning and setting up of the impedance measurement system was done by Vincent Senez and the design of the cell culture protocol was done with guidance from Serge Ostrovidov (CNRS/IIS). The self-assembled monolayers for cell adhesion tests were provided by Prof. Beomjoom Kim (IIS).

In section 4, the planning and execution of cell measurements using a thermal MEMS sensor and the analysis of the results were performed solely by the author. The MEMS sensor and the measurement set up were designed and provided by Jaakko Saarilahti (VTT).

In section 5, the author has drawn the mask layers, designed the processing steps and overseen the microfabrication process for integrating the Fabry-Perot interferometer (FPI) on a photodiode with guidance from Martti Blomberg and Simo Eränen (VTT). The author has also drawn the mask layers, designed and overseen the microfabrication process for separate FPIs, with guidance from Martti Blomberg. The presented optical simulations for the FPIs have been created by the author. The miniature spectrometers (including software and calibration) were developed by Jarkko Antila’s team (VTT), with the author acting as a project leader responsible for realizing the pen spectrometer and providing the FPIs for the imaging spectrometer. The spectral imaging measurements were performed by the author.

2. Characterization techniques

Impedance spectroscopy, microcalorimetry and fluorescence measurements are among the most versatile cell characterization techniques that can be applied to microfluidic environments. This section gives a general overview of these three characterization methods and a short review of how they have been applied at the micro scale. The section begins with an introduction to the current characterization methods used in microfluidic analysis systems.

2.1 Cellular characterization methods employed in µTAS

Microscope imaging and fluorescence microscopy are among the most commonly used laboratory methods for studying cell cultures. However, supplementary information on the state and viability of cells can be obtained by applying MEMS-based analysis methods. In recent years, micro total analysis systems have made it possible to culture, treat, manipulate and analyze cells in microenvironments using a range of detection methods. It is an ongoing effort to integrate more analysis and characterization methods into these systems to obtain multifunctional platforms for cellular analysis. To this end, MEMS sensors offer the advantage of small size, low cost and reliable performance.

In order to give an overview of the field of BioMEMS and microfluidic analysis systems, selected high-impact review articles and their approach to this field of research are discussed. This reveals the balance between how much research emphasis is currently invested in microfabrication technologies for the development of channels, sorters, traps and other similar structures intended for the handling of the cells or fluids, and the amount of research being conducted on characterization and detection methodology.

BioMEMS covers a wide range of functional and measurement devices. As mentioned in the first chapter, one branch in the field is the development of physiologically integrated devices for drug encapsulation and delivery, which require implantation and biocompatibility. Grayson et al. have produced a comprehensive review of implantable MEMS and actuation systems, also covering surface modification issues and biocompatibility of MEMS [13]. Biocompatibility is an issue with all cell-based devices, but in this section more detailed attention is given to micro total analysis systems and the characterization methods employed.

Several high quality reviews have been written on cellular µTAS offering various perspectives on the subject. El-Ali et al. report on the extracellular matrix and the possibilities to observe cellular interaction within the microsystem due to the spatial and temporal control and stimuli provided by the microculture environment [14]. They focus more on issues related to cell culturing and handling and less attention is given to analysis and detection methods.

Andersson and van den Berg address the microsystem technologies dedicated to single-cell analysis [15]. As single cell handling within a microsystem requires different handling techniques compared to cell culturing, Andersson and van den Berg cover dielectrophoresis, electrophoresis and optical trapping as ways to manipulate single cells. They also address the electrical, mechanical and optical characterization of single cells, which also have different requirements in terms of sensitivity compared to the characterization of cell cultures and tissues and are thus limited to electrical patch clamp systems [16]–[17] and optical tweezers [18]. Andersson et van den Berg also address the most common microdevices for cellular studies in another article [19] which reviews the common processing and handling techniques for cell sampling, trapping, sorting, transporting and cultivating.

Cell sorters on microchips can utilize different detection and manipulation methods, one of the most common being fluorescence (fluorescence activated cell sorters, FACs) [20]. Cell manipulation in these microfluidic devices is achieved by utilizing different types of forces. Magnetic manipulation utilizes magnetic particles attached to the cells [21–22], optical manipulation utilizes optical tweezers [23], mechanical manipulation utilizes different types of microstructures (filters, microwells, channels), and electrical manipulation utilizes dielectrophoresis (DEP) [24]. Yi et al. review these different cell manipulation methods in their article [25], categorizing the microsystems based on cell manipulation technique, treatment (lysis, culture and electroporation) and analysis (flow cytometers, electrical characterization, whole cell assays).

These review articles cover hundreds of different microsystems for cell analysis, but their emphasis is overwhelmingly on cell handling and manipulation methods. Less research seems to have been conducted on integrated measurement and characterization methods, the most commonly mentioned of these being structures for patch-clamp, electroporation and lysis. Electroporation is a common method applied in gene transfection and cell lysis, where voltage applied across the cell (in a patch-clamp electrode system) opens up the ionic channels of the cell membrane. This allows the extraction and analysis of the internal contents of the cells, even at the single-cell level. However, this analysis method kills the cells, which limits it application (not an on-line analysis tool).

Y. Tanaka et al. also review cell culture microsystems and single-cell analysis systems, but go further by examining the promising field of bio-microactuators, which exploit the mechanical properties of cells (contractile force) for different types of applications (fluid pumping and actuation, muscle robots) [26]. As regards characterization and detection methods, Tanaka et al. mention the less common force sensors for determining the contractile force of a single rat cardiomyocyte [27] as well as the scanning thermal lens microscope [28], which was applied to detecting NO release in a cell culture on a glass substrate.

Erickson et al. review the common sorting and manipulation devices, but also examine integrated devices with chemical analysis and detection [29]. The examined systems consisted mainly of enzyme-modified electrodes for monitoring glucose, lactate, glutamine and glutamate [30–32]. Besides general chemical analysis, this method is also suitable for *in vivo* monitoring of cells. Optical sensing elements based on the integration of microchannel systems on CMOS imaging chips have also been developed by Adams et al. [33]. Here, an LED light source at $\lambda = 588$ nm was used together with a commercial CMOS imaging sensor with a fixed wavelength dielectric $SiO_2/S_{i3}N_4$ 7-layer quarter wavelength filter stack for absorption spectroscopy measurement of the microchannels. Such a miniaturized microfluidic set-up described by Adams et al. could be significantly improved with the tunable optical MEMS FPI filter system described in this thesis, allowing multiple wavelength fluorescence measurements to be performed. Other integrated optical structures for microfluidic systems include 2D PDMS lenses for improved fluorescence detection sensitivity [34] and low-loss optical waveguides for time-correlated single-photon counting of fluorescent molecules [35].

A more recent review (2010) of microfluidic tools by Velve-Casquillas et al. [36] summarizes the microfluidic technologies that allow microenvironmental control, discussing laminar flow, PDMS micromoulding technologies, mechanical cell measurements (force), temperature control as well as the commonly employed manipulation techniques (EP, DEP, micro-electroporation/lysis) and cell culturing techniques (medium renewal). As a detection method, only electrical measurements, such as amperometric measurement (enzyme/ion selective electrodes) and impedance spectroscopy, are described. Two articles of particular interest are that of Liu et al., describing the use of impedance measurement to detect the germination of spores [37], and Varshney et al., exploring the potential for detecting bacteria in food samples [38].

Another recently published review article (2010) on the latest developments in microfluidic cell biology and analysis by Salieb-Beugelaar et al. [39] provides a thorough look at the last two years in the field, starting with microfabrication techniques (2D PDMS environments [40]) and surface modification techniques (tetra(ethylene glycol) undecane thiol/hexadecanethiol SAMs for attaching fibroblasts to gold surfaces [41]) which resemble the SAM technique presented in this thesis and published in 2003 [1], moving on to the standard microfluidic topics of flow control, cell cultivating, reactors and mixers, cell manipulation (electroporation, transportation, lysis), cell counting, flow cytometry, separation, as well as sorting and trapping of cells. Up to this point, the Salieb-Beugelaar et al. review article contains 138 citations, whereas the last section of the review dealing with detection contains just 14 citations, accounting for only 9% of the total cited publications mentioned in the article. Of the novel detection methods described, three are based on impedance spectroscopy (distinguishing spermatozoa from HL-60 cells [42] and detecting bacteria *E. coli* [43] and audio frequency for real-time measurement of volume changes [44]. Other described methods include amperometric detection of catecholamines from bovine chromaffin cells [45], chemiluminescence detection of single human blood cells [46] as well as integrated optical sensors for glucose and oxygen uptake [47]. On less common methods, aptamers and surface plasmonics were used for label-free detection of secreted growth factors [48] and the microwave interferometric system for detection of capacitance changes [49].

There are several further examples of the use of cell monitoring techniques left outside of these review articles that deserve attention. Charvin et al. used fluorescence imaging to monitor *Saccharomyces cerevisiae* for more than eight division cycles at the single-cell level. The device consists of a microfluidic platform with a membrane that inhibits piling of the cells, imaged with a digital camera. The system can be used to directly measure the amount and duration of any fluorescent signal-transduction or gene-induction response and allows direct correlation of cell history or cell cycle position with the measured response [50]. The imaging spectrometer developed in this thesis is a miniaturized version of such a detection system which helps bring down the cost of analysis and enables multiple assay-type imaging systems to be built for similar types of cell monitoring activities.

Funfak et al. [51] give another example of fluorescence-based detection in a microfluidic system, describing the use of polymer microparticles with immobilized fluorescent pH-sensitive dye for the monitoring of pH during cell cultivation. Funfak et al. claim that, in contrast to dissolved indicator dyes, the chemical interference of the sensor particles with the surrounding solution is negligible. For the excitation, they used LED at $\lambda = 480$ nm and fluorescence emission detection at a fixed wavelength at $\lambda = 510$ nm. Also in this case, the traditional fixed wavelength filtering could be replaced by a tunable MEMS FPI-based filter spectrometer for multiple wavelength measurement allowing several dyes to be measured, or by imaging the whole cell culture area with a MEMS FPI-based imaging spectrometer.

Droplet assays for cellular enzymatic reactions are often monitored with calorimetry, such as the MEMS nanocalorimetric sensor described in Chapter 4. However, Huebner et al. [52] describe a PDMS-based droplet trapping array for fluorescence monitoring of single *E. coli* cells and enzymatic reactions. Yellow fluorescent protein (YFP) was used for the compensation of droplet shrinkage in the measurement data, while the cells and the galactosidase were also monitored with fluorescence detection. Their results show how some of the repeatability problems described with calorimetric enzyme assays (shrinkage and poor reproducibility) could be overcome by introducing additional monitoring methods (fluorescence).

Finally, an excellent example of integrating several parallel sensing techniques for continuous on-line monitoring of yeast cells in a microfluidic cell culture platform comes from Krommenhoek et al. [53]. They built an integrated measurement system with ultra-microelectrode arrays (UMEA) for amperometric (electrochemical) detection of dissolved oxygen, an ion-selective field effect transistor (ISFET) for monitoring pH, impedance spectroscopy for on-line measurement of biomass and a platinum thermistor for temperature monitoring.

2.2 Impedance spectroscopy

Electrical impedance spectroscopy (EIS) involves passing a small AC current through a biological sample and determining its impedance response at various frequencies. It is a non-invasive tool that can be applied to studying the properties of cells, tissues and their culture environment [54]. EIS has been used to monitor cellular behaviour [55], to study cell attachment and spreading of mammalian cells [56], to monitor yeast cell division [57], growth [58] and cell cycle [59], and to assess cytotoxicity [60]. It is also a useful tool for differentiating cells in on-chip flow cytometry [61] or for characterizing ion channels at the single-cell level instead of using a patch-clamp system [62].

The commonly used electric cell-substrate impedance sensor (ECIS) consists of two parallel electrodes, a small detecting electrode and a larger counter electrode, where the impedance of the smaller electrode dominates the overall impedance. However, planar microelectrodes made with microfabrication technology in various configurations have gained interest in recent years, as this configuration allows impedance monitoring throughout the confluent cell layer or from different parts of the cell culture. In this setting, the field distribution of the impedance is more complex than in the parallel plate setting and the geometry of the microelectrodes affects the impedance response [63].

Impedance is the ratio of the voltage applied across the measured object to the current flowing through the object. Unless the system is purely resistive, the impedance is complex, consisting of a real part and an imaginary part, as described by:

$$Z = Z' + iZ'' = R - \frac{i}{\omega C} = |Z| e^{i\phi} \tag{1}$$

where

$$|Z| = \sqrt{(Z')^2 + (Z'')^2} \tag{2}$$

Z’ and Z’’ represent the real and the imaginary parts of the system, and the phase ϕ can be written as

$$\phi = \arctan\left(\frac{Z''}{Z'}\right) \tag{3}$$

Figure 2 illustrates the composition of impedance regarding its real and imaginary part and the phase. However, the drawback of this plot is that it is limited to a given frequency and, thus, when measuring the magnitude of impedance over a frequency range the Bode plot, which expresses the magnitude of the frequency response, is more suitable for this form of presentation (Figure 3).

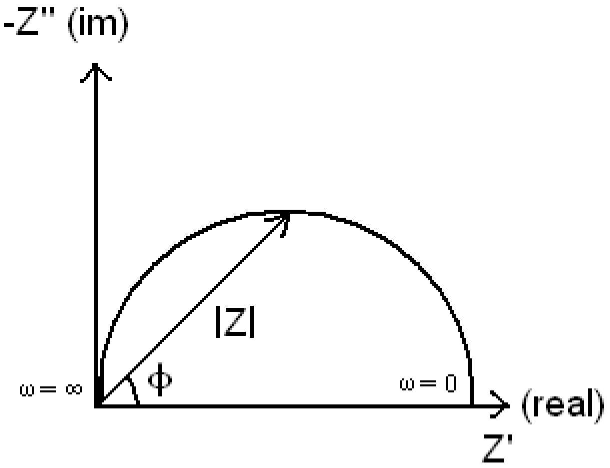

Figure 2. The Nyquist plot.

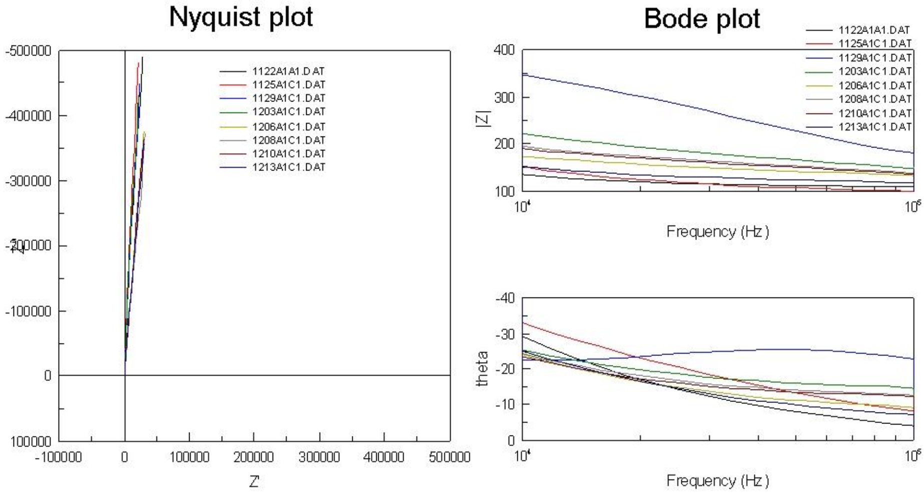

Figure 3. Differences in presentation between the Nyquist and Bode plot.

The properties of a system in which the cells form a monolayer on top of the electrode can be presented as a simple equivalent circuit presented in Figure 4, where R_m is the resistance caused by the culture medium, R_c and C_c are the resistive and the capacitive part of the cell layer, respectively, and C_{me} is the capacitance between the medium/electrode interface. This type of circuit was found by Wegener et al. [54] to be useful for quantitative interpretation of the impedance spectra of endothelial cell monolayers.

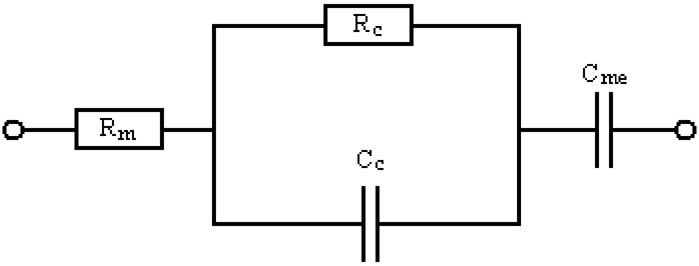

Figure 4. Equivalent circuit used in quantitative interpretation of endothelial cell EIS measurement by Wegener et al.

Another common representation of the impedances within a system with the electrode-electrolyte interface is the Randles circuit shown in Figure 5, which takes into account that in parallel with the double layer capacitance C_{dl} there is also charge transfer resistance R_{ct}, which is the result of current leakage across the double layer due to interfacial electrochemical (redox) reactions, as well as Warburg impedance Z_w, which results from the diffusion of ions to the interface and can be presented as series-connected with the charge transfer resistance.

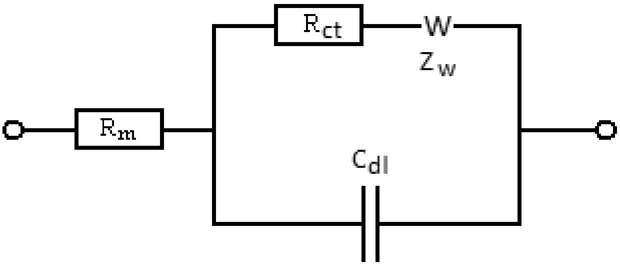

Figure 5. Randles circuit.

The use of these equivalent circuits enables extraction of the exact quantitative electrical properties of the measured cells from the impedance analysis, if needed. However, in many cases the qualitative measurement capabilities of the EIS technique are more suitable for monitoring purposes, such as in the case of monitoring the endothelial cell capillary formation in this work. In addition, in microfluidic cell sorters and culture cycle monitoring applications the usefulness of EIS comes from the detected change, not the absolute quantitative value.

No studies have been published to date on the use of EIS for monitoring endothelial cell capillary formation. Studies concerning the general short-term monitoring of endothelial cell cultures do, however, exist. A recent work performed with microfabricated planar electrodes by Rahman et al. examined cell-cell interactions and the motility of human umbilical vein endothelial cells. Their device consists of

16 planar microfabricated electrodes in a radial configuration [64]. They focussed on extracting electrical parameters for HUVEC and the used culture medium using the equivalent circuit approach. Their device was intended for short-term culture measurement rather than long-term cell growth and cycle monitoring, which is needed to assess cell cycle specific relative measurement data. Chung et al. investigated endothelial cell capillary formation in a 3D culture [65], but used only conventional microscope imaging and fluorescence to observe the structures.

Asami et al. [57] performed monitoring of yeast cell division with EIS, utilizing the relative change in impedance spectrum to determine cell properties specific to the cycle phase. Their device was, however, intended for macroscopic culture monitoring (500 ml volume) and also for a relatively short duration (< 16 h).

The specific challenges addressed in this dissertation regarding an EIS method for cell monitoring come from fabricating a microdevice capable of long-term monitoring of endothelial cell cultures (several weeks) in order to allow the culture to proceed to capillary formation and to use the relative change in the impedance spectrum to observe the changing culture properties.

2.3 Microcalorimetry

Essentially, all chemical and physical reactions are accompanied by the release or absorption of heat. This makes calorimetry a suitable characterization method for a very broad range of applications. As a characterization method for biological samples, it has the advantage of being non-invasive and not requiring tagging or surface binding. In recent years, microfabrication technology has enabled the development of small MEMS-based calorimetric sensors, which are less expensive and more cost-effective in terms of sample volumes than traditional bench-top calorimetric equipment. However, the measurement of liquid samples with MEMS sensors remains a challenge, as most of these sensors have been developed for gas or solid sample measurements.

The most common types of calorimeters are adiabatic, heat conduction, and power compensation calorimeters. A power compensation calorimeter uses a heater to compensate for the heat loss in an endothermic reaction. In an exothermic reaction, the process is balanced by a cooling power, typically using the Peltier effect. Measurements in this type of calorimeter are thus conducted under isothermal conditions. In an ideal adiabatic calorimeter, there is no heat exchange between the calorimeter and the environment. However, as this is practically impossible, most calorimeters used in this manner are semi-adiabatic, and the heat exchange is compensated.

In ideal adiabatic conditions, the quantity of heat can be expressed as

$$q = C_h \Delta T \,, \tag{4}$$

where C_h is the heat capacity of the system and ΔT is the temperature change of the process. As there is usually transfer of heat involved with the vessel and the surroundings, the calibration constant of the system can be experimentally determined and the heat energy expressed as

$$q = \varepsilon_c \Delta T \,, \tag{5}$$

where ε_c is the calibration constant. A change in the heat capacity of the measurement system will thus lead to a change in the calibration constant. The thermal power can be expressed using the calibration constant and the temperature change as

$$P = \varepsilon_c \frac{dT}{dt} \tag{6}$$

In heat conduction calorimeters, heat is allowed to transfer between the reaction vessel and the surrounding body, which serves as a heat sink, maintained at constant temperature. Usually this heat is conducted through a thermopile. In an exothermic reaction, the heat will flow from the vessel to the sink and in an endothermic reaction, from the sink to the vessel. The Tian equation presents the thermal power detected by the thermopile as

$$P = \frac{1}{K}\left[V_o + \tau\left(\frac{dV_o}{dt}\right)\right], \tag{7}$$

where V_o is the measured voltage difference across the thermopile, *K* is the sensor responsivity (V/W), and τ is the time constant. Under steady-state conditions using constant electric power during calibration this reduces to

$$P = \frac{V_o}{K} \,. \tag{8}$$

The time constant is ideally equal to the quotient between the heat capacity C_h of the system (including the reaction vessel and its contents) and the heat conductance of the thermopile *G*:

$$\tau = \frac{C_h}{G} \tag{9}$$

The calibration constant ε_c is ideally equal to the ratio between the thermal conductance of the thermopile and the Seebeck coefficient of the thermocouple material. Thus, it is not changed by heat capacity changes, reducing the need to calibrate the sensor before each experiment. The sensor responsivity can be expressed by

$$K = \varepsilon_c S \,, \tag{10}$$

where ε_c is the calibration constant and S is the Seebeck coefficient or the thermoelectric power of the thermocouple (V/K). The voltage output of a thermocouple is proportional to the temperature difference between the junctions

$$\Delta V = S\Delta T \quad . \tag{11}$$

Calorimeters for liquid sample measurements can be categorised as either open or closed chamber systems. Measurements in an open environment suffer from evaporation as well as inconsistencies in liquid sample handling. Closed chamber set-ups, on the other hand, suffer from heat conduction to the sensing body.

Besides the measurement principle and being an open/closed chamber set-up, calorimeters can also be classified according to their operating mode. Differential scanning calorimetry (DSC) involves the monitoring of two identical thermal detectors consisting of a sample or reaction under investigation and a reference sample or material for comparison, measured at a specific scanning rate. MEMS technology offers the advantage of fabricating identical small-sized sensors, which reduces the cost of analysis equipment. The miniature size offers the advantage that the energy required to heat the calorimeter itself (the addenda) is small compared to traditional differential scanning calorimeters (DSC) [66], so very small volumes can be measured.

Numerous MEMS calorimeters have been developed in the past for measurement in the solid or gas phase, but in recent years there has been growing effort to develop devices for liquid measurement. Lee et al. developed a measurement system composed of microfluidics, thermopiles and vacuum encapsulation [67] which was capable of characterizing 3.5 nl samples with 4.2 nW resolution, used for reaction heat measurements of urea hydrolysis. Wang et al. [68] presented a MEMS differential sensor based on reference chambers on polymer diaphragms connected with the thermopile with a sensitivity of about 3.1 µV/mM, tested on glucose solutions. Recht et al. demonstrate an enthalpy array based on thermistors made of vanadium oxide on polyethylene naphthalate membranes, based on differential measurement of reacting enzymes and a non-reacting sample liquid [70].

All of these liquid measuring closed-chamber calorimetric devices have been designed for the characterization of enzymatic reactions where the microfluidic channels offer an accurate way of transporting and measuring small volume samples. However, when dealing with biological cells, microfluidic channels used for sample transportation may be inconvenient due to particle clogging and difficulty of cleaning. This thesis work is based on a differential thermopile-based measurement of yeast cell samples in an open chamber setting where the droplets are pipetted onto the membrane of the calorimetric MEMS device. This may provide a fast means of analyzing yeast cell heat production, although the open environment may also present challenges.

2.4 Spectroscopy

Spectroscopy involves the measurement of the intensity of light (absorbed, emitted, reflected) at a given wavelength or interval of wavelengths. It is a commonly applied technique for measuring the concentration or amount of a given species. It is typically used in physical and analytical chemistry for the identification of substances through their emitted or absorbed spectrum. Spectrometers can be classified by their working wavelengths, including UV (ultraviolet), Vis (visible light), NIR (near infra-red) and IR (infra-red), the measurement technique used (single beam or double beam) and the spectrum acquisition method (monochromators, photosensors). For spectroscopic measurements, the sample is illuminated or excited utilizing a laser, high power diode, Xenon or infra-red (IR) light source and then the emitted or absorbed wavelength is measured with a device consisting of an optical filter (or several filters, for the measurement of the whole visible spectra, for example) and a detector.

Spectroscopy is a versatile tool that has been used in the UV-visible spectral range, for example, in quantifying protein and DNA concentration [69], reporter gene assays, LIF detection of biological warfare agents [71], enzyme activity assays and to monitor microbial growth [72]. In cell research it is a basic tool for characterizing cellular properties in tissues or at the single-cell level [73] by measuring the emission from fluorescent tags. The near- to middle wavelengths of the IR range (NIR – MIR) are typically used in absorbance spectroscopy, such as in gas concentration measurements [74, 75, 76], however they can also be used for glucose, glutamate, fructose, glutamine, proline, ammonia and CO_2 measurements in bioprocess media [77].

Until recently, spectroscopic equipment in the UV-visible spectral range has been very expensive and restricted to laboratory use; the size of the equipment is large and manual optical filter wheels are slow for measurement purposes [78]. MEMS technology has enabled the fabrication of small optical filters and detectors that can dramatically reduce the size and price of spectroscopic equipment [79]. By combining the current miniaturization efforts of sample preparation and handling in lab-on-chip devices with the detection and analysis capability of novel optical sensors, the whole chain from sample preparation to analysis can be covered; there is a true opportunity to bring real-time identification of diseases and pathogens from laboratories to the desks of health practitioners, into environmental and industrial monitoring, as well as consumer use.

2.4.1 Absorption spectroscopy

In absorption spectroscopy, light is directed through the sample and the absorbed, transmitted or reflected light is detected. Molecules can absorb light by promoting electrons to a higher level, while the photon energy has to match the energy required to promote the electron. Visible absorption spectroscopy is often combined with UV absorption spectroscopy. UV region photons have enough energy to be absorbed by all kinds of atoms.

The general law used to describe absorbance spectroscopy is Lambert-Beer's Law:

$$A = ebc, \tag{12}$$

where: A is absorbance, e is the molar absorptivity, b is the path length of the sample and c is the concentration of the compound in solution.

The derivatization of spectral data offers further enhancement in resolution of overlapping peaks and elimination or reduction of background or matrix absorption [80]. Derivative UV/Vis spectroscopy can be conducted using wavelength modulation, dual-wavelength measurement or mathematical methods.

UV absorbance spectroscopy allows quantitative analysis of all molecules that absorb light. The traditional UV/Vis/NIR spectroscopy applications areas include materials characterization, optics, coatings, glass, and pharmaceutical quality assurance and quality control (QA/QC). In traditional UV-spectroscopy, samples were mostly in liquid form. However, flexible fibre-optic dip probes have brought more versatility to the measurements. Fibre-optic reflectance probes enable sampling of solid surfaces and powders as well as liquids.

2.4.2 Fluorescence spectroscopy

Fluorescence spectroscopy is a basic tool for analyzing biomolecules, cells and compounds. Certain molecules have the ability to absorb light of a higher frequency and then emit light at a specific lower frequency. A light source, such as a laser, led or filtered lamp is used to excite the sample molecules to a higher energy state. As the molecules then drop to a lower vibrational level of the ground state, they emit photons at a certain wavelength and at a certain intensity. These fluorescent dyes are used in cellular biology to mark different components (antibodies, proteins etc.). These dyes are then used as probes in microscopy or spectroscopy.

Fluorescence spectroscopy can be used to assess many different properties of cells, such as metabolic and enzymatic properties, nutritional state and elemental content of individual cells and measurement of intracellular pH [81]. Fluorescence spectroscopy usually involves the use of commercially available fluorescent dyes and stains, with different emission wavelengths and staining methods. Multiple fluorescent stains can be used simultaneously. For example a commonly used fluorescent dye called fluorescein absorbs blue light (430–500 nm) and then emits green light (520–565 nm). Another commonly used fluorescent probe is green fluorescent protein (GFP), which was originally isolated from a jellyfish *Aequorea victoria*, and which can be further genetically engineered into mutants with specific properties. These fluorescent proteins can be used to mark and track specific cellular organelles. Fluorescent detection can also be done without any labelling by laser induced fluorescence (LIF).

2.4.2.1 Fluorescent stains and green fluorescent protein (GFP)

Different stains are commercially available for different intracellular macromolecules. These include, for example, specific stains for lipids, nucleic acids and proteins. Key practical properties of the stains include their excitation and emission spectra and high extinction coefficient (high absorption wavelength) in the excitation frequency, which enables detection of small amounts of stain and detection of whether the measured sample contains autofluorescent molecules of a similar excitation wavelength as the stain [82].

The GFP mutants have several advantages over traditional fluorescent stains; they can be genetically engineered to respond to a variety of biological signals, targeted to specific subcellular compartments, introduced into cells and tissues while keeping them intact, and they are rarely toxic. New GFP variants with altered excitation and emission wavelengths, enhanced brightness and improved pH resistance relative to the original green, cyan and yellow variants [83] are being developed.

2.4.2.2 Multi-wavelength fluorometry

Multi-wavelength fluorometry involves measuring fluorescence from more than one excitation and emission wavelength. This is a useful non-invasive method to monitor various bioprocesses. Skibsted et al. showed that by applying a PLS (partial least square) analysis to multi-wavelength fluorescence measurements it is possible to perform quantitative predictions of various key parameters in bioprocess [84], such as exhaust gas O_2 and CO_2 composition as well as succinate, protein and nitrate concentration and the optical density of medium in *Pseudomonas fluorescens* culture. Surribas et al. [85] used a similar technique of combined multiwavelength fluorescence measurement and mathematical modelling to monitor biomass and substrates (glycerol and methanol) during cultivations of *Pischia pastoris* for the production of *Rhizopus oryzae* lipase (ROL). Haack et al. [86] monitored the cell mass of *Saccharomyces cerevisiae* cultivation on-line using multi-wavelength fluorescence.

Biological process monitoring is an important aspect of production optimization in various pharmaceutical and chemical processes aimed at obtaining products such as biofuels, pharmaceutical ingredients and enzymes.

2.4.3 Microspectrometers

Today, micro-opto-electro-mechanical sensors (MOEMS) are changing the field of spectroscopic measurement. Traditional spectroscopic instruments are high performance, large and expensive devices designed mainly for laboratory use. In recent years, MEMS technology has enabled the replacement of expensive optic filters in spectroscopic instruments operating in the IR spectrum with tunable microfabricated filters based on very small mirror structures. Currently, these small, robust, fast-measuring, sensitive and specific devices can be used to measure, for example, concentrations of pollutants and greenhouse gases outside the laboratory.

Most commercially available MEMS-based microspectrometers can be used to perform measurements in the IR spectrum range. Infrared absorption spectroscopy is used for the identification of functional groups of organic and organometallic molecules. Electrically tunable Fabry-Perot interferometers combined with thermopile detectors can be applied to measure CO_2 concentration, based on NDIR (non-dispersive infra-red) Single-Beam Dual-Wavelength measurement [87]. The operating wavelength of these sensors is above 1 μm.

Even though various MEMS-based devices are already available for the IR spectrum measurements, spectrometers for the UV-visible range of the spectra are less common. This spectral range is especially interesting in biological applications, as the wavelengths of most of the dyes used in fluorescence measurements are located in the visible part of the spectrum (Figure 6).

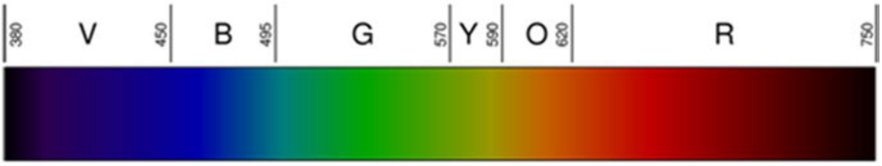

Figure 6. The visible spectrum.

Microspectrometers can be classified into three groups based on their operating principle: grating-based, Fourier transform and interferometer spectrometers. Interferometers are usually based on the Michelson, Mach-Zehnder or Fabry-Perot principles.

Grating-based microspectrometers utilize the interference of incident light at the grating for dispersion. Grating-based microsensors have been fabricated for both the visible and near-infrared part of the spectrum [88]. Michelson and Mach-Zehnder interferometers are very suitable for glass fibre or waveguides, whereas the Fabry-Perot interferometer is most often used for MEMS-based microspectrometers. This is mostly due to the nature of MEMS fabrication technology, which allows monolithic assembly, various combinations of thin films and movable/dimensional features, thus supporting the creation of Fabry-Perot structures. The Fourier microspectrometer is basically a modification of the Fabry-Perot interferometer, in the sense that instead of being covered by a mirror, the detector is at a fixed position within the incident light path and measures the intensity at a well-defined distance from a movable mirror [88]. FT-IR is used, for example, in the analysis of solids (organic, inorganic, and biological) in a variety of forms including fibers, thin films, particles, powders, coatings, residues, monolayers, and monolithic solids.

Several interesting MEMS FPIs developed for IR spectrum measurements can be found in the literature. Parashar et al. have designed and modelled a three-cavity tunable MEMS FPI for measurements between 2.4 μm and 4,018 μm based on deflecting Ag mirrors, without realizing the device yet. Tunable Fabry-Perot filters with SiO/Ge Bragg mirrors integrated monolithically on HgCdTe-based photodetectors have been reported [89, 90], but the tuning range was limited to 1/3 of the gap and the mirrors suffered from non-ideal film quality due to an uneven starting surface from the detector and due to bending.

Until recently, Fabry-Perot interferometers for the visible spectral range have been less common compared to MEMS FPIs capable of measuring in the IR range. Some examples found in the literature consist of silver (Ag) mirrors supported by a SiN membrane and a Si frame, but the transmission was limited to 10% due to silver absorbance and the FWHM of the optical resonance was about 20 nm [91]. The difficulty in designing a MEMS-based FPI for the visible spectrum arises from the requirement for very thin film thicknesses ($\lambda/4$) and the required high quality of the layers in the Bragg mirror stacks (conformal coating, good uniformity with minimal thickness variation over the entire wafer, no pinholes). The development of the atomic layer deposition (ALD) technique enables precise film thickness control of high quality dielectric films, while making it possible to also develop new low-temperature MEMS processing methods utilizing new materials of sacrificial layers, such as polymers and polyimides [92]. Based on this, the first tunable MEMS FPI-based on ALD dielectric layers for the visible wavelength range was developed [93].

Also in the present work, a process was developed for monolithic integration of the FPI structure directly on a photodiode with the aim of realizing a first-in-the-world microspectrometer-on-chip for visible spectral range measurements, as well as developing alternate techniques for separate tunable FPI filters. Combining these MEMS-based optical filters with detectors, new miniature spectrometers for single-point as well as imaging spectrometers can be realized, which may be applied to the characterization of biological cells.

3. Impedance spectrometry of endothelial cells

3.1 Introduction

In this study, capillary endothelial cells were cultured in polydimethylsiloxane PDMS/glass microdevices to investigate their capillary formation by using impedance spectrometry [1]. The cells used in this study were Bovine Adrenal Cortex Capillary Endothelial Cells (BACC-ECs), which have a high capability to form capillary-like structures when maintained at confluence. The objective was to monitor the culture growth by electrical impedance spectroscopy (EIS) measurements to observe whether the capillary tube formation produces a change in the impedance spectrum. As the capillary formation takes several weeks of culturing during which the cells require minimal disturbance, EIS is a very suitable tool due to its non-invasive measurement characteristics and sensitivity for surface phenomena within the cell culture area, while allowing stable monitoring over long periods of time.

3.2 Theory

3.2.1 Endothelial cell signalling and tube formation

Endothelial cells (ECs) play an important role in angiogenesis. This formation of new blood vessels occurs during tumour growth, embryonic development, wound healing and metastasis [94]. Better understanding of endothelial signalling during development could lead to new targeted therapies for heart disease, diabetes and cancer [95]. There are several sequences in angiogenesis, including local degradation of the endothelial basement membrane by the action of proteases, migration of endothelial cells (and formation of sprouts), proliferation of endothelial cells and lumen formation [96] (Rahmanian et al.).

Different types of tissues have different kinds of endothelial cells. ECs have many common features, but they also exhibit diversity such as vessel-size specific, organ-specific and age-specific characteristics [95]. ECs in different organs are required to perform functions specific to each organ. In addition, the capillaries formed by ECs in skeletal muscle, heart, lung, and brain are continuous, whereas capillaries in endocrine and exocrine glands, choroids plexus and intestinal villi have fenestrations [97]. Endothelial cell capillary tube formation is a multi-step process involving cell adhesion, migration, differentiation and growth. Endothelial cell growth, differentiation and apoptosis can be affected by modulating their size using micro-patterned adhesive islands [98]. As reference, images of endothelial cell capillaries obtained by Glienke et al. are shown in Figure 7, and Figure 8 shows capillaries observed in this study.

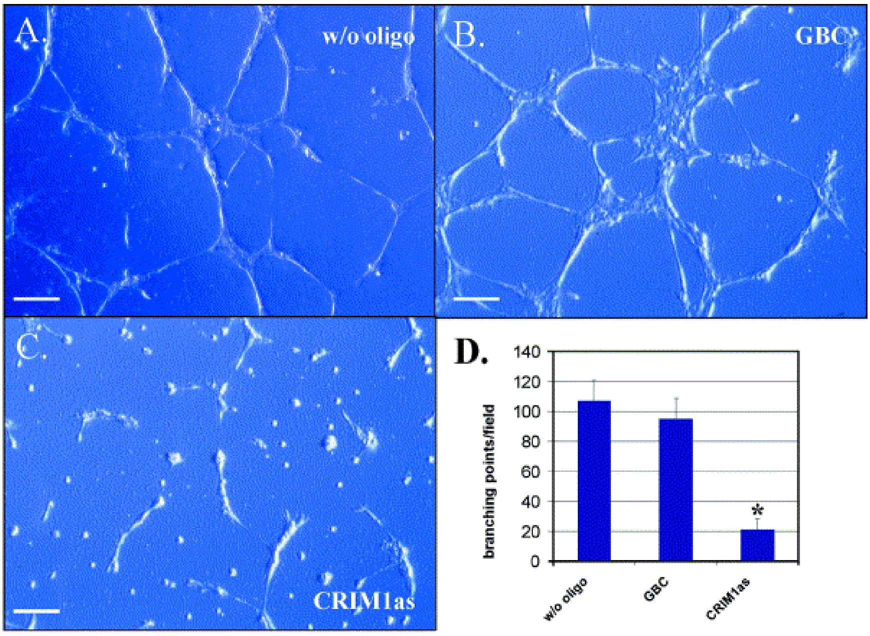

Figure 7. Je68/CRIM1 mRNA downregulation inhibits tube formation of HUVEC on Matrigel. A) Untransfected cells B) Control transfected cells C) Transfected cell D) Number of branching points per visual field. Bar 125 µm. Reprinted with permission from the publisher [99].

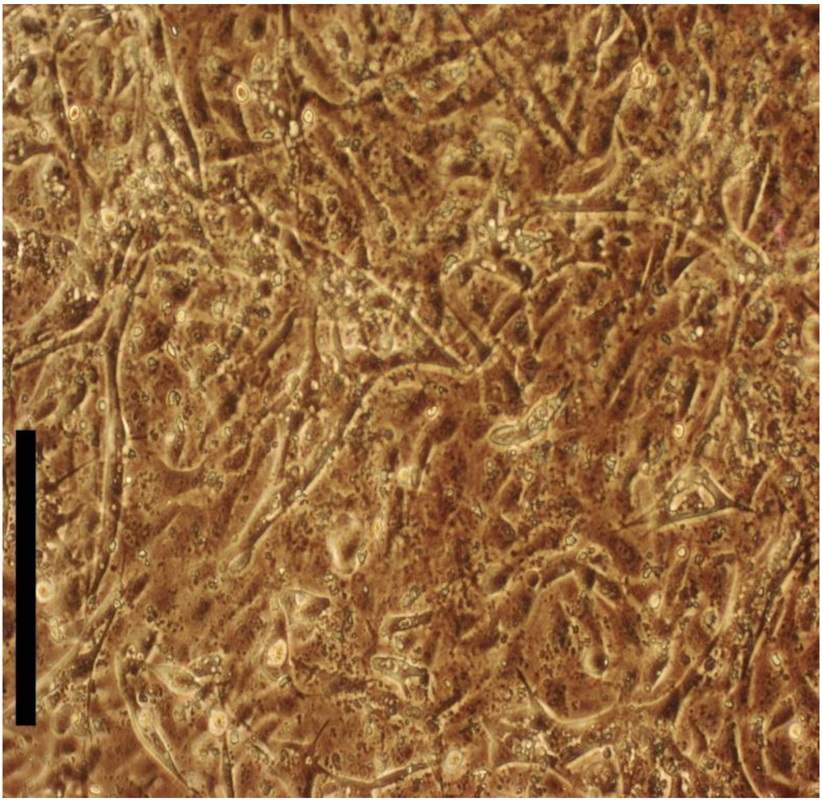

Figure 8. Endothelial cell capillary structures after 3 weeks of culture, bar size 250 µm.

3.2.2 Capillary tube formation growth factors

It is known that tissues signal to endothelial cells. There are several proteins that affect angiogenesis, such as fibroblast growth factors (FBF-1 and FBF-2), vascular endothelial growth factors (VEGF), proteoglycans and glycosaminoglycans. Angiopoietins (such as Ang-1 and Ang-2) are required for maturing of the vasculature. Angiostatin inhibits endothelial cell migration and tube formation [100]. ECs also appear to give signals to their surrounding tissues [95].

VEGF induces vascular formation and angiogenesis as it is required to initiate the formation of immature vessels by vasculogenesis or angiogenic sprouting during embryonic development and in adults. Endocrine gland-derived vascular endothelial growth factor (EG-VEGF) promotes proliferation specifically in cells derived from endocrine glands [101].

Erythropoietin is also a known growth factor. Anagnoustou et al. [102] observed the dose-dependent proliferative action of human umbilical vein endothelial cells (HUVECs) and bovine adrenal capillary endothelial cells when using recombinant human Epo (rHuEPO). Jaquet et al. [103] observed that rHuEPO stimulated capillary outgrowth up to 220% compared with non-stimulated physical outgrowth, whereas VEGF165 increased outgrowth by 230%, concluding that erythropoietin exhibits equal angiogenic potential to VEGF.

3.2.3 Cell attachment

Some cell types do not attach to gold electrodes due to the hydrophobic nature of gold. The work of Mrksich et al. [104] suggested that endothelial cells can be attached to gold surfaces using self-assembled monolayers (SAMs, specifically alkanethiolates) and fibrinogen proteins. Mrksich et al. also noted that hydrophobic surfaces in general do not support the attachment of cells when using proteins.

To be able to investigate a confluent cell monolayer and capillary formation, it is desirable for the cells to attach themselves also to the glass surface between the electrodes. This can be achieved by making the glass surface hydrophilic using O_2 plasma treatment. Oxygen plasma essentially breaks the hydrogen bonds on a given surface, thus leaving it hydrophilic.

3.3 Experimental

3.3.1 Measurement device

The device consists of seven pairs of gold electrodes on a glass substrate of different dimensions. The device configuration, with numbered electrode pairs, is shown in Figure 9. The dimensions of the electrodes are presented in Table 1. The purpose of the design is to vary both the electrode surface dimensions and the distance between the electrodes to be able to experimentally observe the differences between the chosen geometries and sizes. Although the width of the thinnest electrodes is in the order of the capillary size (~ 300 µm), it is still the entire culture area which is of interest.

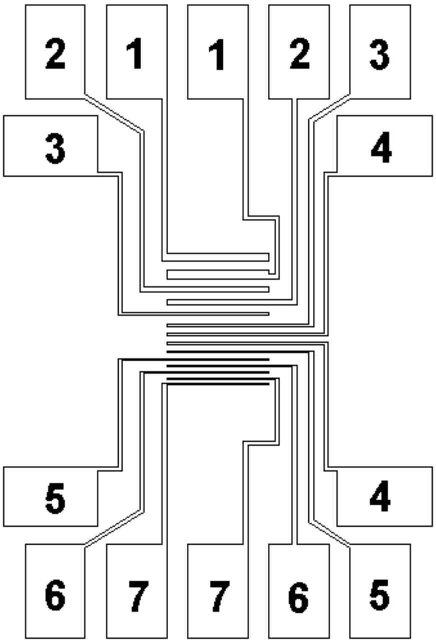

Figure 9. Gold electrode configuration and electrode numbers [1].

Table 1. Device dimensions [1].

El. Pair No.	Width/ mm	Area / mm^2	Distance / mm
EP1	1	1	1
EP2	0.5	0. 25	1
EP3	0.3	0.09	1
EP4	0.3	0.09	0.8
EP5	0.2	0.04	0.7
EP6	0.1	0.01	0.6
EP7	0.2	0.04	0.4

3.3.2 Device fabrication

The fabrication process of the device is shown in Figure 10. Glass substrates were cleaned by immersing them in Sica Clean solution (alcohol solution containing alkyl titanate for surface bond activation) in ultrasound for 30 min and then DI water for 30 min. A Au/Cr layer was deposited by evaporation in the same vacuum.

A thin chromium layer (20 nm) was used as an adhesive layer for the gold layer, which was approximately 200 nm thick.

The electrode lithography was done by spinning positive photoresist S1813 (3000 rpm for 30 s), prebaked on a hotplate at 110 °C for 1 min, exposed to UV radiation (E = 10 mW/cm^2) for 10 s, developed for 75 s, and post-baked at 110 °C for 5 min. The gold was etched in potassium iodide etchant for 95 s and the chromium was etched for 15 s in chromium etchant, prepared from 165 g diammonium cerium(IV) nitrite, 43 ml Perchloric acid and 1 l water.

The PDMS parts were fabricated by pouring 40 g of Silpot 184 and 4 g of Catalyst Silpot 184 into a container and mixing carefully. The solution was degassed by alternating vacuum pumping and air pressure in a chamber. The solution was then poured into two containers with a glass substrate on the bottom of each container. The glass substrates had been cleaned and coated with a thin Teflon layer in RIE with CHF_3 plasma for 12 min (P = 75 W, p = 20 Pa, CHF_3 flow = 50 sccm) to enable the hardened PDMS to be later peeled from the glass surface. The PDMS solution was degassed again for approximately an hour and then cured in an oven at 75 °C for 90 min.

The hardened PDMS was then peeled carefully from the glass surface, placed on a clean plastic surface with the clean surface (PDMS/glass) down, and the culture area walls were carved, taking advantage of the transparency of the PDMS and the plastic and using a paper sketch of the desired pattern.

The glass substrate with the gold electrodes and the PDMS part were then placed in RIE to treat the top part of the glass/Au substrate and the clean side of the PDMS part with oxygen plasma for 5 s (P = 75 W, p = 20 Pa, O_2 flow = 50 sccm). The O_2-treated surfaces were then pressed together to allow a waterproof seal to form between the glass/Au surface and the PDMS.

The samples were then coated with 5 mM 11-mercaptoundecanoic acid for 3 hours to obtain a self-assembled monolayer (SAM) to allow cell attachment on the gold electrodes. The short O_2 treatment (5 s) was sufficient enough to make the glass surface hydrophilic to support endothelial cell bonding. A photograph of the final measurement device is shown in Figure 11.

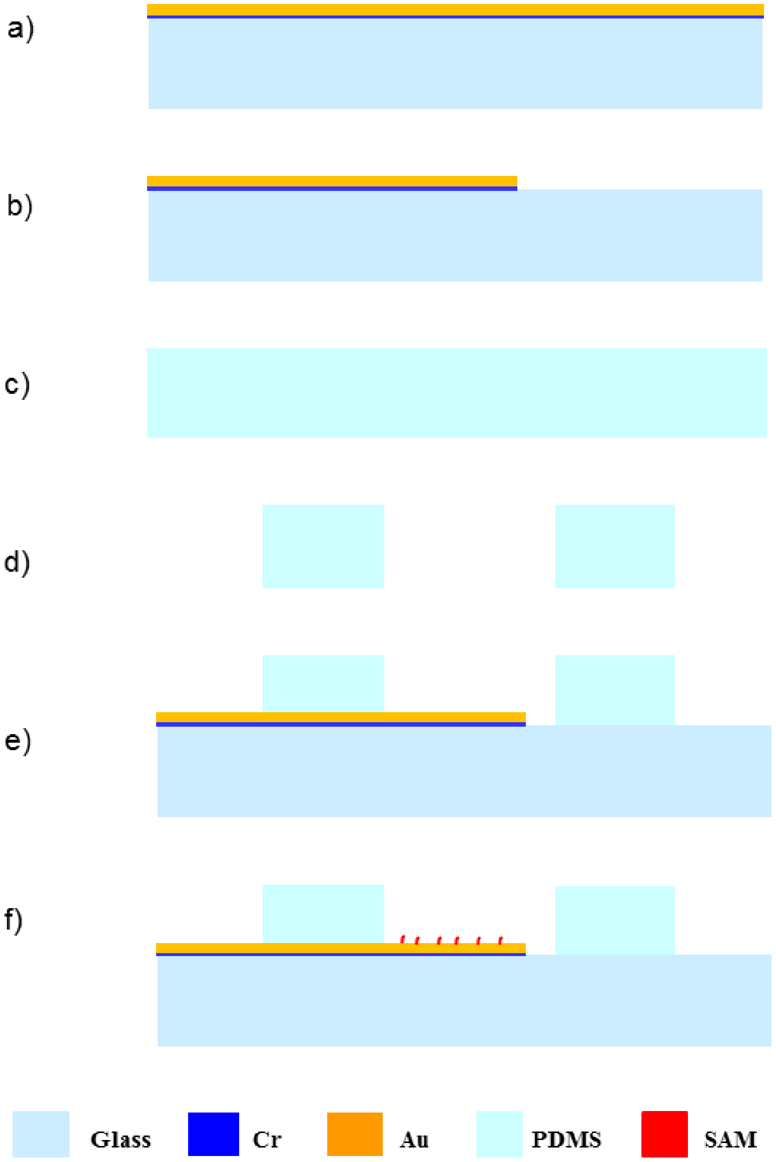

Figure 10. Fabrication of the device. a) Cr/Au films are sputtered, b) lithography and etching of Cr/Au layer, c) preparation of PDMS, d) structuring of PDMS, e) joining of PDMS part to the device substrate and f) SAM coating with 11-mercaptoundecanoic acid.

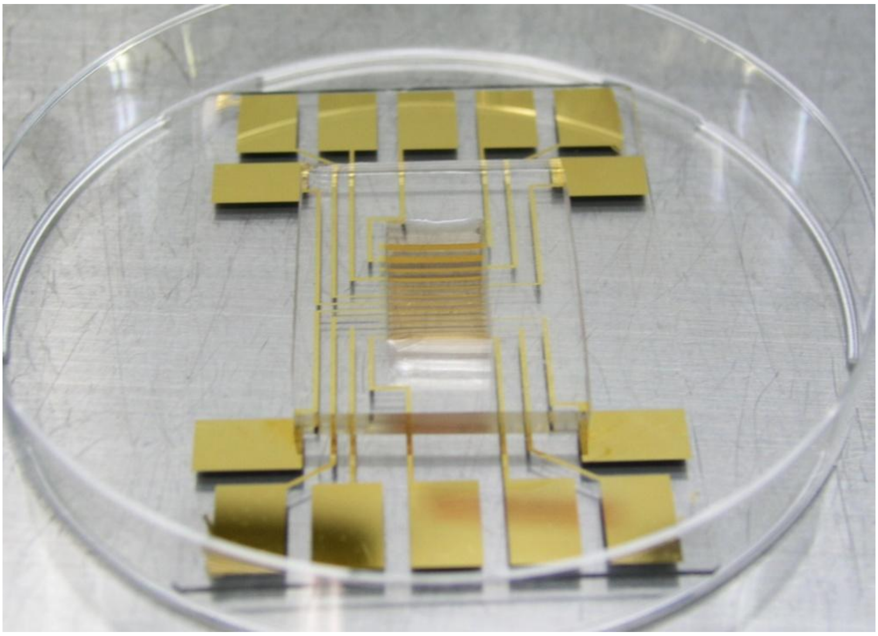

Figure 11. The device. The culture area defined by the PDMS can be seen in the middle.

3.3.3 Culture protocol

A ∅ 90 mm Petri dish was used to culture the cells in a total volume of 10 ml of culture medium with incubation in 5% CO_2 at 37 °C in a high humidity atmosphere. The culture medium was changed every 2 or 3 days. Harvesting and subcultivation of cells was performed every 4 to 6 days by first washing quickly with 10 ml PBS and using 2 ml of trypsin/EDTA for 4 min at 37 °C. To stop trypsinization, 8 ml of culture medium was added to the Petri dish. Subcultures were made by taking 1 ml of the solution with harvested cells and adding 9 ml of culture medium. The cells used for subcultivation were never allowed to grow to confluence as this can lower their growth ability. The approximate inoculation density was $1*10^4$ cells per cm^2. Cell counting was done using a standard hemocytometer.

Two different culture media were compared in terms of capillary growth. The first was low-glucose Dulbecco's Modified Eagle's Medium (DMEM), supplemented with 2% HEPES buffer (Sigma), 20 % Fetal Bovine Serum (FBS, JHR Biosciences) heat-inactivated at 56 °C for 30 min, with 1% NEAA and antibiotics. The other culture medium was alpha medium with similar supplementation.

Capillary formation was also investigated separately by allowing the cells grow to confluence in 3–4 ml of culture medium in a ∅ 35–60 mm Petri dish.

3.3.4 Measurements

A Solartron 1260 Impedance Analyzer and Solartron Dielectric Interface 1296, connected to a PC for data handling and analysis, were used for the measurement and analysis of the cell layer properties. The set-up is presented in Figure 12 (courtesy of V. Senez). The interval of the cell layer measurement ranged from one to several days. The measurements were made utilizing combinations of electrode pairs of various dimensions and at different areas of the culture surface. Additionally, measurements without cells were made to compare the characteristics of each individual device and their electrodes using culture media.

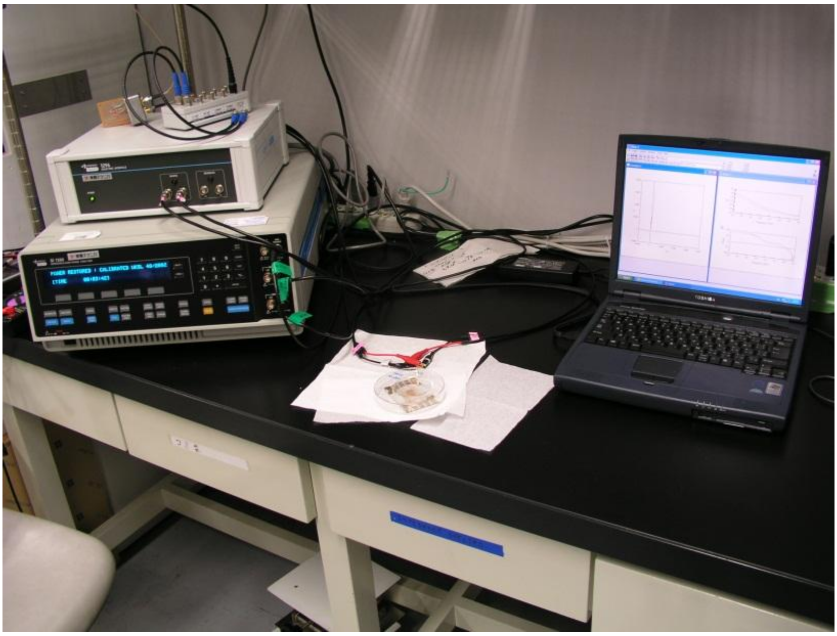

Figure 12. The impedance measurement setup.

The cultures in the microdevices were started with $1.4*10^5$ endothelial cells per device. The total culturing time ranged from one to several weeks. The amount of culture medium used in each measurement was 800 µl (37 °C), and was changed immediately before the measurement in order to avoid measurement variation due to different electrical properties of aged culture medium. Between measurements the devices were stored in the cell laboratory incubator in ∅ 100 mm Petri dishes and removed to another laboratory for impedance measurement. To prevent culture contamination during measurements, a ∅ 60 mm Petri dish bottom was placed on the device to act as a cover to protect the PDMS part and the culture (inside the 100 mm Petri dish).

To perform the frequency scan in the range from 10 Hz to 10 MHz takes about 6 minutes. Usually three, sometimes even five frequency scans with different electrode pairs were performed during each measurement. Human body temperature was taken advantage of to maintain the culture close to 37 °C during the measurement. The device was taken out of the 100 mm Petri dish, and held in hand using sterile gloves as shown in Figure 13 to maintain the culture temperature as close to 37 °C as possible, in order to avoid temperature changes which might disturb the culture and induce peeling off of the culture. Temperature has no effect on the impedance measurement itself.

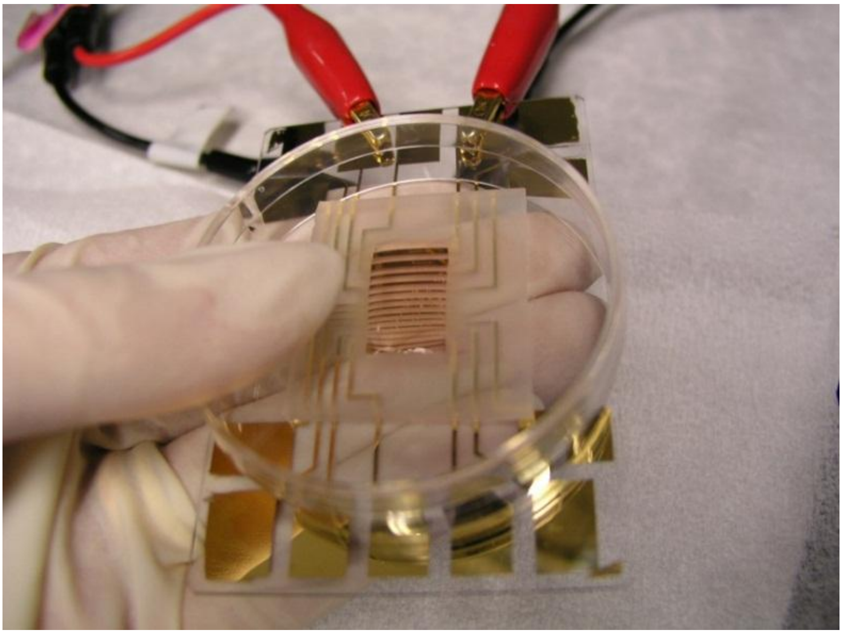

Figure 13. Measuring the cell culture.

After the measurement, the device was taken back to the cell laboratory in the 100 mm Petri dish. Before placing the dish into a clean bench, the dish upper lid was removed and the device was sprayed with 70% EtOH to sterilize it. The 60 mm cover was left in place to protect the culture area. Inside the clean bench, the 60 mm cover was removed and the device was placed in a new sterile 100 mm dish. The culture was washed once with 800 µl culture medium (37 °C). Pictures were taken of the cell layer from different parts of the culture (the electrodes pairs which were measured) to assess the correspondence to the measurements, and before placing the device in the incubator, the culture medium was changed once more to 1 ml (37 °C).

3.3.5 Cell adhesion tests with SAMs

Cell adhesion to the gold electrodes was done in cooperation with Kim Laboratory, IIS, Tokyo University by preparing glass samples with patterned gold coating. Tests were done using collagen and self-assembled monolayers (SAM) of alkanethiolates with an oxygen plasma treated surface and untreated surface. The SAMs used in these tests were 11-mercaptoundecanoic acid (11-MUA), (HS(CH2)10COOH, 11-MUA).

Cell attachment tests were continued by the author using prepared measurement devices for testing. Tests were done with different SAM solutions in combination with oxygen plasma treatment, including 5mM hexadecanethiol (HDT) in ethanol, 11-MUA, 5% dodecyltrichlorosilane (DTS) in toluene and 5% octadecyltrichlorosilane (OTS) in toluene.

Samples were treated as follows:

- A1 and A2: O2 plasma and 11-MUA coating (3h)
- A3: O2 plasma, DTS coating on glass (3h) and HDT coating on Au (3h)
- A4: O2 plasma, DTS coating on glass (3h) and 11-MUA coating on Au (3h)
- A5: O2 plasma, OTS coating on glass (3h) and HDT coating on Au (3h)
- A6: O2 plasma, OTS coating on glass (3h) and 11-MUA coating on Au (3h).

In addition, tests were done using glass samples with patterned gold coating, without O2 plasma treatment and without the presence of PDMS in the samples.

These samples were treated as follows:

- B1: HDT coating on Au (3h) and OTS coating on glass (2h)
- B2: 11-MUA coating on Au (3h) and OTS coating on glass (2h)
- B3: HDT coating on Au (3h) and DTS coating on glass (2h)
- B4: 11-MUA coating on Au (3h) and DTS coating on glass (2h).

3.4 Results

3.4.1 Cell adhesion tests with SAMs

Proper cell attachment over the entire culture surface was obtained using oxygen plasma treatment of the glass surface and 11-MUA coating of the gold electrodes. The use of collagen to cover the gold electrodes and oxygen plasma treated surface proved ineffective, as the cells would not attach themselves to the glass.

The cell attachment on samples A2–A6 is presented in Figure 14. On sample A2, the cells attached to both the glass and the gold. In samples A3–A6, there was no attachment on glass. In samples A4 and A6, the cells attached on the gold for a brief period, but ultimately peeled off. In samples A3 and A5, the cells did not attach to the gold.

In samples B1–B4, the cells did not attach to the glass. However, some attachment to gold was observed with samples B3 and B4, as seen in Figure 15.

This attachment behaviour implies that a hydrophilic glass surface obtained with oxygen plasma treatment combined with a 11-MUA self-assembled monolayer results in best cell attachment and culture surface properties.

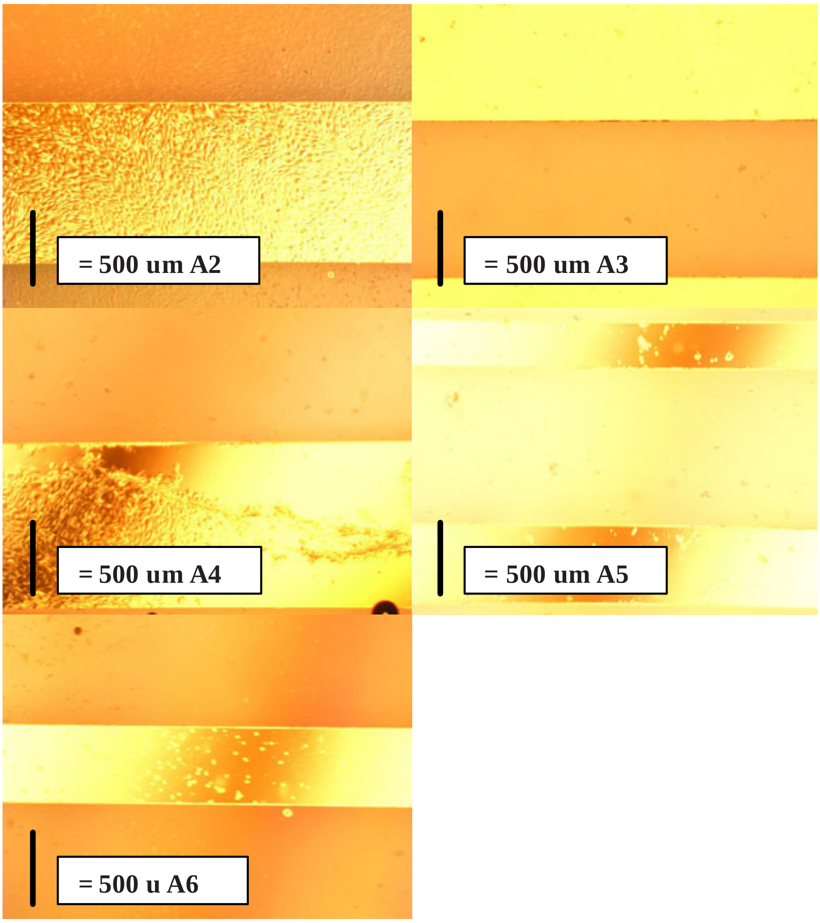

Figure 14. Cell attachment on samples A2–A6. A2: attachment on both glass (seen as orange) and gold (seen as bright yellow), surface modified with O_2 plasma treatment and 11-MUA coating. A3: no attachment on gold (HDT) /glass (DTS) surfaces. A4: initial attachment on gold (11-MUA), subsequent peeling. No attachment on glass (DTS). A5: no attachment on gold (HDT)/glass (OTS) surfaces. A6: no attachment on gold (11-MUA)/glass(OTS). Unattached cells show as round particles in the images.

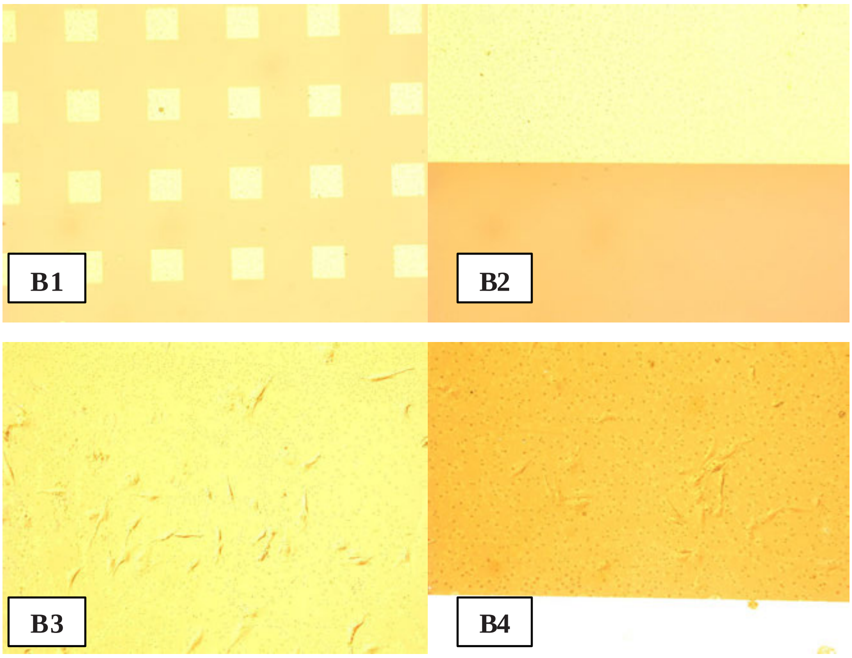

Figure 15. Cell attachment on samples B1–B4. B1: Gold (seen as yellow) with HDT and glass (seen as orange) with OTS, no attachment. B2: Gold with 11-MUA and glass with OTS, no attachment. B3: Gold with HDT and glass with DTS, attachment only on gold. B4: Gold with 11-MUA and glass with DTS, attachment only on gold.

3.4.2 Capillary growth using DMEM and alpha medium

When using DMEM as the culture medium, the capillary formation took approximately 4 weeks, resulted capillary structures shown in Figure 16. With alpha medium, the capillary structures were very distinct after three weeks (Figure 17). The length of these structures extended several hundreds of micrometers. The first branching was visible already after 2 weeks (Figure 18 and Figure 19). In terms of capillary growth, alpha medium proved to be much more efficient. In addition, upon visual inspection, the structure density obtained using DMEM appeared smaller compared to the capillary density obtained with alpha medium.

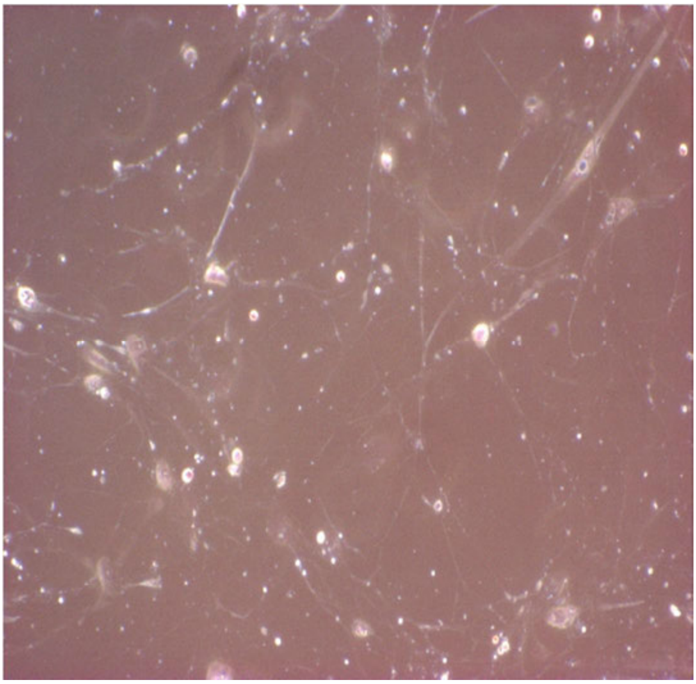

Figure 16. Capillary formation in the culture (Petri dish) after 4 weeks using DMEM.

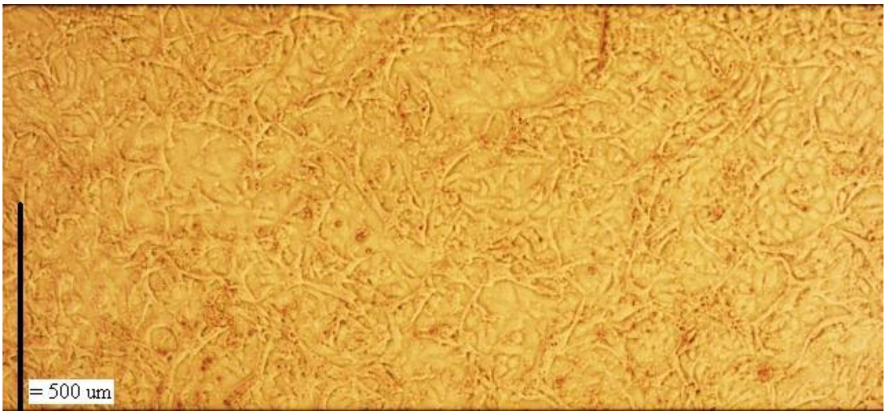

Figure 17. Device A2. Distinct capillary structures after three weeks of culture [1].

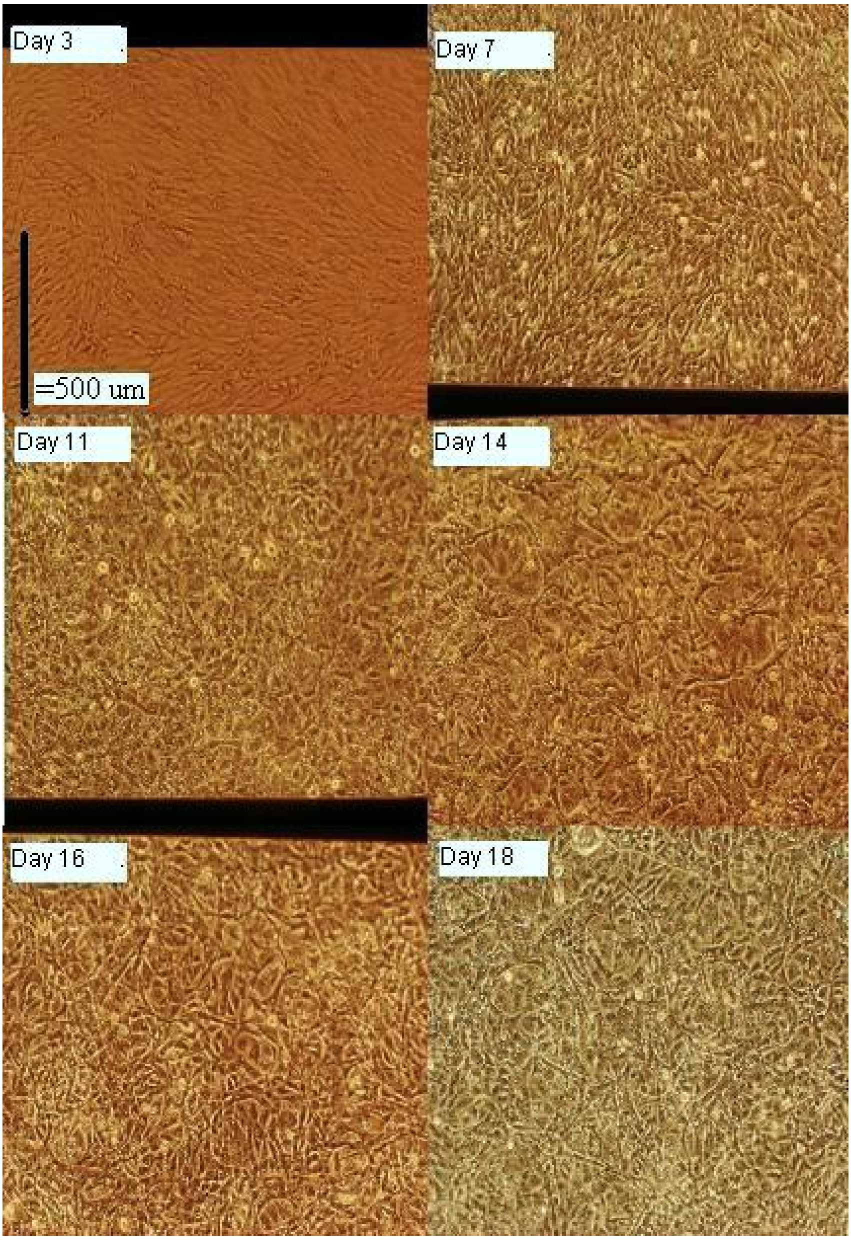

Figure 18. Capillary formation in device A2 observed with an optical microscope during days 3 to 18 (counting the start of the cell culture as day 1) [1]. Confluence is obtained by day 7, after which the cells start to elongate (day 11) and form capillary structures which increase in length between day 14 and day 18.

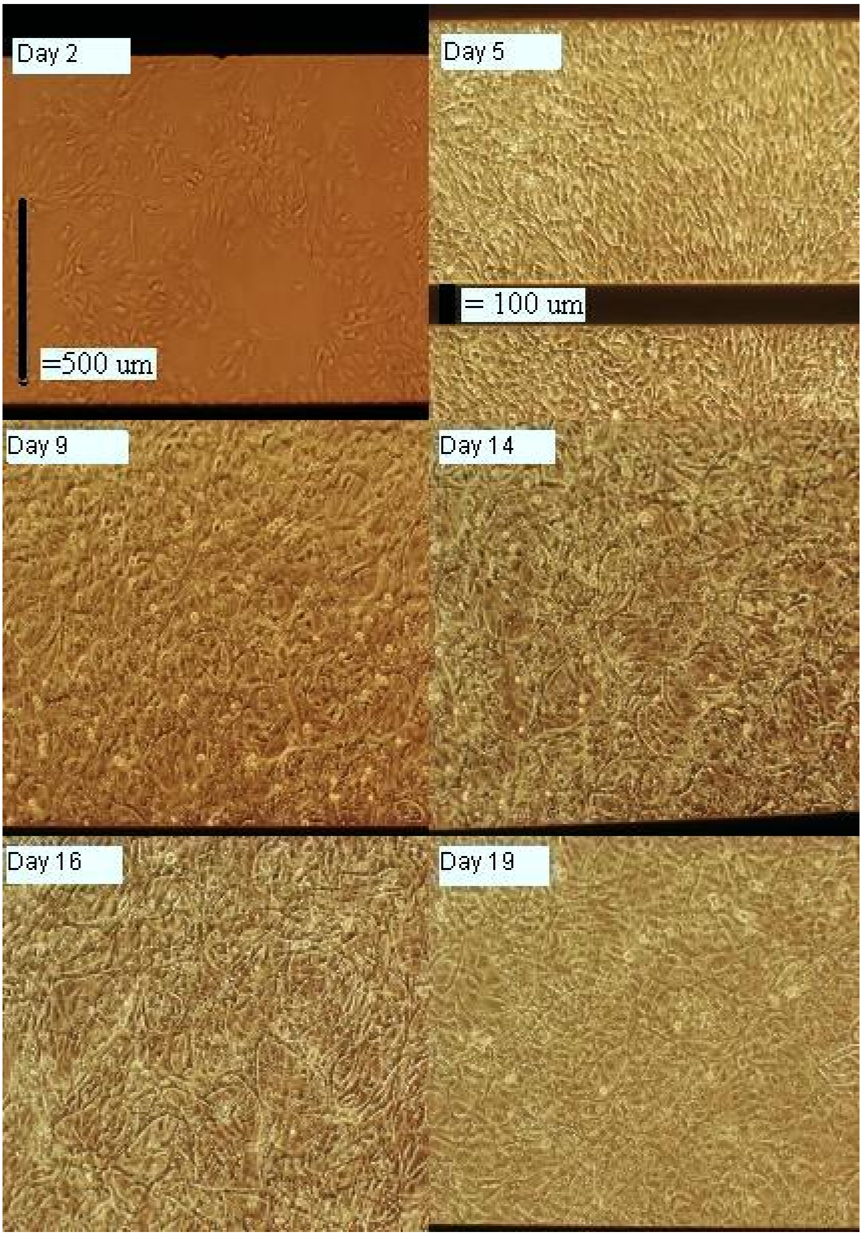

Figure 19. Capillary formation in device A1 observed between days 3 to 18 (counting the start of the cell culture as day 1). Confluence on day 5 is followed by the cells starting to elongate and form capillaries (day 9). The density of the capillary structures increases (days 14 to 16) until the capillary density ceases to increase (days 16 to 19).

3.4.3 Impedance measurements with culture medium

Measurements using culture medium were made to compare the characteristics of each individual device and electrode pairs of different dimensions. In Figure 20 (page 52) and Figure 21 (page 53), the lowest impedance values are obtained with the largest electrode pairs (EP 1) and the largest impedance values were obtained with the smallest electrode pairs (EP 6).

In Figure 22 (page 54), smallest and largest electrode pairs in different devices were compared, with the impedance curves matching each other. This allows comparison between different cultures.

In Figure 23 (page 55), the two culture media used (DMEM and alpha) were compared to see if their electrical behaviour is similar, and whether comparisons between cultures in different media can be made. Again, the impedance curves match.

The impedance curves shown in Figure 20 to Figure 23 represent those of a typical electrode-electrolyte system, consisting of solution resistance, charge transfer resistance and double layer capacitance. The impedance magnitude decreases with frequency, which is typical of double layer capacitance in parallel with charge transfer resistance. The large capacitive phase angle up to 100 kHz indicates that double layer capacitance dominates at lower frequencies but that the magnitude of capacitive reactance decreases with increasing frequency.

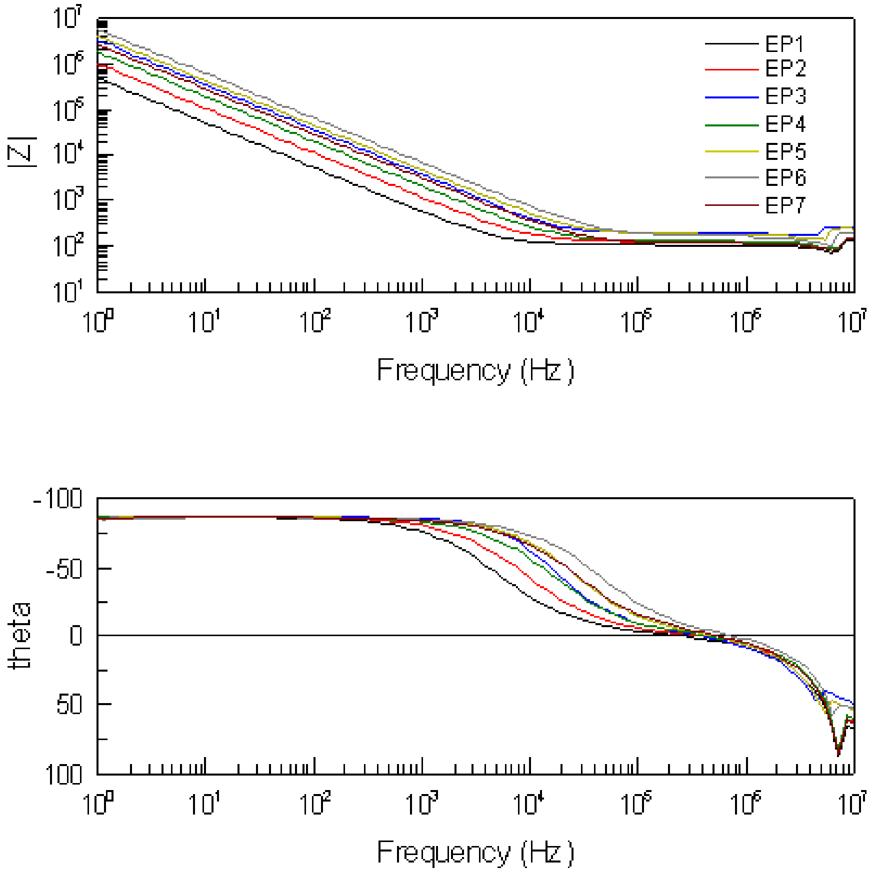

Figure 20. Device A1, measurements with alpha medium. The lowest impedance values were obtained with the largest electrode pairs (EP1, black) and the largest impedance values were obtained with the smallest electrode pairs (EP6, grey).

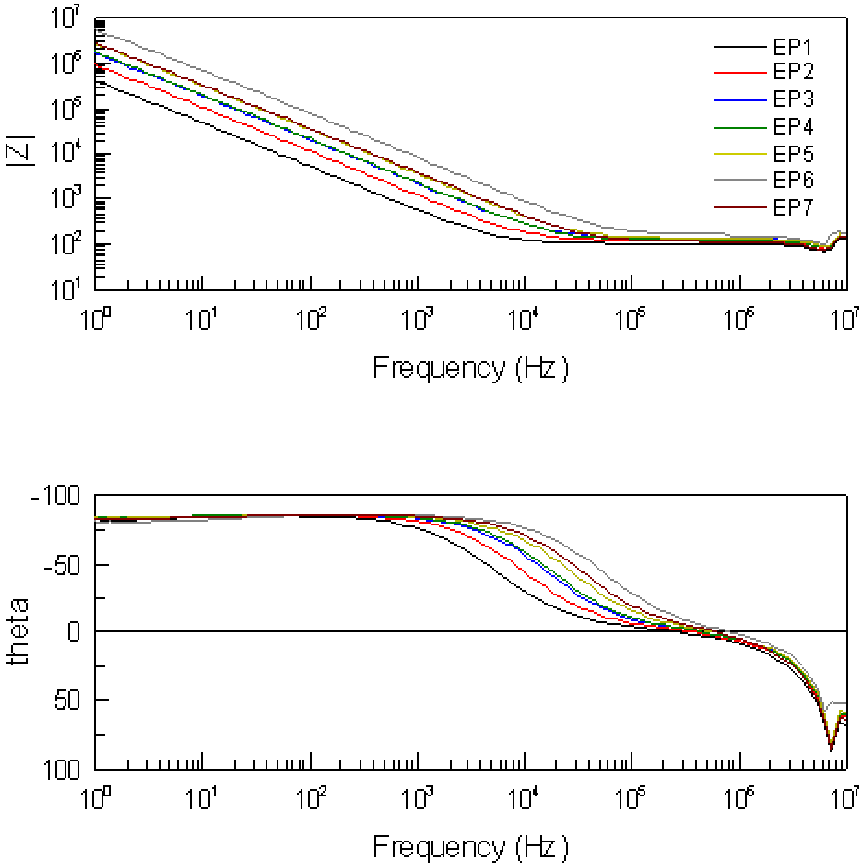

Figure 21. Device A1, the impedance spectra according to electrode size with DMEM shows a similar pattern to the corresponding measurement with alpha medium.

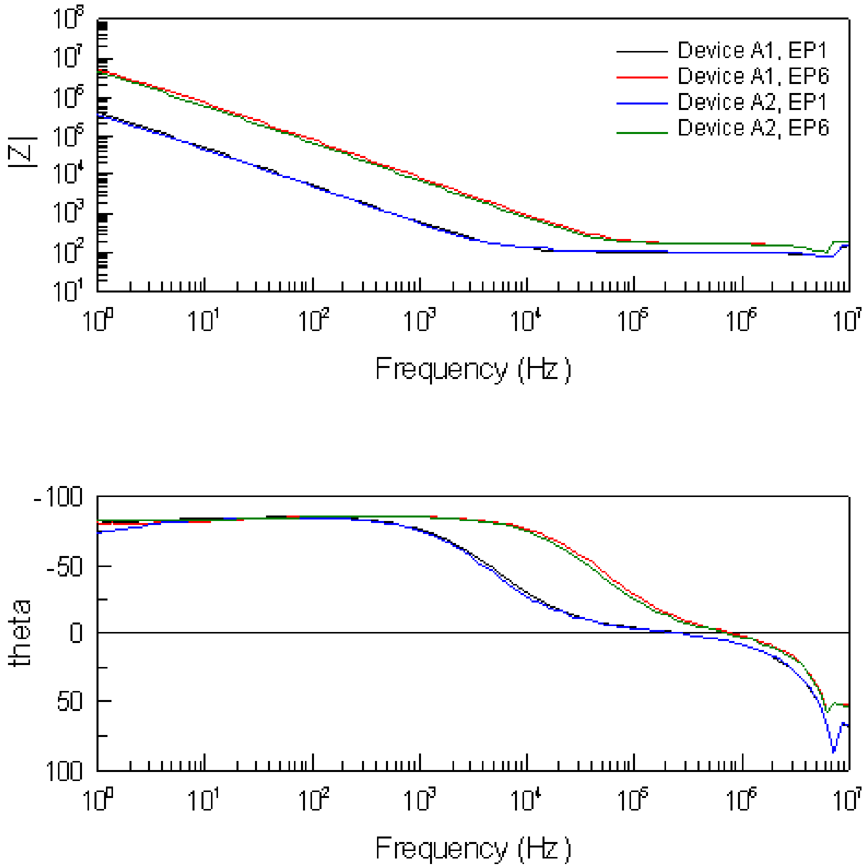

Figure 22. Impedance spectra of device A1 versus device A2 with DMEM measured with electrode pairs 1 (largest dimensions) and 6 (smallest dimensions). The measured spectra show similarity between the devices, which enables comparison of cell measurements to be made between the cultures.

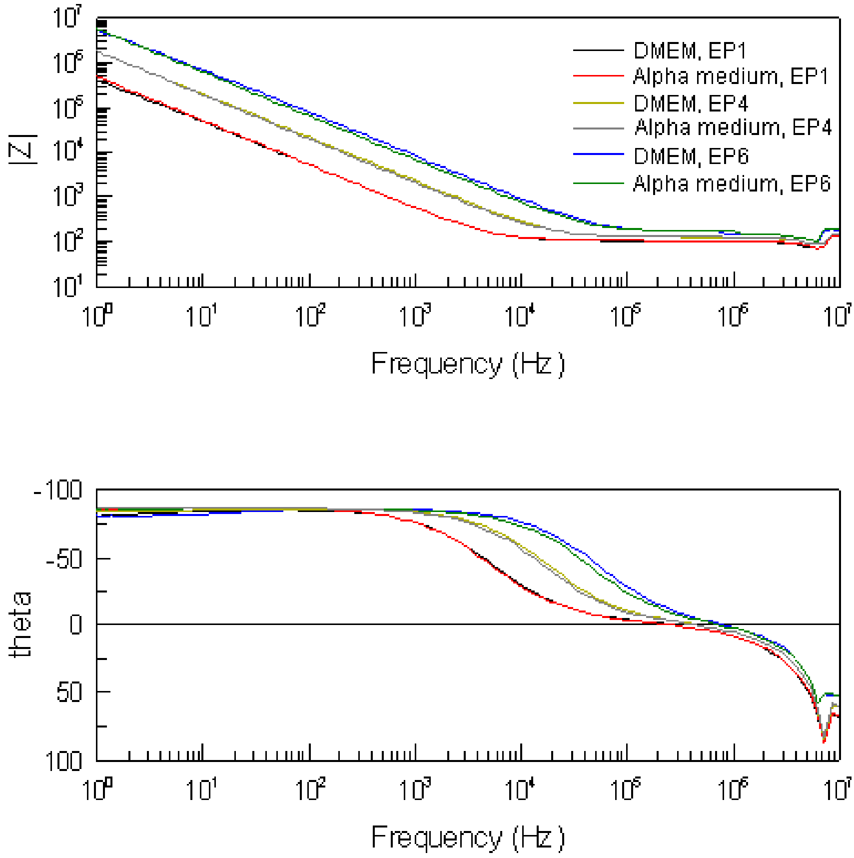

Figure 23. DMEM versus alpha medium in device A1 (electrode pairs 1, 4 and 6). Comparison of the impedance spectra of the two different culture media shows some difference in the smallest electrode pair (EP6), with the DMEM producing slightly higher impedance values.

3.4.4 Impedance measurements with cells

Changes in the cell layer condition could be seen as distinct changes in the impedance level especially between 10 kHz and 1 MHz.

One day after starting the culture, the impedance level remained at the initial (culture medium) level on electrode pair (EP) 1 in device A1. As the cell layer reached confluence five days after the start of the culture, the impedance level increased, as seen in Figure 24. When comparing the impedance phase data of culture medium vs. cell layer in confluence, it can be seen that at frequencies below 10 kHz the cell layer is less capacitive than the culture medium, indicated by the smaller phase angle data of the cells. The magnitude of impedance is higher for the cell layer than for the culture medium, indicating that the cells form a tight contact with the electrode surface, thus restricting the current flow. Above 10 kHz the phase angle of the culture medium is smaller than that of the cell layer while the magnitude of impedance is also smaller, consisting mostly of solution resistance. The cell layer growth observed with a microscope between day 1 and day 5 can be seen in Figure 25.

The impedance level remained unchanged on EP1 in device A2 as the confluence was maintained during days 3 to 7 after starting the culture (Figure 26). In addition, the phase angle plateau is observed between 10 kHz and 100 kHz. Figure 27 presents the cell layer in confluence on day 3 and day 7.

Detection of problems in a certain part of the culture is demonstrated in Figure 28. On electrode pairs 1 and 6, confluence was reached within 1 to 5 days from culture start. However, EP4 shows very little change during this time. As Figure 29 show, a cell detachment problem occurred in the middle of the culture.

Figure 30 (page 60) shows the impedance level development on a linear scale measured with EP 1, the largest electrode pair in device A2 between 10 to 100 kHz. After confluence is reached (day 7), the impedance level starts to drop (between days 11 and 18), until finally on day 21 the impedance level is close to the initial level (culture medium). The cell layer growth close to EP1 in device A2 can be seen in Figure 18 and Figure 17.

Figure 31 shows a similar impedance level development, from early culture and confluence to the final capillary structures on EP6 (smallest electrode pair) in device A1.

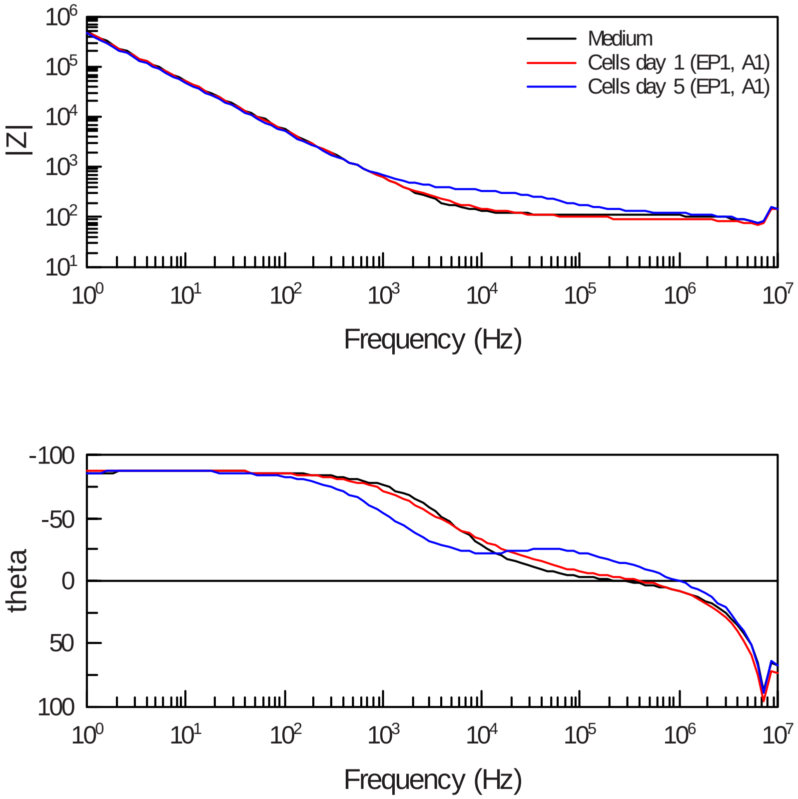

Figure 24. Cells growing to confluence (electrode pair (EP) 1, device A1) [1]. As the cell layer reaches confluence five days after the start of the culture, the impedance level increases.

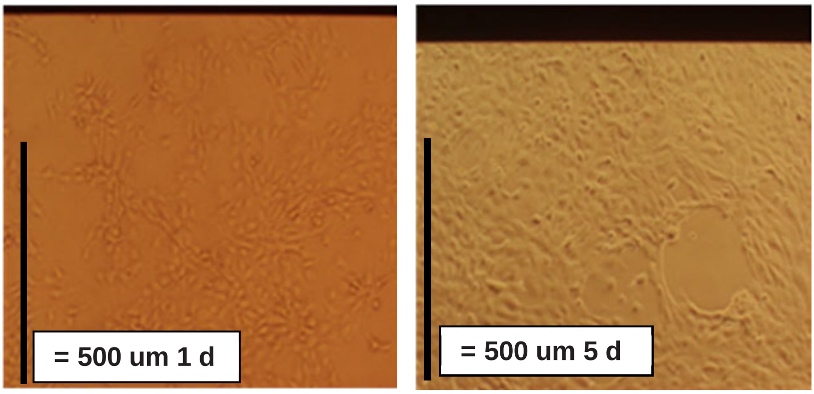

Figure 25. Device A1, electrode pair 1, 10X magnification. Change observed between 1 and 5 days after starting the culture.

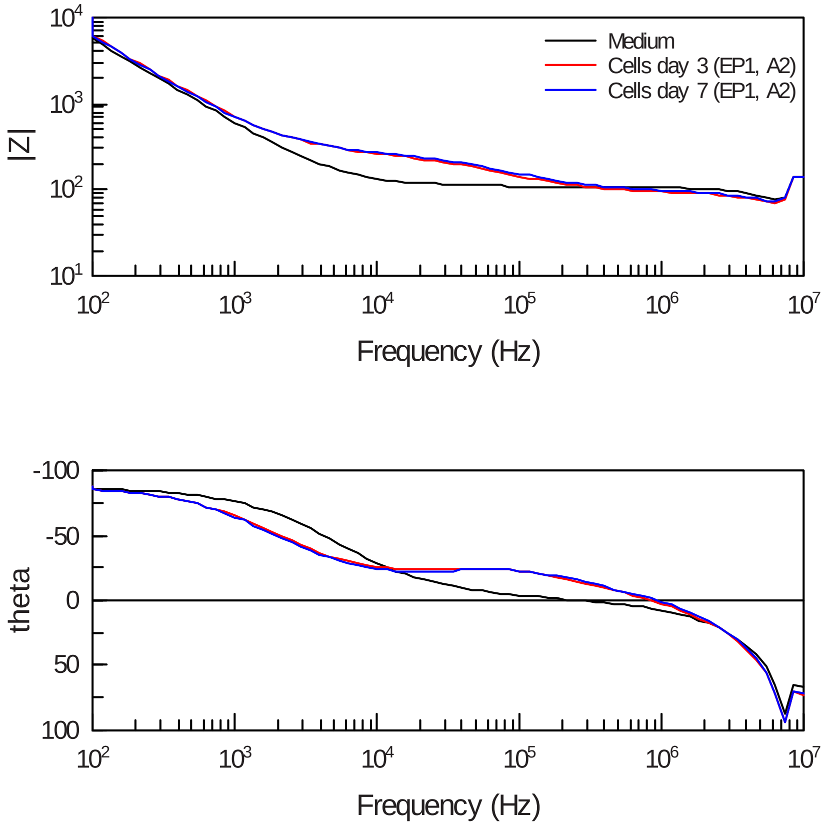

Figure 26. Maintaining confluence on electrode pair (EP) 1 in device A2.

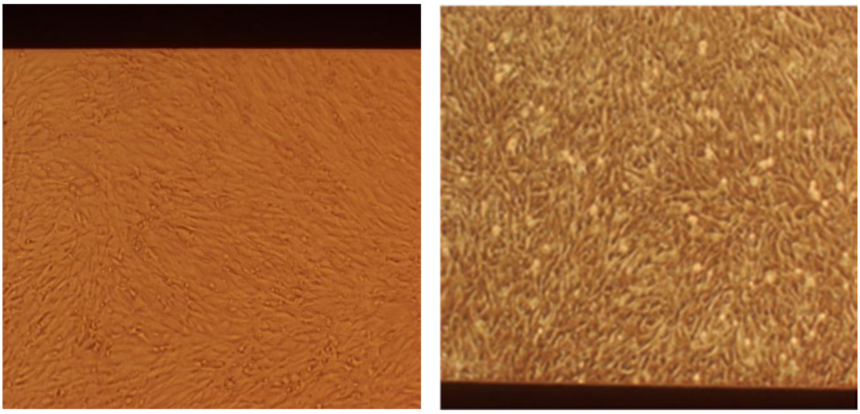

Figure 27. Device A2, electrode pair 1, 10X magnification. No change observed between 3 and 9 days after starting the culture.

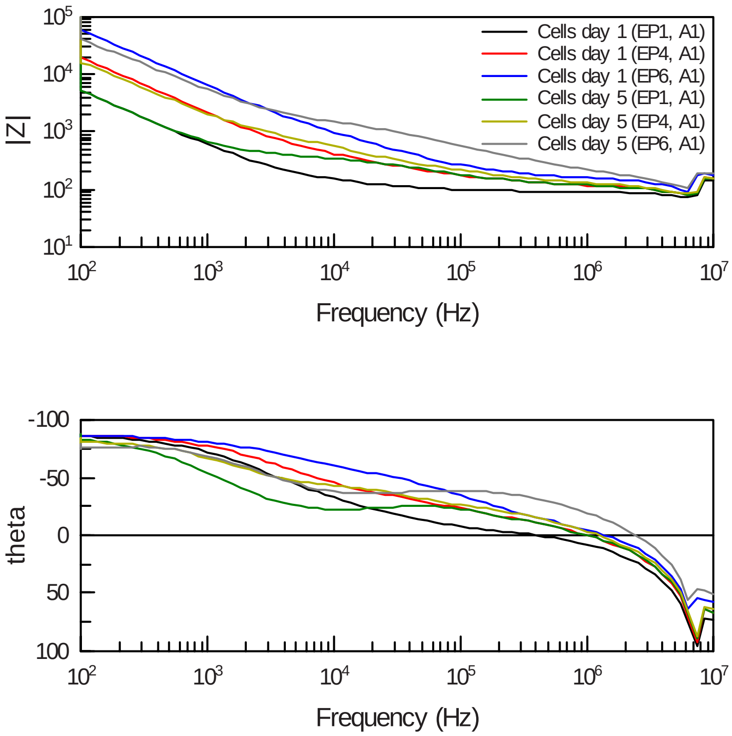

Figure 28. Detecting local cell detachment (EP 4, seen as similar curves between day 1 and 5) in the culture with measurements from different parts of the culture on electrode pairs 1, 4 and 6 in device A1 [1].

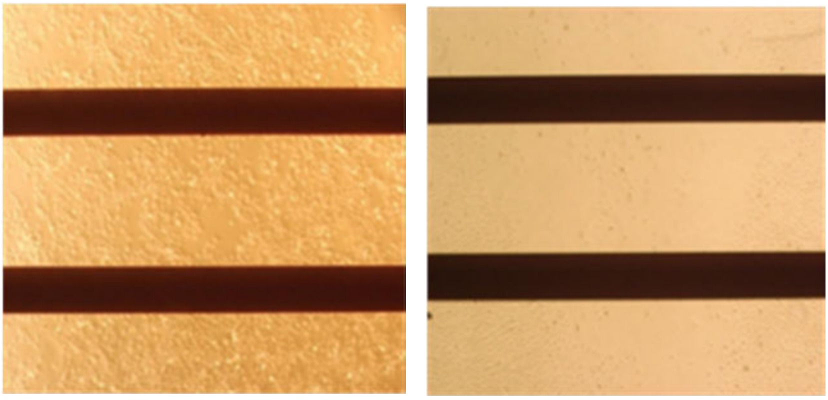

Figure 29. Device A1, electrode pair 4, 10X magnification. Electrode pair 4 on day 1 (left) and on day 5 (right). Cell growth observed from the device culture, corresponding to the red and light green impedance curves in Figure 28, shows cell detachment in the middle of the culture.

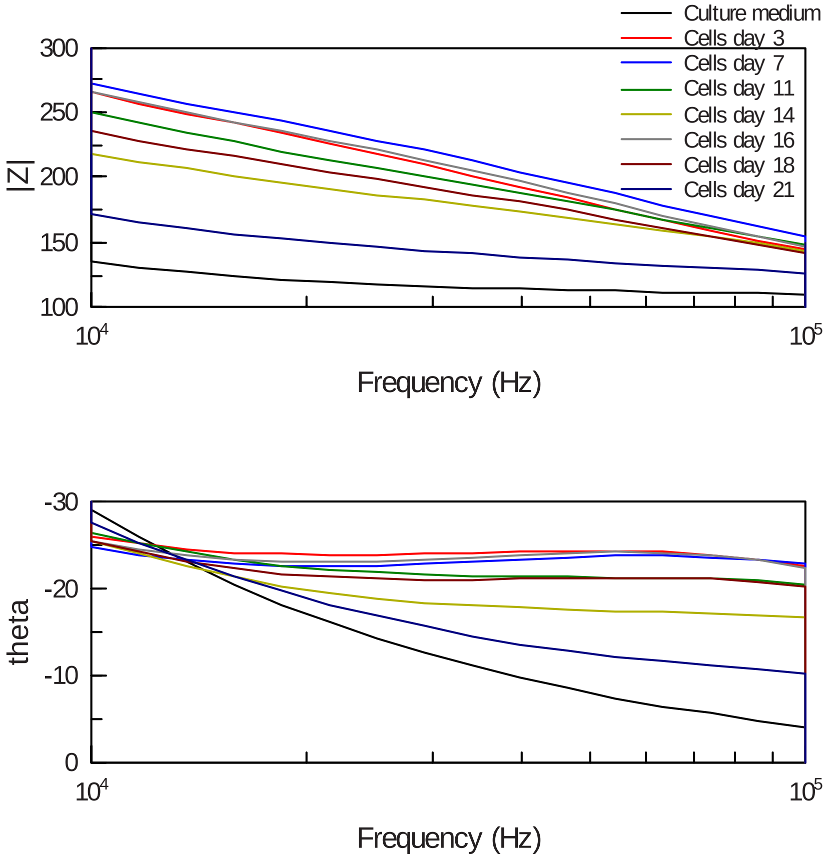

Figure 30. Impedance spectra measurement between 10 to 100 kHz showing the cell layer growth and capillary formation on a linear scale measured with the largest electrode pair (EP1) in device A2 [1]. After confluence is reached (day 7, blue), the impedance level starts to drop (between days 11 and 18), until on day 21 (grey) capillaries are formed and the impedance level is close to the initial level (culture medium, black).

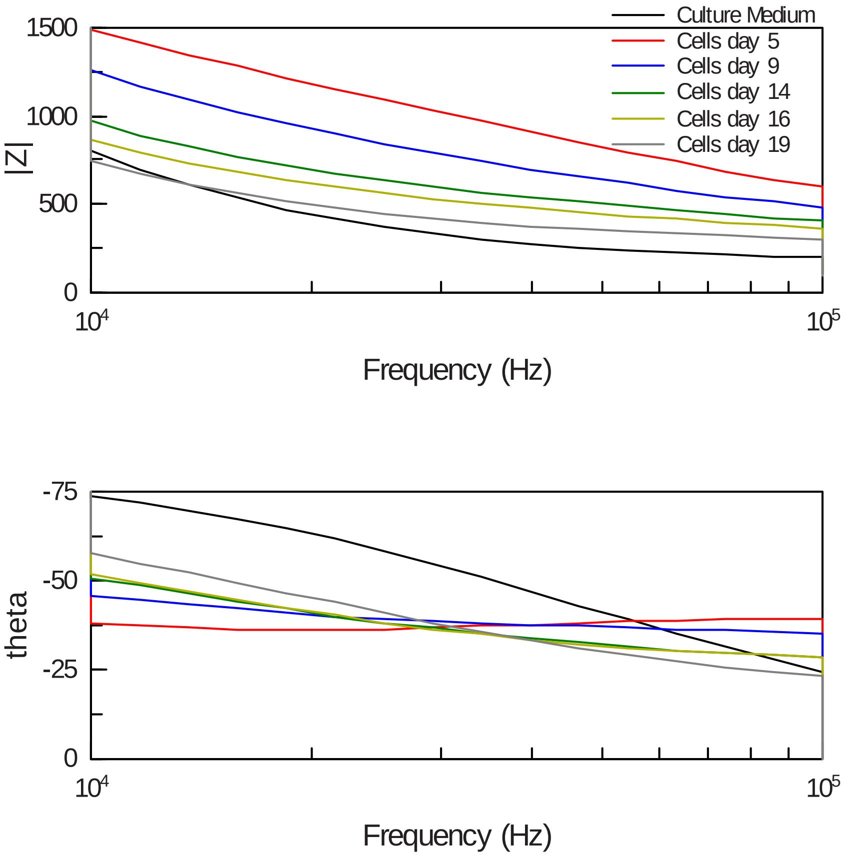

Figure 31. Impedance spectra development between 10 to 100 kHz according to the cell layer growth and capillary formation measured with the smallest electrode pair (EP6) in Device A1). After confluence is reached (day 5, red), the impedance level starts to drop (between days 9 and 16), until on day 19, after capillary formation, the impedance level is close to the initial level (culture medium, black).

When comparing the measured impedance spectrum of the culture cycle with the largest electrode pairs EP1 (Figure 30) and smallest electrode pairs EP6 (Figure 31) it can be seen that the impedance magnitudes on the largest electrode pairs are smaller than those on the smallest pairs, as expected. It is interesting to see the difference in the phase angle data. When the culture reaches confluence (days 3–5) the phase angle between 10 kHz and 100 kHz remains constant throughout the spectrum, but as the growth progresses and the cells develop an elongated structure, the phase angle increases at low frequencies and decreases at high frequencies, a slope which indicates a change in capacitive reactance. This dispersion behaviour is affected by the electrode size.

In Figure 30, the centre of the phase angle dispersion, i.e. the frequency at which all impedance data curves have the same phase angle, is at approximately 15 kHz and the phase angle magnitude across the spectrum is much smaller, ranging from the maximum -30° to -5° from 10 to 100 kHz. For the smallest electrodes in Figure 31, the centre of the phase angle dispersion for all cell measurement data lines is at 30 kHz and the phase angle magnitude ranges from -60° to -25°, indicating that capacitive reactance is more dominant. It should also be noted that, unlike with the larger electrodes, the phase angle curve for the culture medium does not meet the centre of dispersion for the cell measurement curves. This helps to differentiate between the causes of the change if examining impedance magnitude values alone is not sufficient.

To observe the relative impedance level change, the comparison was done with the impedance magnitude values at the centre of the phase angle dispersion, i.e. at 15 kHz for the largest electrodes and at 30 kHz for the smallest electrodes. The confluence ratio (R_{conf}) was obtained by comparing the impedance magnitude of the culture at confluence with the initial impedance level with culture medium:

$$R_{conf} = \frac{\left|Z_{conf}\right|}{\left|Z_{\min}\right|} \tag{13}$$

The capillary ratio (R_{cap}) was obtained similarly by comparing the impedance level of the cell layer having fully-developed capillary structures with the initial level with culture medium:

$$R_{cap} = \frac{\left|Z_{cap}\right|}{\left|Z_{\min}\right|} \tag{14}$$

The results are presented in Table 2 and Table 3. At 15 kHz (ω = -25°), the confluence ratio is 2.1 and the capillary ratio had an average of 1.3. At 30 kHz (ω = -38°), the confluence ratio is 3.1 and the capillary ratio had an average value of 1.3.

Table 2. Confluence ratio.

Confluence:		
Frequency (kHz)	15	30
Electrode Pair.	EP1	EP6
$\lvert Z(\text{min})\rvert$ / [Ω]	125	350
$\lvert Z(\text{conf})\rvert$ / [Ω]	260	1100
$\lvert Z(\text{conf}\lvert Z(\text{min})\rvert$	2.1	3.1

Table 3. Capillary ratio.

Capillaries:		
Frequency (kHz)	15	30
Electrode Pair	EP1	EP6
$\lvert Z(\mathrm{min})\rvert$ / [Ω]	125	350
$\lvert Z(\mathrm{cap})\rvert$ / [Ω]	160	450
$\lvert Z(\mathrm{cap}\rvert/Z(\mathrm{min})\rvert$	1.3	1.3

3.5 Discussion

Based on the measurement results, it can be seen that the capillary formation of the endothelial cells produces a drop in impedance level. The reasons behind this phenomenon are discussed below.

One factor might be reduced adhesion due to cell migration [105]. As the cells begin to differentiate and move into structures, they cannot be adhered to the surface as tightly as when there is confluence and when migration has not yet begun. In this case, there is more space between the cells and the electrode, and the more the culture medium is in direct contact with the electrodes. The cell-to-surface adhesion mechanism has an effect on the measured impedance level and cell adhesion to the electrodes can be enhanced with covalently bound adhesion peptides vs. physical adsorption of similar peptides to the SAM layer [106], resulting in higher impedance values. In the experiments reported in this thesis, the SAM layer provides the binding site for the adsorbed fibronectin and cell-fibronectin contacts, so binding is expected to be less strong than with covalently bound peptides. In addition, other peptides present in the FBS supplement also affect the binding properties, such as adhesion rate, proliferation and viability of endothelial cells [107]. Other research teams have addressed this current issue of the dynamic nature of cell adhesion and detachment by developing a biological breadboard platform capable of spatiotemporal control of fibroblast cell adhesion [108].

The impedance is inversely proportional to the active electrode area. If cells grow adherently on an electrode, the electrode effective area is decreased and the impedance is increased [109]. In the reverse situation, there is more active electrode area, and the impedance is decreased. This may also be the reason for the larger confluence ratio obtained with the smaller electrodes. The effect of a confluent cell layer on electrode double layer capacitance is larger than when there are capillary structures present and there is more culture medium between the cell monolayer and the electrode surface.

This reduction in cell adhesion was also evident in the reference culture in the Petri dish. Normally, great care must be taken when inserting new culture medium to avoid peeling of the cell layer. In these experiments, however, cell layer peeling never occurred during confluence.

Other than reduced adhesion, the electrode effective area may also be increased due to the area exposed between the cells as they form into these structures. However, no such electrode surface exposure was observed under the microscope.

It was, however, observed that electrode surface exposure may occur at the sides of the culture area, thus, naturally increasing the electrode area in the measurements. However, the condition at the sides of the culture remained relatively unchanged throughout, indicating that electrode surface exposure on the sides does not add to the impedance decrease caused by capillary formation, but rather it may create inconsistencies in the impedance levels obtained from the measurements of different devices.

3.6 Conclusions

Bovine adrenal cortex endothelial cells are known to have good capability of creating capillary-like structures in stable Petri dish cultures. The present study showed, however, that these cells also have the capability to form capillaries when cultured in a microdevice environment on electrode structures. The BACC-EC formed capillaries after one month when using DMEM as the culture medium. When using alpha medium, the capillary structures started to form already after 2 weeks and were complete before 3 weeks, indicating that alpha medium was more favourable as a growth medium.

The cell growth and cycle was successfully monitored with microelectrodes in a PDMS-glass microdevice using impedance spectroscopy. The condition (confluence, cell death, capillary formation) of the cell layer was seen as distinctive changes in the impedance spectra.

Capillary formation was indicated by a drop in impedance magnitude level, especially between 10 and 100 kHz. In confluence, the impedance values measured from the cell monolayer were 2.1 (largest electrodes) to 3.1 times (smallest electrodes) higher compared to the minimum impedance level. With observed capillary structures throughout the cell culture, the impedance values were on average 1.3 times higher than the minimum, independent of the electrode size. The electrode size affects the magnitude and phase dispersion of the measured impedance.

The capability to use EIS for the characterization of endothelial cell capillary formation in a microdevice may in future enable novel methods for the monitoring of cancer drug therapies.

4. Nanocalorimetric thermal characterization of yeast cells

4.1 Introduction

Most biological processes are accompanied by thermal activity. Thermal measurement is also an attractive choice as a characterization method. It does not require the use of reactant labelling, the sample can be in a liquid form without the need of surface attachment of the measured biomolecules, and it can be used for many different kinds of processes, for example cell metabolism measurement, protein folding and unfolding detection and enzymatic activity measurements. However, calorimetry as a technique is not specific, as the heat produced by different biochemical reactions cannot be distinguished.

Whereas traditional calorimetric measurement devices require large sample volumes, MEMS technology enables the manufacture of low-cost integrated devices which require very small sample volumes, thus reducing the cost of analysis. MEMS calorimetric sensors also offer other advantages, such as improved sensitivity and linear range due to improved thermal isolation, reduced thermal mass and sample volume, reduced power consumption, and shortened measurement times [110]. MEMS calorimeters can also be used for high-throughput parallel measurement arrays.

Calorimetric MEMS sensors are typically based on either thermopiles or thermistors. Thermistors detect heat as a change in resistance and allow measurement of absolute temperatures, but are less sensitive than thermopiles, which detect the temperature difference as a voltage difference between the hot and cold junctions of the thermocouples. The voltage of the thermopile is the sum of the thermocouple voltages. MEMS thermocouples are typically made of metals or semiconductors, and are fabricated on free-standing membranes or bridge structures to improve thermal isolation.

MEMS chips have been used to measure droplet evaporation enthalpies, as shown in Figure 32 by Gross et al. [111]. Droplet placement on the microcalorimeter is seen as a drop in the measurement curve and, as the droplet evaporates, a return of the temperature to the starting point.

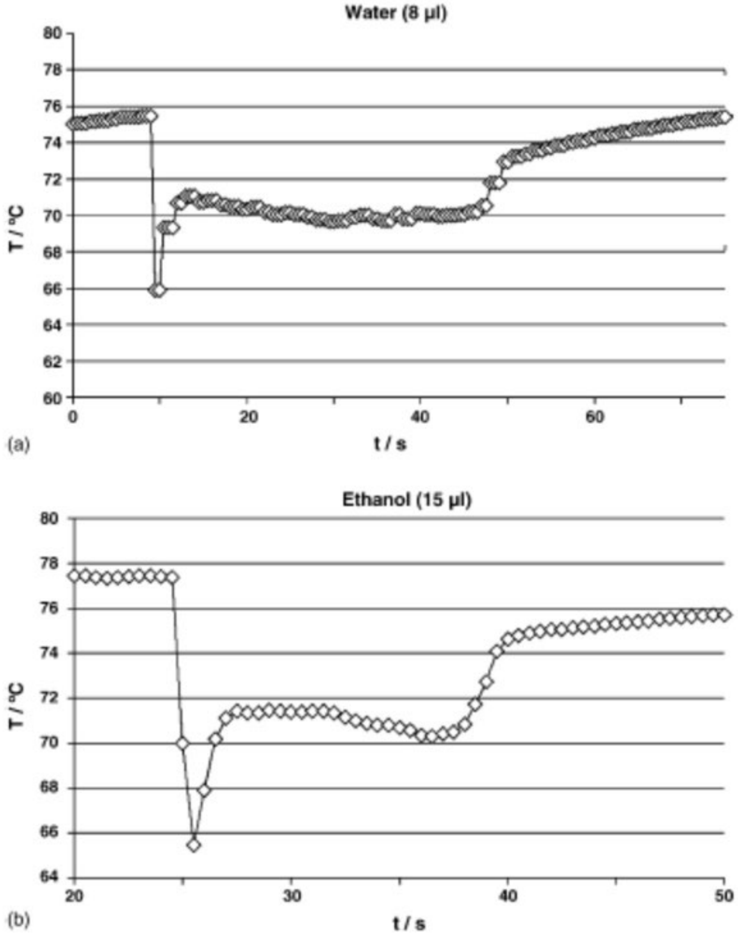

Figure 32. Temperature signal during pipetting and evaporation of a water and ethanol droplets: (a) 8 µl; (b) 15µl measured at a constant heating power of 1.4W, by Gross et al. [111].

Calorimetry is an excellent tool for monitoring cell metabolism, since cellular growth is always accompanied with the production of heat, and the amount of heat that is dissipated is related to the rate of substrate consumption and product formation in the culture [112]. The growth of yeast cells consists of different stages, depending on the energy source of the cells. Calorimetry enables determination of the growth phase of the cell culture. Thus, the metabolic cycle can be controlled, for example, by adding more nutrients to maintain the fastest cellular growth phase.

Microcalorimetry has previously been used in several ways to study cultures of Saccharomyces cerevisiae: the tolerance of sudden osmotic dehydration [113] or osmotic shock [114], physiological structure during cell cycle oscillations [115], identification and control of oxidative metabolism [116], identification of population structure and expansion kinetics [117], protein oxidation [118] and the catabolic capacity during carbon and nitrogen starvation [119]. Microcalorimetry has also been used to study the interaction between T4 phage and Escherichia coli [120]. Most of these measurements were conducted in a macro-scale microcalorimeter (micro- referring to the accuracy of the device, not the size). However, for measurement on smaller scale devices, a nanocalorimeter has been developed which is capable, for example, of performing measurements on single liver cells [121].

Traditional microcalorimetric measurement systems are large and, as such, more expensive compared to microsensors. They also require large sample volumes, which make them less cost-effective. For this reason, it is of great interest to develop smaller and less expensive calorimetric tools based on MEMS micro-or nanocalorimetric sensors to enable monitoring of very small samples volumes or cell cultures. In this work, the ability to use MEMS nanocalorimetric sensors for monitoring the metabolic activity of small populations of *S. cerevisiae* is tested and evaluated [2].

4.2 Yeast cell metabolism

The cell cycle (Figure 33) of *S. cerevisiae* consists of duplication of the nuclear material and formation of a new cell. The population is heterogeneous and consists of cells which are able to bud and daughter cells which expand in volume and mass [117]. The majority of cells are at the same phase of the cell cycle at the same time, which means that the cells are synchronized and the culture is oscillating. However, individual cells have different properties, such as age or size, and can form distinguishable subpopulations.

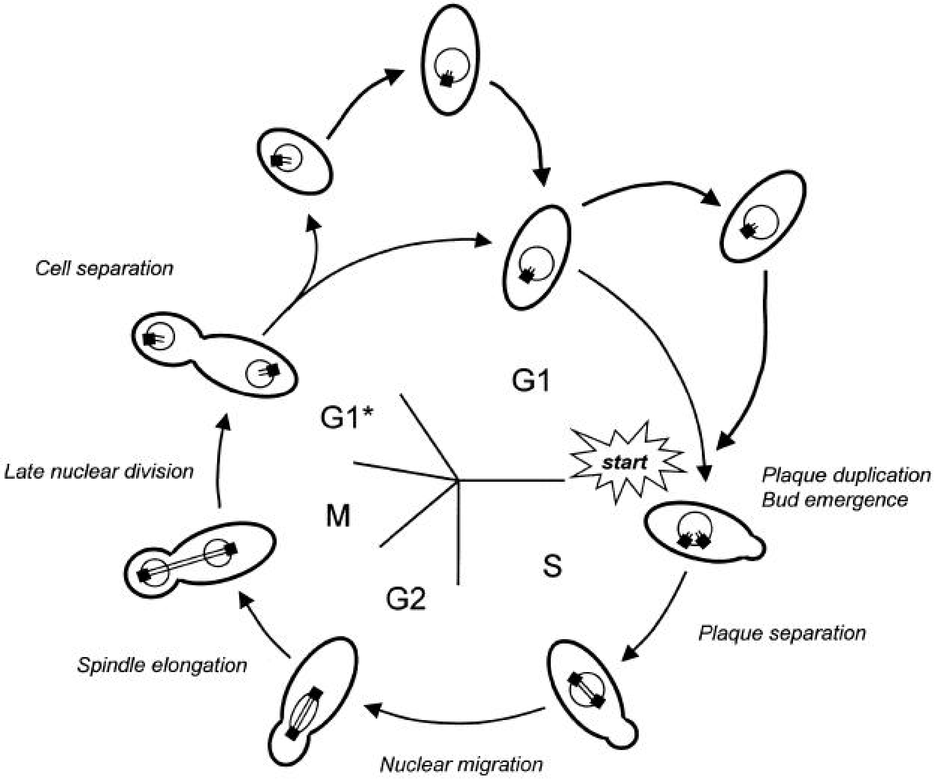

Figure 33. The cell cycle of S. cerevisiae by Duboc et al. [117].

During the first growth phase of *S. cerevisiae*, the cells use glucose as a carbon and energy source and produce ethanol and small amounts of glycerol and acetate. During this respiro-fermentative metabolism, the growth and heat production rates are at their maximum levels. As the glucose supply becomes inadequate (Figure 34), there is a drop in the heat production rate and between the first minimum and the second maximum all of the glucose is consumed from the culture. The cells then start using the previously produced ethanol as the energy source, and the growth rate slows. When this ethanol is depleted another drop occurs, followed by a plateau in the heat production rate curve, which represents the consumption of acetate [112].

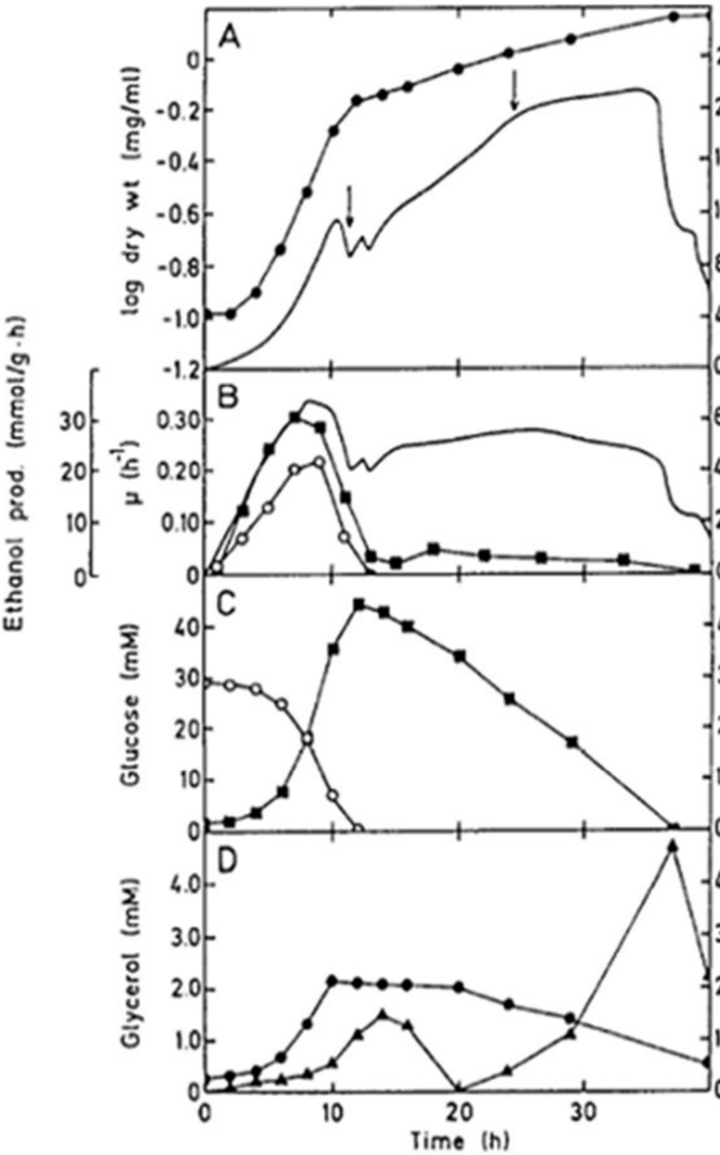

Figure 34. Yeast cell cycle monitoring by Larsson et al. Plot A) shows the mass production related to heat production, B) the ethanol production rate, C) glucose consumption (hollow circles) with regads to ethanol production (squares) and D) the levels of glyserol (circles) and acetate (triangles).

4.3 Nanocalorimetric sensor

The sensor used in these experiments is a thermal MEMS sensor fabricated at VTT by J. Saarilahti [122], referred to as a nanocalorimeter due to its miniature size and its nanowatt detection range in the gas measurements for which it was originally developed. It consists of four thermopiles, each with 35 thermocouples. The temperature difference between the hot and cold junctions (Figure 35) of the thermocouple creates a voltage difference between the junctions. The output voltage of the thermopile is the sum of the thermocouple voltages in series. The hot junctions are located in the measurement area, which is a thin nitride membrane with polysilicon heat equalizing plate (Figure 36), and the cold junctions are on the sensor substrate. The silicon has been etched away from beneath the membrane in order to ensure good thermal insulation and to avoid thermal conduction between the hot- and cold junctions of the thermocouples. There is also a thermal resistor in the measurement area, which is used in the calibration of the sensor and can also be used to heat the sample or to measure the absolute temperature.

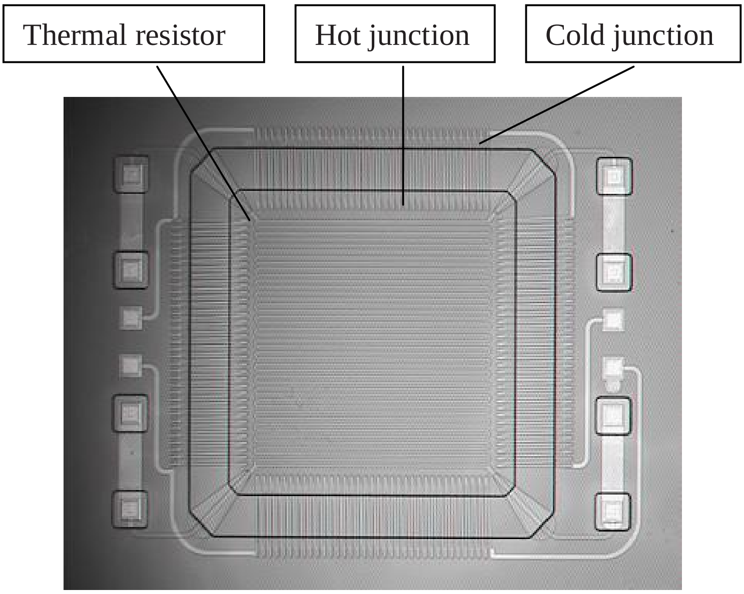

Figure 35. Sensor type A with 150 µm insulation distance between the hot and cold junctions [122]. A thermal resistor runs through the entire central membrane area, with thermocouple hot junctions at the membrane edges and cold junctions on top of the substrate.

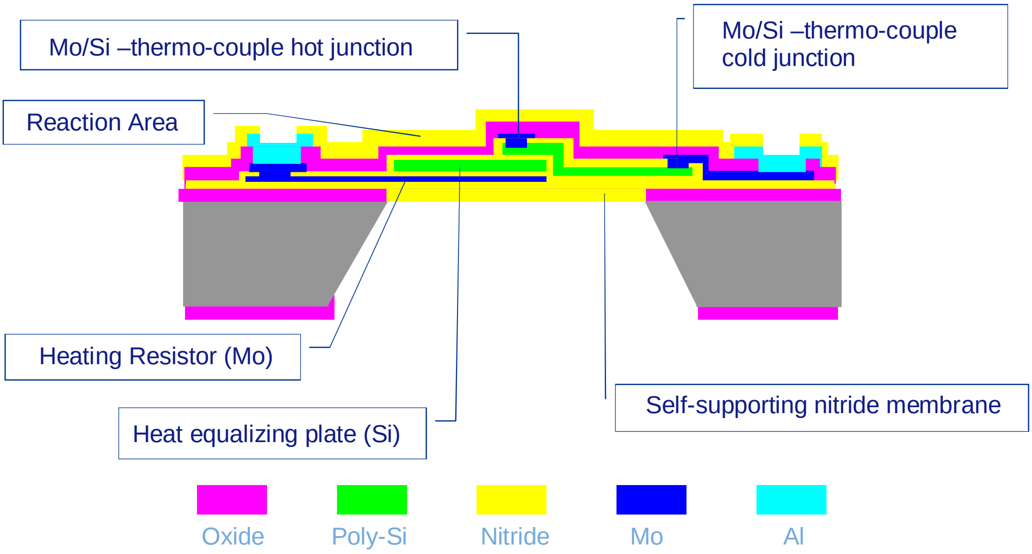

Figure 36. Nanocalorimeter cross section [122].

The sensor can be used either in the position shown in Figure 36, or in the upside-down position. When placing the sensor upside down, a fluid container can be placed on top of the sensor to create a closed measurement chamber. In the upright position, the measurement area can only be covered so that the wiring is also enclosed, which leaves an empty space between the measurement sample and the cover and thus leaves more room for evaporation. The calibration constant ε_c of the sensor can be determined by measuring the thermoelectric voltage induced in response to an electric power applied to the membrane heating resistor [122]. Without liquid droplets, the responsivity of the sensors has been determined to be 16V/W, and the thermo voltage per thermocouple as 0.161 mV/K [123]. With the fluid container in the upside-down position and with 20 µl of stagnant water in the chamber, the responsivity has been determined to be 2.9 V/W [123]. This is only 18% of the responsivity without a liquid sample present. This is due to increasing thermal conductance to the substrate caused by water, resulting in a smaller temperature difference between the hot and cold junctions of the thermopile.

The respiratory heat production of the cells was estimated using the value obtained by Larsson et al. [112], namely 100 µW of heat from a volume of 0.331 ml with 1e6 cells/ml. Based on this, one cell fermentation unit (CFU) can be assumed to produce approximately 0.3 nW of heat and thus 1 * 10^6 cells would produce 0.3 mW. If the measurements are done in differential scanning calorimetry (DSC) mode, the thermal voltage produced by the cells is

$$\Delta V_{cells} = V_{o1} - V_{o2}, \tag{15}$$

where V_{o1} is the total thermopile output voltage of the cell droplet and V_{o2} is the total thermopile output voltage of a reference water droplet. Thus, the heat loss due to evaporation is extracted from the heat generated by the cells.

If the responsivity *K* of the sensor is known, the heat power produced by the cells (Eq. 7) can be derived from the differential thermopile output voltage,

$$P_{cells} = \frac{\Delta V_{cells}}{K}. \tag{16}$$

The power sensitivity of the measurement system varies according to the size of the liquid droplet, but it can be estimated that with the lowest sensitivity (responsivity 2.9 V/W) the differential thermopile output of the sensor would be $\Delta V_{cells} = P_{cell} * K = 0.87$ mV and with the highest possible sensitivity (responsivity of 16 V/W) $\Delta V_{cells} = 4.8$ mV for $1 * 10^6$ cells, differentially compared to a reference water droplet to eliminate evaporation. Since these values are relatively high (~mV range), it might be possible to use the nanocalorimeter to monitor yeast cell heat production.

Figure 37 presents a simulation of a small droplet on a SiN membrane, representing the heat distribution in the membrane and the Si structure. The heat production corresponds to a population of ~3000 yeast cells in their first growth phase, supposing that the heat loss due to evaporation is zero. When evaporation is not present, the temperature of the yeast cells droplet would be +9°C degrees higher than at the edge of the sensor, however as heat is dissipated into the structure, the difference between the hot and cold junctions would be about half of this, at 4–5 °C.

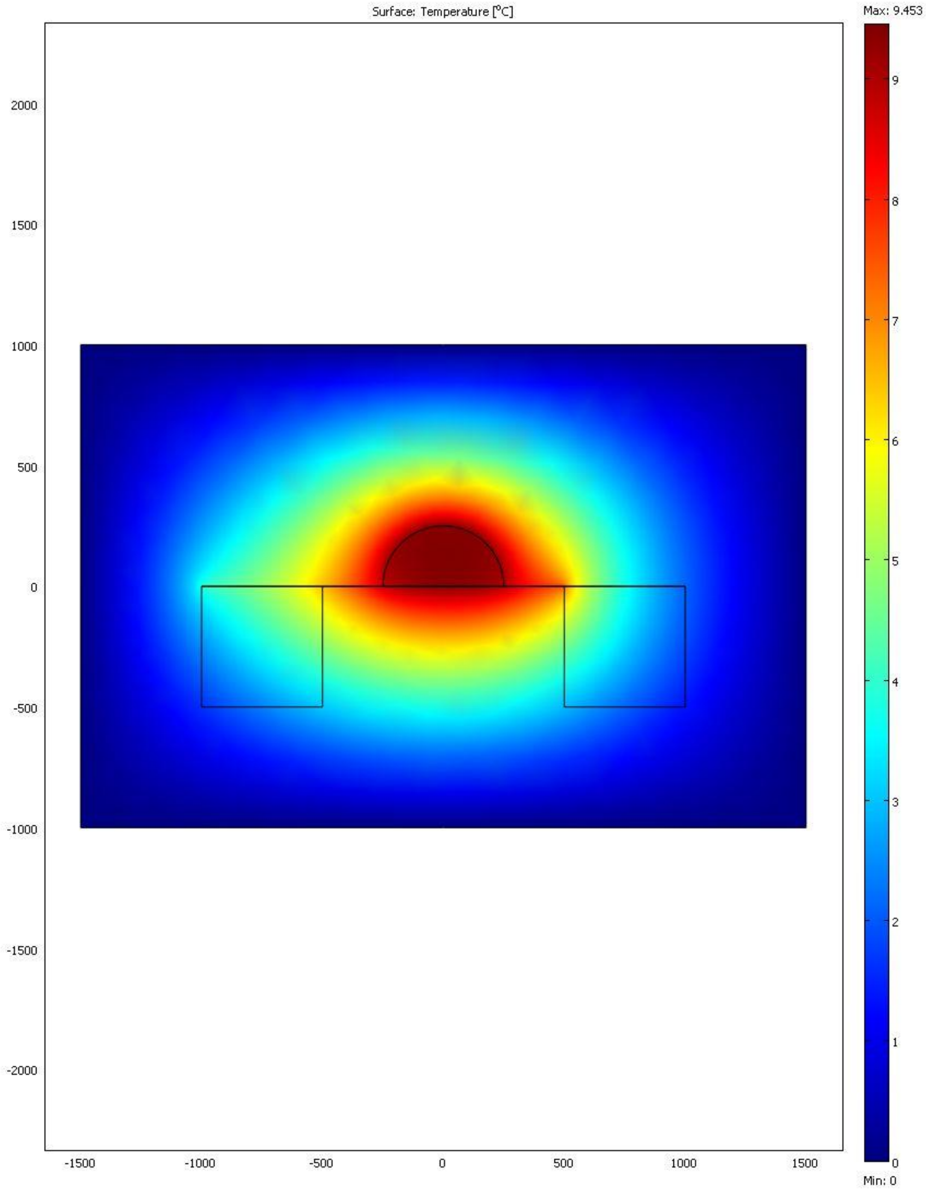

Figure 37. Simulation of a small droplet producing 1 µW heat on a SiN membrane fabricated on silicon, courtesy of Ari Hokkanen. The distance from the centre (droplet on the sensor membrane) is given in micrometers in the x- and y-direction, the temperature difference is indicated in colour (blue indicating 0 °C difference to ambient room temperature). A cross-sectional view of the sensor shown in Figure 36.

4.4 Experimental

4.4.1 Cells

Saccharomyces cerevisiae (strain CEN.PK113-1A) was cultivated in 50 ml of minimal growth medium containing 2% glucose o/n until optical density (A600) of 2–10 was reached (courtesy of VTT Bio). The cells were collected by centrifugation at 3000 rpm (2 min) and washed once with distilled water. The cells were then resuspended in growth medium containing 2 % glucose to obtain a density of $0.5 * 10^5$-$1 * 10^6$ cells / µl. The resuspension was done 2 to 3 hours before the measurement in order to ensure that the cells were in the first growth stage and able to produce the highest amount of heat.

4.4.2 Experimental set-up

Measurements were done at room temperature with an Agilent 34970A Data Acquisition / Switch Unit with HP34901A 20 channel multiplexer, which was connected to a PC for controlling and data handling through HP BenchLink Data Logger software. Each sensor was tested for normal operation prior to measurement by measuring the sensor's reaction to heat.

Two different detachable covers A (thick metal) and B (ceramic), seen in Figure 38 were used with the sensor in an upright position, and a closed fluid container with approximately 20 µl fluid volume (Figure 40) was used with the sensor in upside down position. The fluid container was made of plastic and contained an inlet and an outlet for fluid piping, and an o-ring, which was pressed against the sensor to create a sealed sample volume. The fluid container was held tightly in place with rubber bands.

When using either of the covers, the sensor was placed in a metal box with the necessary wiring connected to the multiplexer, and the cells were pipetted as droplets (size 1–10 µm) onto the centre of the sensor membrane (Figure 39). The cover was then placed on top of the sensor to minimize evaporation, and the metal box containing the sensor was closed with either one (cover A) or two (cover B) covers to ensure thermal isolation and to minimize evaporation. When using the fluid container, the cells were injected with an injection needle through plastic piping. The minimum amount of cells used in the device was 10,000, and the maximum was 10 million. The cell density range was from 1,000 to 1,000,000 cells/µl. After each measurement, the sensor and other parts of the measurement system were washed with isopropanol and water.

Cover B proved to be better than cover A in terms of evaporation while leaving sufficient space for the droplet inside the cover. When using the sensor in an upside-down position with the fluid container, the droplet is in contact with the substrate of the sensor and the sensitivity decreases. Sensitivity was also better on small droplets (< 5 µl) than on 10 µl droplets, as the larger droplets occupy a larger surface area and may thus come into contact with the cold thermocouple junctions, decreasing measurement sensitivity.

Figure 38. System with cover A (left) and cover B (right) for measurements with the sensor in the upright position. Cover A provides thick insulation but leaves more space for evaporation than cover B, which provides sufficient space for the droplet but no extra room for evaporation.

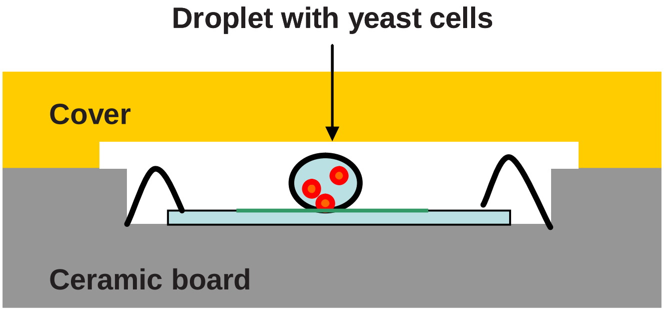

Figure 39. The measurement set up with the nanocalorimetric sensor wire-bonded to the ceramic substrate, with droplet with yeast cells on the sensor membrane.

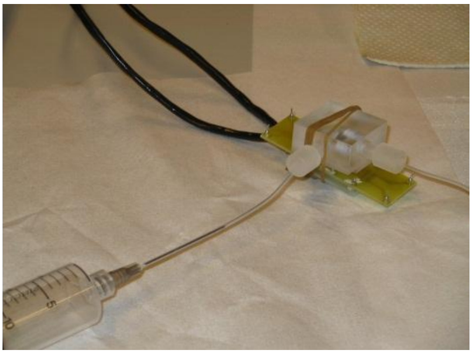

Figure 40. System with fluid container, used with the sensor in the upside-down position. Leaves no room for evaporation, but thermal conductivity of the substrate decreases measurement sensitivity.

4.5 Results

Observed heat loss due to evaporation was the dominant factor in the measurements, and thus the measurement curves obtained resembled those of the typical droplet evaporation experiments by Gross et al. [111] in Figure 32. To extract the heat loss due to evaporation from the heat energy created by the cells, a reference measurement comparing a yeast sample droplet to a water droplet of the same size is necessary, preferably performing the measurements simultaneously as in differential scanning calorimetry.

Figure 41 shows typical voltage output measurement patterns for 2 µl droplets of water, yeast cell sample and ethanol, taken on a sensor in an upright position with a cover to minimize evaporation. Initially, there is a sharp negative drop in the sensor output voltage when the droplet is placed on the membrane and the cover is placed over. With water, the voltage output curve then stabilizes to a plateau with small fluctuation (less than 100 µV) caused by environmental effects. The cell sample, on the other hand, shows a rising voltage output curve (> 400 µV) measured from the initial voltage base level due to the heat generated by the cells. The ethanol droplet does not maintain any voltage base level as it evaporates very fast and the output voltage drops constantly. The output voltage baseline levels for each measured droplet in Figure 41 are $V_{O,H2O}$ ~-11 mV, for cell droplet $V_{O,\text{ cells}}$ ~-4 mV and for ethanol $V_{O,\text{ ethanol}}$ ~1.5 mV. The difference between sensor output voltage for water and the cell droplet is thus ΔV_{cell} ~7 mV. It might be expected for the ethanol droplet to show the greatest negative output voltage, but as the surface tension of an ethanol droplet is low, the droplet is completely wetted on the surface creating a shortcut between the hot and cold junctions of the sensor and thus decreasing the sensitivity, which can be seen as a low value in the differential voltage output signal. As the thermal responsivity varies according to the liquid in question and the size and the position of the droplet, quantitative extraction of the exact amount of heat produced by the cells cannot be made. It can only be concluded that there is a distinguished difference in sensor signal behaviour between the cells and the reference droplets.

For 10 µl droplets with a total of $10 * 10^6$ cells, the thermopile output voltage was ~-2.5 mV, while for a reference water droplet the voltage was -8 mV, the voltage difference being 5.5 mV. This is in the range of the expected calculated value (with 2.9 V/W responsivity and 0.3 nW/CFU) of 8.7 mV.

However, based on these values it is not possible to make an exact calculation of the heat produced by the cells, as there is a systematic error of about +-1.5 mV caused by pipetting and fluctuations in the droplet placement and size (Figure 42), which is discussed next.

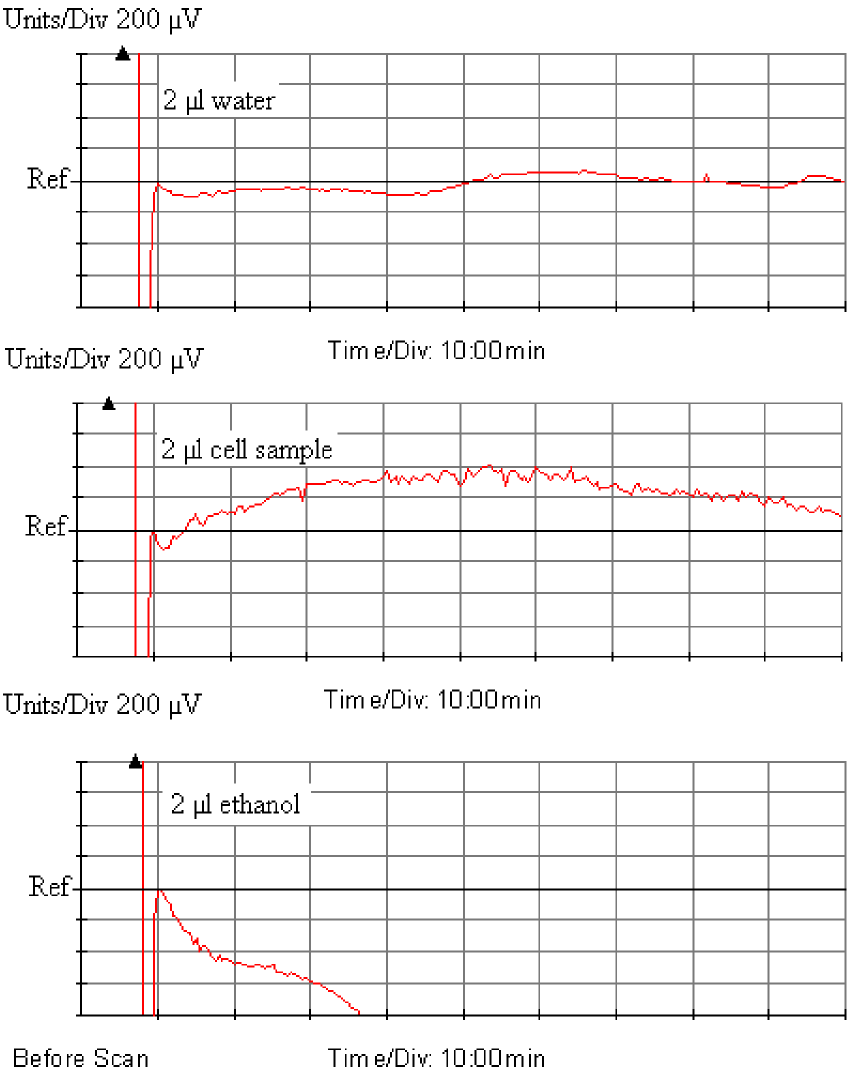

Figure 41. Typical measurement curves. Evaporation of 2 µl droplets of water, cell sample (1x10^5 cells) and ethanol [2].

The measurements showed that the cells generate heat, which can be seen in the droplet evaporation pattern created by the sensor voltage output curve. However, to be able to extract the heat generated by the cells by parallel sensor array measurements, the reproducibility of the droplet placement on the sensor needed to be assessed. This was done by the measurement shown in Figure 42, in which sequential droplets were placed on the membrane and the plateau of the output voltage was monitored. The measurement showed that the base level or plateau which is obtained during each droplet measurement varies by several millivolts due to the droplet position on the sensor membrane, size variations and evaporation. The variation is far too great (~mV) compared to the voltage difference between the cell droplet and the water droplet. Because of this, it is impossible to make a comparison between the sample and the reference water droplet, which is needed to exclude the evaporation heat loss from the heat energy created by the cells.

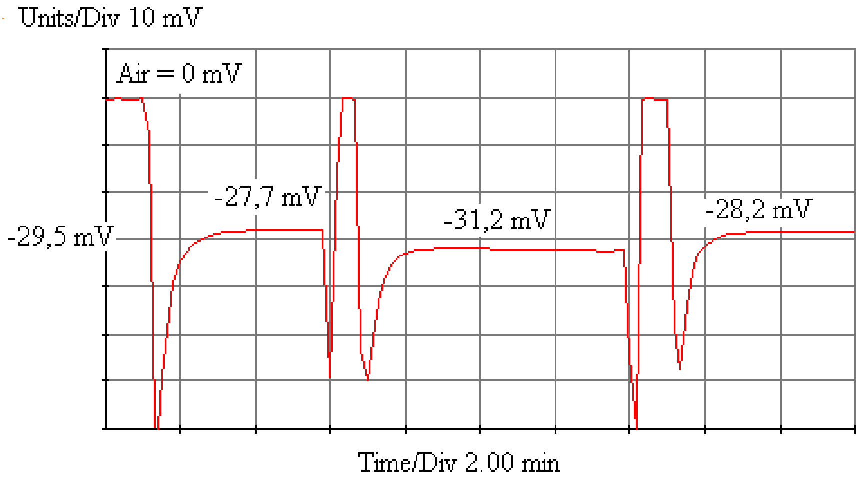

Figure 42. Repetitive evaporation tests with 2 µl water droplets [2].

4.6 Discussion

Xu et al. [124] employed a similar micromachined nanocalorimeter with SiO_2/SiN membrane and Seebeck coefficient of 24 µV/K per junction. Their measured sensitivity was 2.9 V/W, which is lower than the measured sensitivity of the VTT nanocalorimeter. Their approach was to use a droplet injector with 1% reliability in volume delivery and to position the micropipette through a sealed hole in the cover glass. With this setup, they were able to reach a detection limit of 22 nW with ~2% day-to-day reproducibility even with a less sensitive MEMS calorimeter. The measurement reproducibility issue of droplet nanocalorimeters is currently of great interest for chemical reaction enthalpy measurements as well as cell/bioevent characterization, and has been recently addressed in a review [125] which also listed the eight most advanced droplet nanocalorimeters (open and closed chamber) based on power resolution (13 to 300 nW). Thus, although the measurements reported in this thesis indicate reproducibility-related problems with the current open-chamber measurement setup, there is still potential for using this sensor for yeast cell measurements. Unlike the commercially available nanocalorimeter used by Xu et al. [124], the sensor developed by VTT is able to confine a larger amount of thermocouples into a small area of the membrane. This requires that some simple modifications are made to the setup which might help improve reproducibility.

The most disturbing effect besides evaporation in liquid calorimetry is droplet size and position variation, which affects the base level of the output voltage signal in the order of several millivolts. Based on the measurement results, a few improvements have been proposed but have not yet been implemented.

The simplest way to guide the droplet to the same position is to stamp a circular area onto the sensor membrane using a stamp (a tube of known diameter, selected for a specified size of measurement droplet). The stamp is coated with an adhesive and pressed gently onto the membrane leaving a circle which indicates the exact position of the droplet and improves reproducibility. This method does not help in terms of evaporation, however.

Figure 43 shows a new proposed microsystem for yeast cell measurement. A circular polymer tube of small radius is attached to the sensor membrane. This helps to reduce the variance in droplet placement while also minimizing evaporation. The height of the tube can be varied for different sample volumes, and a PDMS (polydimethylsiloxane) cover effectively closes and seals the sample to minimize evaporation.

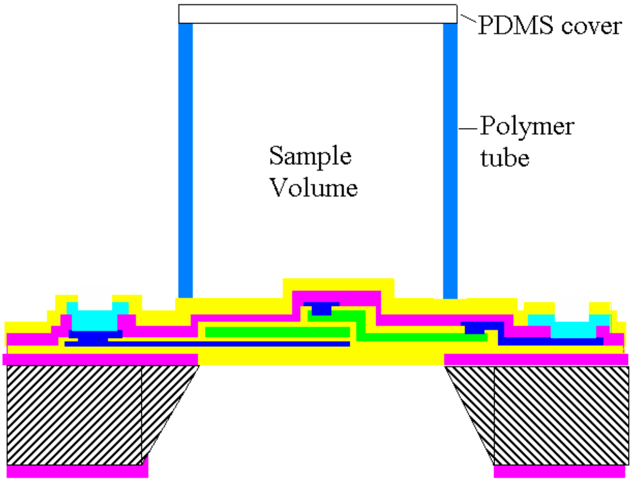

Figure 43. A nanocalorimetric microsystem for yeast cell measurement [2].

Possible problems with this type of set-up include cleaning of the sample chamber and the general durability of the device, as the polymer tube can easily detach and the sensor membrane can break.

4.7 Conclusions

The measurement results presented in this thesis show that the heat produced by a yeast cell population (~$1*10^5$ – $1*10^6$) can be seen in the measured output voltage curve pattern of the nanocalorimetric sensor and in the different levels of the thermopile baseline output voltages. However, to be able to extract the heat loss caused the by evaporation from the heat generated by the cells, parallel reference measurements in a more reproducible measurement set-up are needed. With the current nanocalorimetric sensor this is not possible due to high variance in the sample output voltage base level during each droplet measurement, caused by the sample placement on the membrane and evaporation.

A new microsystem set-up is proposed which could reduce both of these factors and improve the sensitivity and reproducibility of the measurements. Due to limited resources, the experimental work and measurements for this set-up could not be performed but this proposal serves a suggestion for future research. The improved measurement set-up contains a sensor for the sample and an identical sensor for the reference droplet. In this way, evaporation and environmental changes can be taken into account, and the heat produced by the cells can be obtained by comparison with the reference signal. In addition, to minimize evaporation, a microfluidic measurement chamber was designed to be attached to the sensor, as shown in Figure 43. The chamber consists of a plastic ring, which improves the thermal isolation between the hot and cold thermopile junctions, and a PDMS cover to reduce evaporation.

5. Visible light Fabry-Perot interferometer

5.1 Introduction

In this section, a novel microspectrometer for the visible spectral region is realized, integrating a tunable microfabricated Fabry-Perot interferometer for the wavelengths between 430 and 580 nm [6] on a Si photodiode using IC-compatible microfabrication techniques. The Fabry-Perot interferometer is an electrostatically actuated structure consisting of two parallel Bragg mirror structures with imbedded circular aluminium electrodes in the top- and the bottom mirror stack. The passband wavelength of the device is determined by the air gap between the two mirrors. By electrostatically adjusting the distance between the mirrors, the transmission wavelength of the device is tuned. The optical thickness of each layer in the mirror stack structure is λ/4, determined by the refractive index and the physical thickness of the thin film. Each mirror consists of stacks of ALD deposited dielectric multilayers of TiO_2 and Al_2O_3. ALD enables precise deposition of thin pin-hole free layers, which has enabled the development of this type of monolithic sensor structure for the visible spectrum range for the first time [93]. Grating-based microspectrometers for the visible wavelength range are commercially available from Hamamatsu, but their fabrication process is not monolithic, which makes the spectrometer more sensitive to temperature fluctuation related calibration unreliability. Grabarnik et al. have also recently published the fabrication of a visible range microspectrometer based on concave grating [126], but this process is also not monolithic. Besides integration to a Si photodiode, a significant advantage of FPI-type filter is in its application to spectral imaging, which is not possible with grating-based spectrometers.

The present work develops this type of device for spectroscopic measurements further by presenting a fabrication process for monolithic integration of the FPI structure on top of a silicon photodiode. The central wavelength of this chip microspectrometer is $\lambda = 500$ nm. Separate filters for different central wavelengths with increased optical apertures are demonstrated [4] and the use of alternative processing methods is discussed [5]. Miniature imaging spectrometers based on these MEMS FPI filters are presented [8] and their application to biological cell measurements is discussed.

5.2 Background

Optical monitoring of cell cultures offers various advantages. It can be performed continuously on-line, while also being non-invasive (less risk of culture contamination) and non-destructive [127]. Several parameters, analytes or multiple dyes can be detected simultaneously. Nevertheless, most optical characterization tools available today are either very expensive bench-top fluorescence spectrometers or very simple single-wavelength probes, capable of measuring only a single parameter. Commercial optical sensors for biological cell monitoring consist mostly of probes for measuring dissolved O_2, CO_2 and pH (chemiluminescence) and biomass or turbidity (single wavelength NIR absorption) [128]. New MEMS- based solutions can help to reduce the cost of spectrometers and advance spectral process monitoring [129].

Although fluorescence is a very common tool in the monitoring of lab-on-chip devices, the detection equipment is very large in size compared to the dimensions of the microfluidic cell cultures. The microspectrometer chip and the MEMS FPI filter-based miniature imaging spectrometer presented in this thesis are both more easily integrated into or adapted to the small dimensions of microfluidic analysis systems than conventional spectral measurement instruments. The proposed spectral sensors may also add versatility to fluorescence monitoring by allowing fast multiwavelength measurements due to their short tuning response time, in contrast to the time it takes to adjust the filter wheel in common fluorescence microscopes.

5.3 Theory

5.3.1 The Fabry-Perot etalon and Bragg mirror structure

The Fabry-Perot interferometer is an optical resonator consisting of two parallel mirrors (Figure 44). In the case of a Fabry-Perot etalon, the position of the mirrors is fixed, whereas in the interferometer the mirrors can be moved. Light enters the cavity and undergoes multiple reflections. The simplified interference condition for the Fabry-Perot can be expressed as

$$2d\cos\alpha = k + \frac{\varphi_1 + \varphi_2}{2\pi}\lambda \tag{17}$$

where d is the mirror spacing, α is the angle of incidence of light, λ is the wavelength, k is the interference order and φ_1 and φ_2 are the phase shifts of reflection in the structure.

The transmittance function for the FPI can be expressed as

$$T = \frac{1}{1 + F\sin^2\left(\frac{\delta}{2}\right)}, \tag{18}$$

where the phase difference between the reflections is

$$\delta = \left(\frac{2\pi}{\lambda}\right) 2nd\cos\alpha \tag{19}$$

and F is the coefficient of finesse, expressed as a function of reflectance R

$$\mathrm{F} = \frac{4R}{(1-R)^2} \tag{20}$$

Here, it is assumed that reflectance R is dentical on both surfaces ($R_1 = R_2$). If it is also assumed that there is no absorption, reflectance is the complement of the transmittance T:

$$R = 1 - T \tag{21}$$

Ideally, the FPI transmits the resonant wavelengths of the incoming light. Maximum transmission ($T = 1$) occurs when the difference in the optical path length ($2nd\cos\alpha$) is an integer multiple of the wavelength. In tunable FPIs, the passband can be tuned by applying voltage to the electrodes, which modulates the distance of the mirrors.

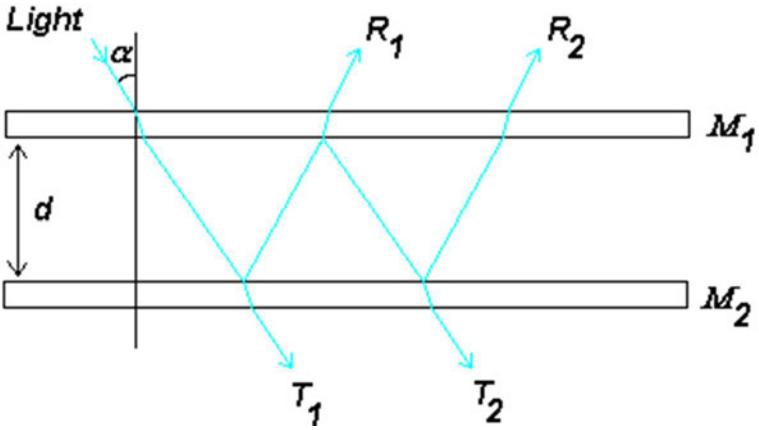

Figure 44. Schematic operating principle of a FPI, where d is the distance between the two mirrors M_1 and M_2. The resonant case corresponds to the constructive interference of the light beams between the mirrors.

A typical FPI transmission spectrum is shown in Figure 45. The transmission maximums appear at different wavelengths, and the distance between the peaks is the free spectral range (FSR). Full width at half maximum (FWHM) is the spectral width of the peak at half of the maximum transmission. The reflection finesse N_F is the ratio of FSR to FWHM. For an ideal FPI with high N_F, the FSR is large and FWHM is very narrow (Figure 46).

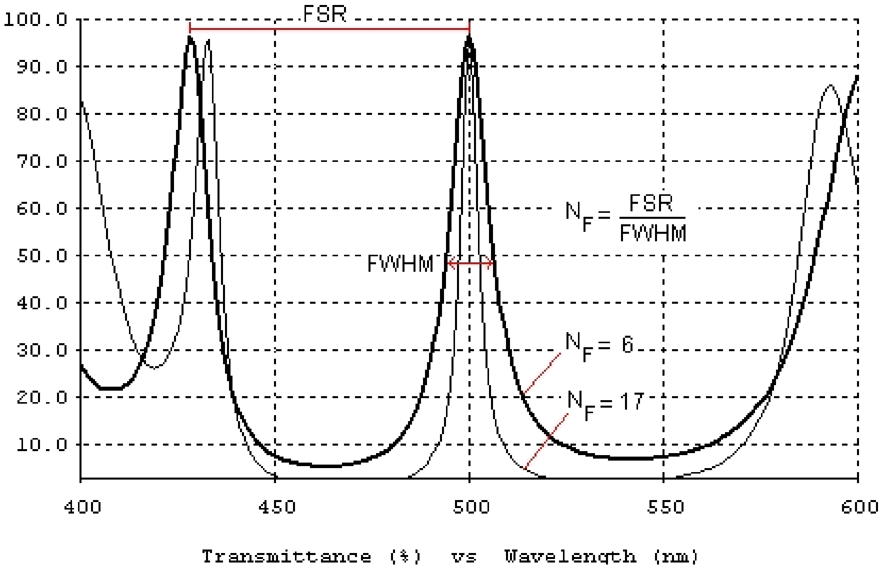

Figure 45. Schematic presentation of the FPI transmission spectrum and reflection finesse (N_F).

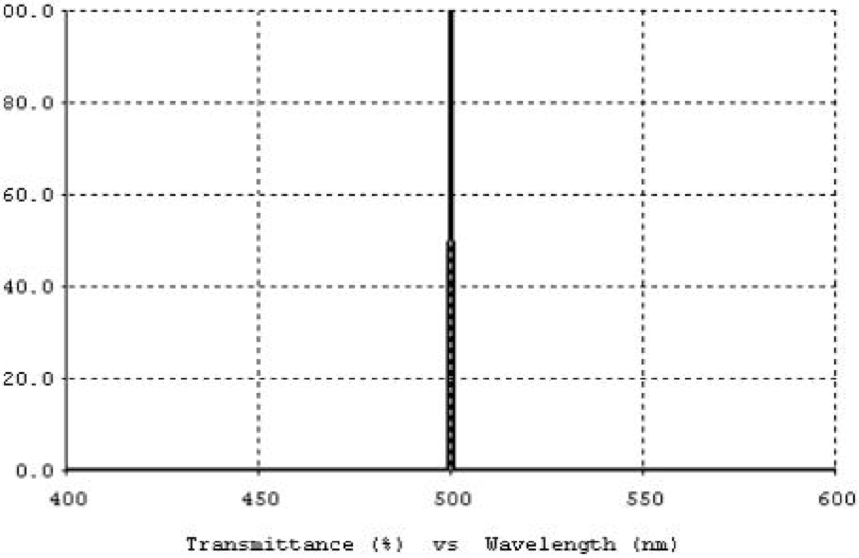

Figure 46. Simulated transmission spectrum of an ideal FPI with high N_F, large FSR and very small FWHM.

In an FPI, the FSR and FWHM can be independently controlled, as the FSR is set by the cavity gap and the FWHM is controlled by the mirror reflectivity. The higher the reflectivity, the sharper the peaks [130]. When using quarter-wave stacks or Bragg reflectors as mirrors in the Fabry-Perot structure (Figure 47), the effective optical path is different from the situation presented in Figure 44 and the theoretical representation of the FPI is more complex. The equations presented here offer a simplification of the system and the more advanced theory is presented elsewhere [131].

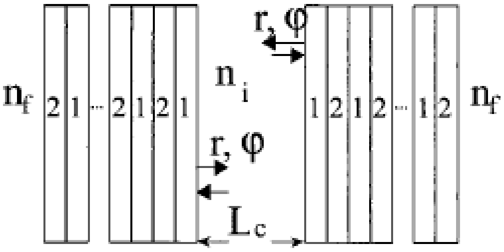

Figure 47. Schematic operating principle of a FP filter consisting of mirror stacks with N quarter-wave layer pairs of alternating refractive indices n_1 and n_2. L_c is the physical cavity length, n_i is the internal refractive index and n_f the final refractive index outside the stack [131].

This structure consists of pairs of alternating dielectric layers with higher and lower refractive index. In this type of structure, the effective optical path length for each layer in resonance is

$$k_m n_j L_j = \frac{\pi}{2}, \tag{22}$$

where in the m^{th} mode of interference, n_j is the refractive index of the thin film layer and L_j is the thickness of the layer. In constructive interference, $k_m = 2\pi/\lambda$ and from this, it follows that

$$n_j L_j = \frac{\lambda}{4}. \tag{23}$$

Thus, the thicknesses of the dielectric layers in the mirror structure are defined by the quarter of the wavelength for which the structure is designed, divided by the refractive index of the dielectric material. The first and the last layer of the structure typically correspond to the high refractive index needed to obtain high reflectivity.

The reflectance R_r of a quarter wavelength stack with a high refractive index material on the outermost layer is given by

$$R_r = \left(\frac{1-Y}{1+Y}\right)^2 , \tag{24}$$

where *Y* is the optical admittance of a quarter wavelength stack with (2P+1) layers:

$$Y = \left(\frac{n_H}{n_L}\right)^{2P} \frac{n_H{}^2}{n_S} . \tag{25}$$

where n_H is high index of refraction, n_L is the low index of refraction and n_s is the refraction index of the substrate. One can see that the reflectance of the Bragg mirror is the better the larger the contrast between the refractive indices of the used materials in the mirror structure. The reflectance can be used to calculate the finesse as shown in Eq. 21.

5.3.2 Capacitive tuning

The tunable Fabry-Perot interferometer is an electrostatic actuator which can be approximated by a simple parallel plate capacitor. The pull-in-voltage, i.e. the voltage at which the electrostatic force between the mirrors in the FPI structure causes the upper tuning mirror to be pulled into the lower mirror and the control of the device is lost, is given by [132]:

$$V_{PI} = \sqrt{\frac{8K_l d_0{}^3}{27\varepsilon_0 A_c}} , \tag{26}$$

where K_l is the linear spring constant, d_0 is the original distance of the air gap, ε_0 is the permittivity of the free space and A_c is the area of the capacitive plates. The pull-in distance is roughly one third of the original gap.

To extend the range of travel to the entire length of the original gap d_0, the gap should be extended to $3d_0$, but as this is not very practical, the required additional gap length $2d_0$ could be replaced by a series capacitor (less than half of the initial capacitance), thus enabling the mirror to travel the entire gap in a stable manner [133]. The series capacitor forms a voltage divider circuit, thus decreasing the fraction of the total imposed voltage [133]:

$$V = \frac{c_1}{c_0 + c_1} V_a , \tag{27}$$

where c_0 is the variable capacitance of the original actuator and c_1 is the series capacitance, V_a is the total applied voltage. In this case, as the movable plate or electrode goes beyond one third of the gap, the capacitance increases rapidly providing the necessary negative feedback to maintain stability.

In the case of an FPI, there is no need to achieve a stable tuning range of the entire gap, as this would result in bending of the Bragg mirror structure and poor optical filter quality. Thus, the series capacitance is added to the system to ensure stable tuning and a linear spring constant. A sufficient series capacitance value is achieved when the series capacitance is equal to the capacitance of the movable air gap. This means that the capacitance is larger than that required for tuning the entire gap length but, on the other hand, the required voltages remain low, which is of practical importance.

5.3.3 PIN photodiode operating principle

A PIN photodiode is a photodetector with an intrinsic region between its highly doped p+ and n+ regions. In the intrinsic or undoped region, the number of excited electrons and holes is equal. In operation, in the so-called high-level injection mode, this intrinsic region is flooded with the charge carriers from the n- and p-type regions. The depletion region which exists in the intrinsic region of the PIN photodiode is larger than the depletion region of an ordinary PN-diode. This means that the space in which photons can create electron-hole pairs (EHPs) is larger, and results in an increased absorption region and decreased depletion capacitance.

When used as photodetectors, PIN diodes are under reverse bias (n-type region is negative with respect to p-type region). Under reverse bias, the diode is not conductive, but as a photon enters the intrinsic region and creates an EHP, i.e. a free carrier. The reverse bias field thus moves the carrier out of the intrinsic region and a current is created. EHPs are generated by photons with energies greater than the band-gap energy (E_g) of the semiconductor material. The band gap also sets the cut-off wavelength (in nm) for the photodetector, given by

$$\lambda_c = \frac{1.24}{E_g(eV)}. \tag{28}$$

5.3.4 Atomic layer deposition (ALD)

Chemical vapour deposition (CVD) is a common thin film deposition technique in microfabrication. It can be applied in different process forms, such as low-pressure (LPCVD) and plasma enhanced (PECVD) chemical vapour deposition. ALD belongs to the category of CVD processes, but unlike normal CVD reactions, ALD reactions are self-terminating. A typical ALD process consists of cycles of reactants (gaseous chemicals such as $AlMe_3$ or $TiCl_4$ and H_2O) separated by an inert gas purge (N_2). Each reaction cycle adds a small amount of material to the surface, depending on the reactants and deposition temperature, and the process is continued until the desired deposition thickness is achieved [134].

Due to the surface-controlled nature of ALD, the achieved thin films are extremely conformal. The excellent thickness control and uniformity makes ALD thin films very desirable for MOEMS applications, where optical thin film thickness is very desirable. Due to the cyclic process, ALD deposition is slow, on the order of a nanometre per minute. However, ALD processes can be scaled for large substrate sizes and batch processing, making them suitable for MEMS production.

5.4 FPI and microspectrometer design considerations

5.4.1 Optical design issues

There are a few important considerations to be made when designing a microspectrometer based on a tunable FPI. The finesse or spectral resolution of the FPI is limited by the reflectivity of the mirror structure. High resolution requires high reflectance, and high transmission requires low absorption. In a Bragg mirror structure, this means that suitable materials must have 1) large enough contrast between the high and low refraction indices, and 2) low absorption in the measured spectral range. In practice, the range of candidate materials is limited due to the required IC compatibility in the deposition process and the required thin film properties (good uniformity over the entire wafer to ensure good yield, tension and stress properties suitable for forming stable and robust multi-layer stack structures). If the difference between the used high- and low index materials is small and the resulting reflectivity is too low, this can be compensated by increasing the number of layer pairs. This may, however, lead to absorptive losses as well as increased internal stresses of the multilayer stack, possibly resulting in breakage of the mirror structures and low processing yield of the devices.

Aperture size influences spectrometer Signal-to-Noise-Ratio (SNR), especially in imaging optics [7]. The SNR can be improved by collecting more light to the image sensor, which translates into developing as large aperture FPIs as it is possible. The key part in the MEMS structure which sets the limit to the optical aperture size is the diameter of the released upper Bragg mirror membrane.

In the past, metal reflectors have been used as the refractive mirrors in visible spectral region Fabry-Perot etalons, but their transmission is very low [88]. The review article by R. Wolffenbuttel also states that the fabrication of dielectric multilayer stacks of alternating materials is marginally compatible with microelectronic processes. This, however, is no longer true; with the development of atomic layer deposition (ALD) process it is now possible to fabricate high-quality film stacks of alternating materials with a film thickness control of a few nm and with excellent uniformity. ALD deposition can be done at different temperatures (110 °C and 300 °C being the process temperatures at VTT). The low-temperature processing makes it possible to integrate the FPI structure on the photodiode, as the earlier fabrication steps in the photodiode process limit the temperature for later process steps.

As the deposition temperature of the ALD process has an effect on the resulting thin film properties, in order to develop accurate mirror structures the optical properties of the ALD materials used in the present study were measured in the UV-visible range [3]. The refractive indices for Al_2O_3 and TiO_2 measured in the UV-visible spectral range are presented in Figure 48 and Figure 49. From these measurements it can be seen that the extinction coefficient remains low for both materials in the visible range, but for TiO_2 the extinction coefficient rises notably in the UV spectral range below 350 nm. This indicates that the absorption properties of TiO_2 are not favourable for making optical filters for the UV region.

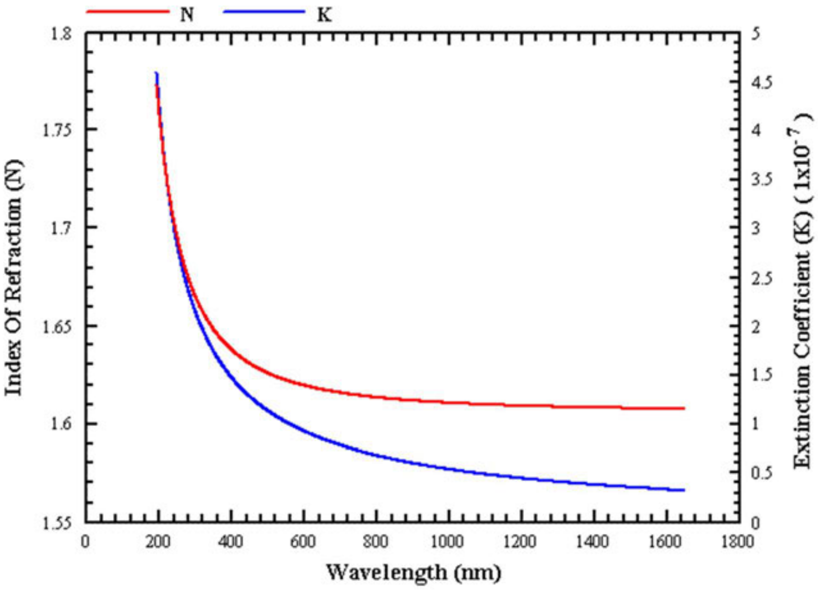

Figure 48. Al_2O_3 index of refraction vs. wavelength in the UV-visible spectral range [5].

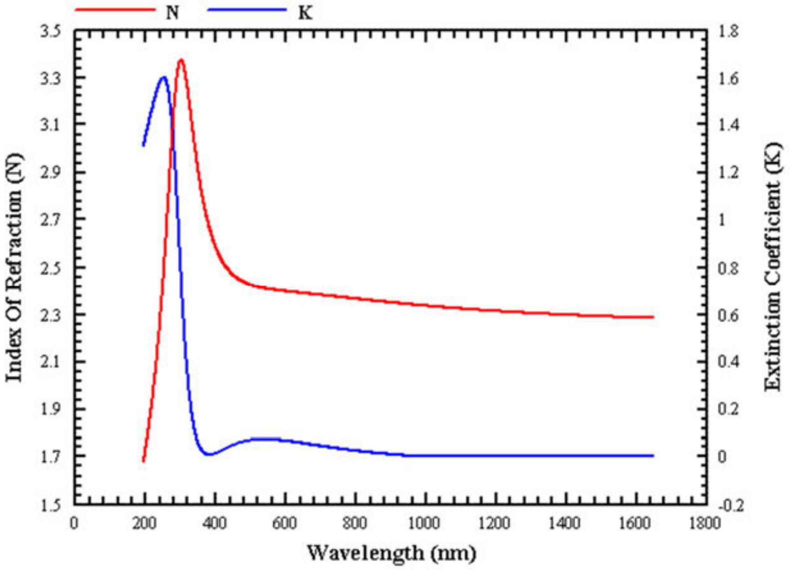

Figure 49. TiO_2 index of refraction vs. wavelength in the UV-visible spectral range [5].

As the properties of ALD materials also depend on their deposition temperature, comparative measurements were done to assess whether there was a difference in the refractive indices of materials deposited at 110 °C or 300 °C. The results are presented in Figure 50 and Figure 51. It can be seen that there is some difference in the refractive index values for low and higher temperature materials, which is good to consider when designing the mirror stack structure.

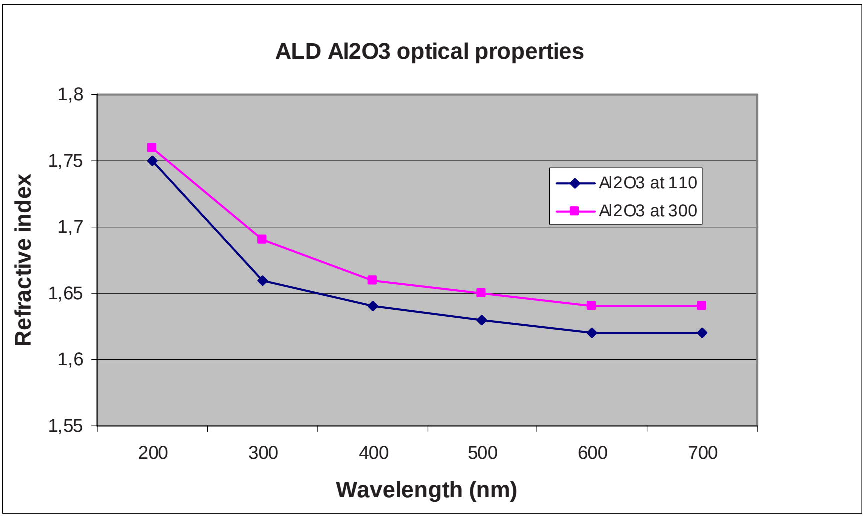

Figure 50. Wavelength dependence of the refractive index of Al_2O_3 thin films grown at 110 °C and 300 °C [3].

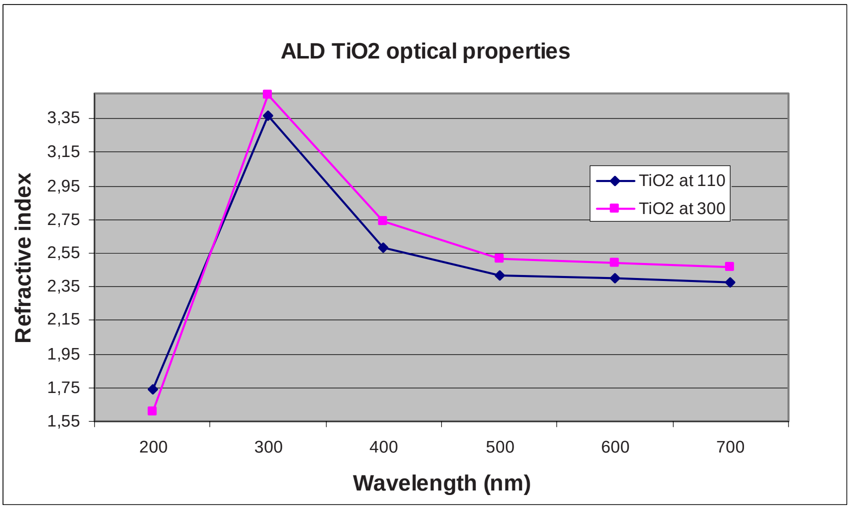

Figure 51. Wavelength dependence of the refractive index of TiO_2 thin films grown at 110 °C and 300 °C [3].

Based on the optical measurements of the ALD films, it can be concluded that the transmission properties of the ALD thin films are excellent in the visible range and the difference in the refractive indices is large enough to realize a 5-layer Bragg mirror with good reflectivity. The simulation results for the optical performance of the tunable FPIs for λ = 500 nm and λ = 670 nm are presented in Figure 52 and Figure 53. The simulated FWHM for the λ = 500 nm FPI is 5 nm and the reflection finesse N_F is 13,4. For the λ = 670 nm FPI, the simulated FWHM is 5 nm and the reflection finesse N_F is 9,5.

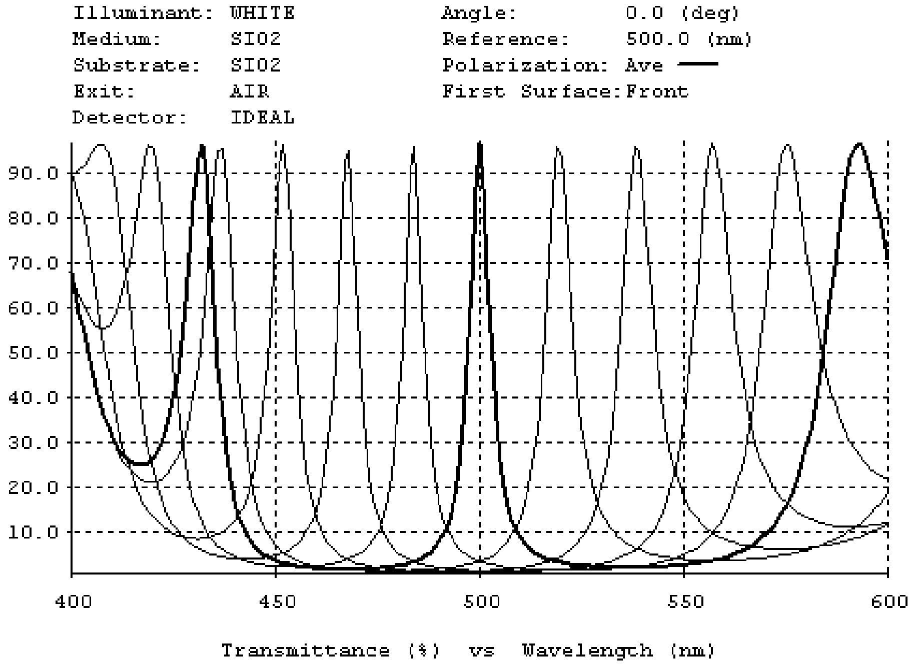

Figure 52. Performance of the tunable FPI for λ = 500 nm with two 5-layer Bragg mirrors of Al_2O_3 and TiO_2 when the air gap is changed in 50 nm steps from 1250 nm (rest gap) to 1050 nm.

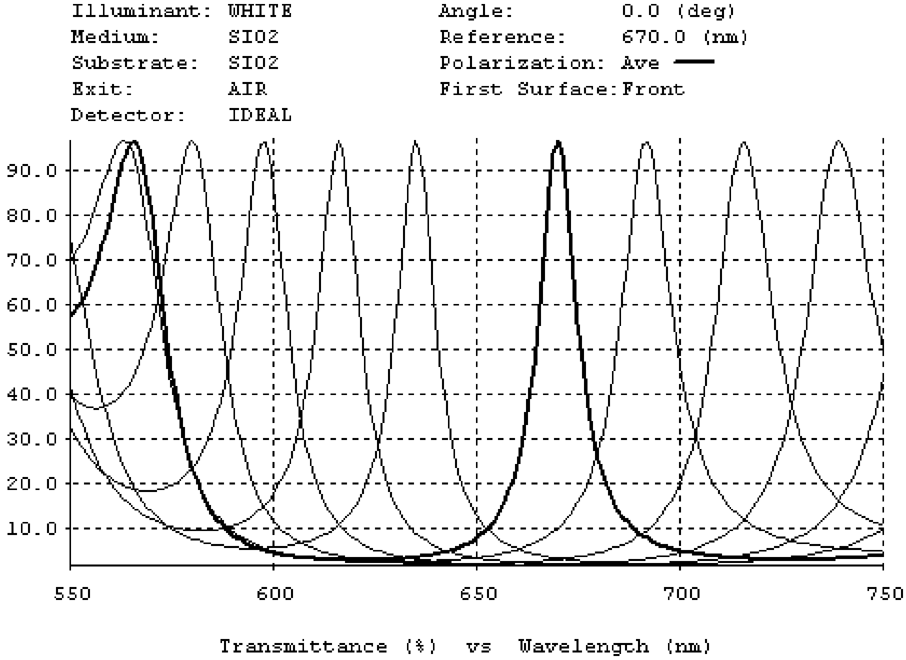

Figure 53. Performance of the tunable FPI for λ = 670 nm with two 5-layer Bragg mirrors of Al_2O_3 and TiO_2 when the air gap is changed in steps from 1340 nm to 1100 nm.

5.4.2 Layout design

The mask layout for the integrated FPI device is presented in Figure 54. In the lithography reticle there are nine variations of the device, with an aperture size ranging from 1 mm to 2 mm, an upper mirror diameter ranging from 2.8 mm to 4.5 mm and a released area diameter ranging from 2.2 mm to 3.4 mm. The dimension variations are listed in Table 4. A total of 13 mask layers are needed to complete the fabrication.

Table 4. Structure dimensions related to FPI gap tunability. R_a is the diameter of optical aperture, R_r is the diameter of released area, R_0 is the outer electrode diameter, C_s / C_0 is the ratio of series capacitance to original control capacitance, d_t is the travel distance and TR is the stable tuning range as percent of the original gap distance (1.3 µm).

R_a (µm)	1	1	1	1.5	1.5	1.5	2	2	2
R_r (µm)	2.2	2.2	2.2	3	3	3	3.4	3.4	3.4
R_0 (µm)	2.8	3.4	3.8	3.8	4.2	4.5	4.0	4.2	4.5
C_s/C_0	2.34	5.25	7.5	2.42	3.84	5	1.76	2.41	3.45
d_t (nm)	620	520	490	610	550	520	680	610	560
TR (%)	47.6	39.7	37.8	47.1	42.0	40	52.3	47.1	43

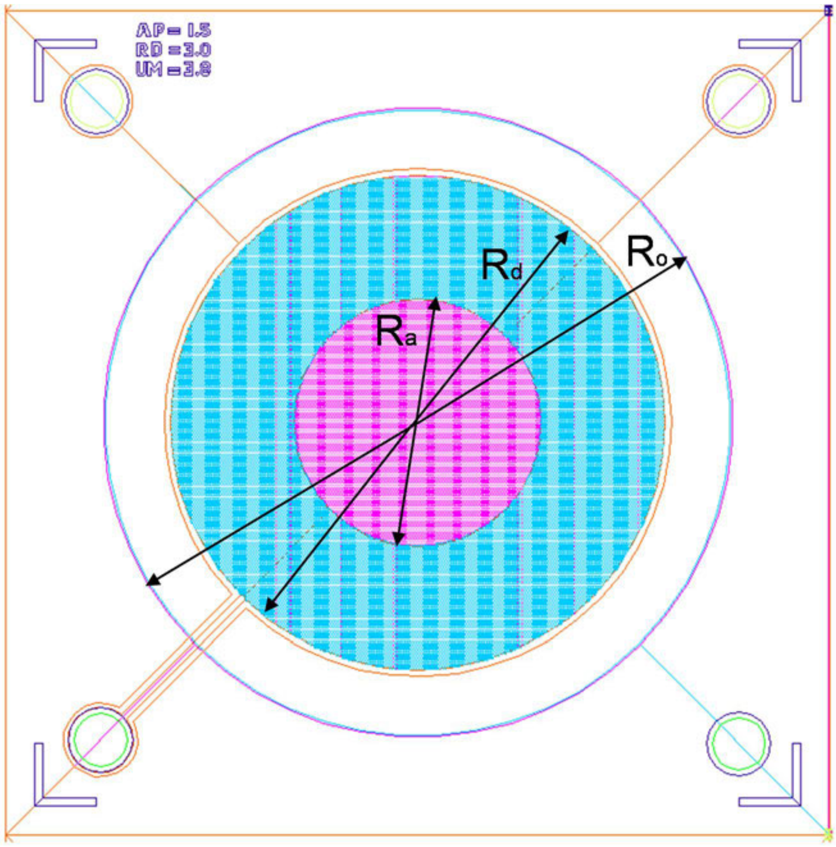

Figure 54. Mask layout for the integrated FPI on photodiode, with an aperture of 1.5 mm, upper mirror diameter of 3.8 mm and released area diameter of 3.0 mm.

5.5 Fabrication and characterization of the FPI structures

In this section, the fabrication of the monolithically integrated microspectrometer is presented, along with the fabrication of a separate FPI optical filter for λ = 670 nm, shown in Figure 55. The fabrication of the components was carried out in the VTT cleanroom. The process developed for a stand-alone FPI for λ = 500 nm [93] has served as the background for these new processes.

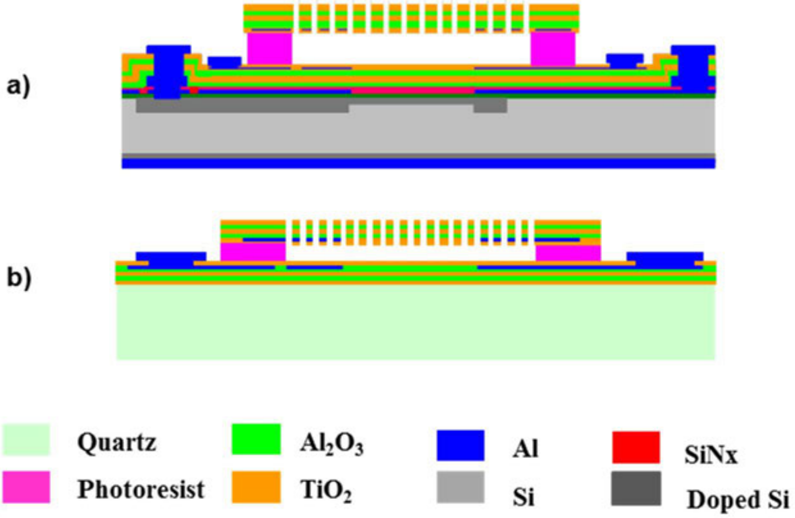

Figure 55. Cross sections of a) a finalized monolithically integrated FPI on a Si photodiode and b) a finalized FPI for λ = 670 nm on a quartz (fused silica) wafer.

5.5.1 Fabrication process of the integrated FPI on a photodiode

The integration of a visible wavelength range FPI structure on PIN photodiode advances the miniaturization of spectrometers into chip-size devices while offering a robust mass-producible construction based on a truly monolithical fabrication process. The process flow is summarized in Figure 56. Float zone (FZ) Silicon wafers were used as substrates (n-type, resistivity > 5000 ς-cm). Wafers were oxidized at T = 1000 °C for 135 min, yielding 82 nm of SiO_2, and deep boron ion implantation was conducted around the photodiode circular aperture region as well as electrical contact arm using ion implantation dosage of $1.0 \cdot 10^{15}$ cm^{-2}. (Figure 56 a). The backside was implanted with phosphorus at a dose of $2.0 \cdot 10^{15}$ cm^{-2} (electrical contact) and shallow boron doping was implanted to the front side optical aperture region (Figure 56 b), after which a drive-in procedure to activate the dopants was performed in a diffusion furnace at T = 1000 ºC for 60 min. The backside oxide was removed and thick aluminum film was sputtered for making

electrical contact. Frontside oxide was patterned (contact opening) and thin Al film was sputtered (Figure 56 c). Frontside Al layer was patterned. This aluminium layer serves two important purposes; it inhibits light from entering the photodiode active areas from other parts except the optical aperture, and the electrical grounding of the layer shields the photodiode from the AC voltage used to control the FPI structure. Insulating SiN_x layer was deposited in PECVD at T = 300 ºC. This film also serves as the bottom layer in the optical film stack (Figure 56 d).
Next, the SiN_x was patterned (contact opening) and thick Al layer was sputtered and patterned for photodiode electrical contact and shielding Al layer electrical grounding. The aluminium was then sintered T = 425 ºC for 15 min. At this point, the photodiode was ready and a few wafers were taken out of the process for electrical characterization of the photodiode functionality (Figure 56 e). ALD Al_2O_3 (75nm) and TiO_2 (50 nm) multilayer stack was deposited at T = 110 °C (Figure 56 f). Thin Al layer was sputtered and patterned, forming the lower control electrodes for the FPI structure. The remaining 25 nm of the top ALD TiO_2 optical layer was deposited, capping the electrodes (Figure 56 g). Contact openings were patterned and etched in plasma through the ALD multilayer stack in two separate lithographic processes for both the photodiode and the FPI (Figure 56 h). Thick Al layer was sputtered and patterned for contact pads. The multilayer on the backside of the wafer protects the Al contact for the photodiode (Figure 56 i).

The sacrificial photoresist was spinned on, patterned and cured with deep UV exposure and baking, resulting in thickness of ~ 1350 nm which determines the rest gap wavelength (order) of the FPI. Patterning of the sacrificial layer increases the stability of the upper mirror structure, reducing the risk of upper mirror breakage. Part of the first optical layer in the upper mirror was grown (ALD TiO_2) and thin Al layer was sputtered (Figure 56 j). The Al layer was patterned (plasma etch process) to form the upper mirror electrode and the rest of the upper mirror ALD Al_2O_3 /TiO_2 multilayer stack was deposited (Figure 56 k). The upper mirror was patterned (lithography and plasma etching) to form small holes through which the sacrificial photoresist can be etched (Figure 56 l). The wafers were then diced and individual chips were release etched in a standard photoresist stripper with O_2 plasma (Figure 56 m), lowering the lowering the plasma voltage to maintain the temperature below 150 ºC as heating can cause cracking of the ALD layers due to the higher thermal expansion coefficient of the polymer.

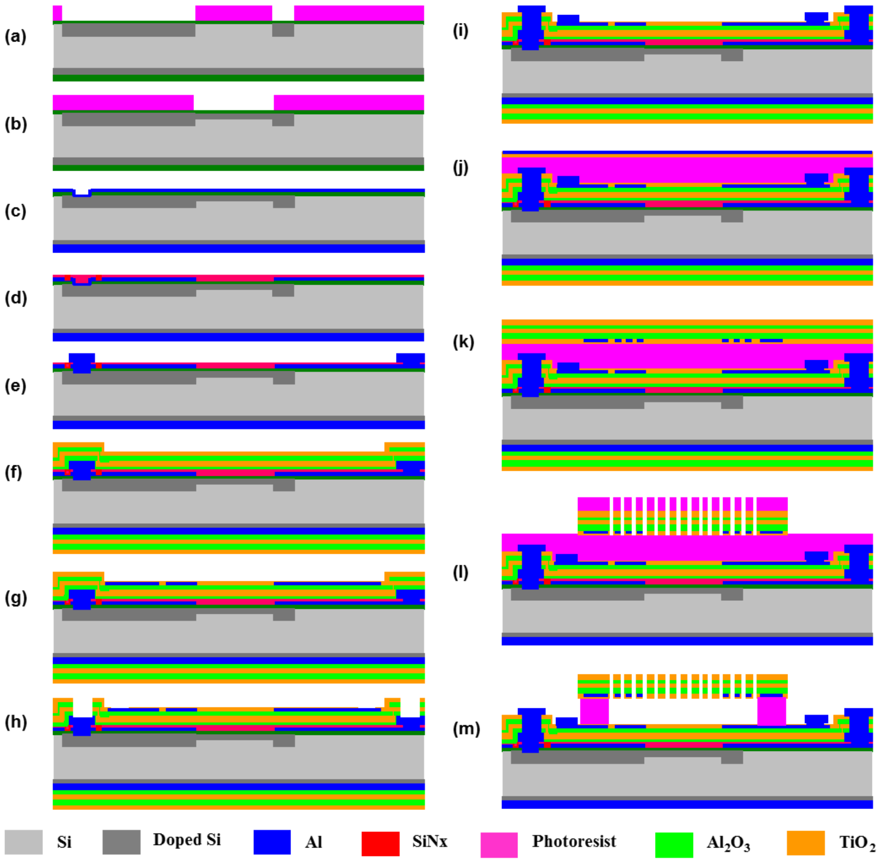

Figure 56. Process flow to fabricate monolithically integrated FPI on photodiode. In a) and b) the active areas of the photodiode on the front- and backside of the wafer are doped, c) backside Al is sputtered as well as frontside thin Al, d) Al patterning and nitride deposition, e) Al contacts, f) ALD deposition of the lower mirror structure, g) lower Al electrode sputtering and patterning and ALD TiO2 capping h) contact hole etching in plasma, i) Al contact sputtering and patterning, j) sacrificial photoresist deposition, ALD TiO2 and Al sputtering k) upper Al electrode patterning and ALD deposition of the rest of the upper mirror structure, l) Upper mirror patterning, m) sacrificial photoresist etching and release of the membrane.

A photograph of a released monolithic FPI spectrometer is shown in Figure 57. A close-up of the mirror membrane prior to release is shown in Figure 58, and Figure 59 shows the membrane after oxygen plasma release. A microscope image of a photodiode which has been processed under the FPI structure is shown in Figure 60.

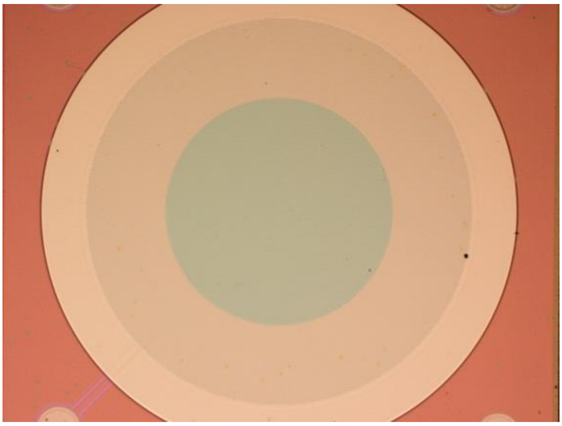

Figure 57. Microscope image of a released monolithic FPI spectrometer. The optical aperture is clear and the film stacks are intact with no sign of internal tension or film cracks [6].

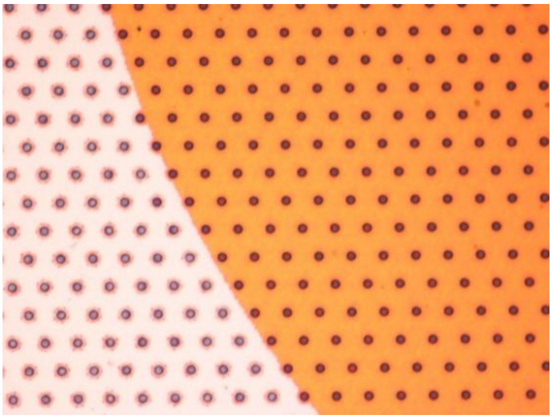

Figure 58. The membrane before release in oxygen plasma, showing the optical aperture area and the metal electrode. Red photoresist is visible in the open etch holes.

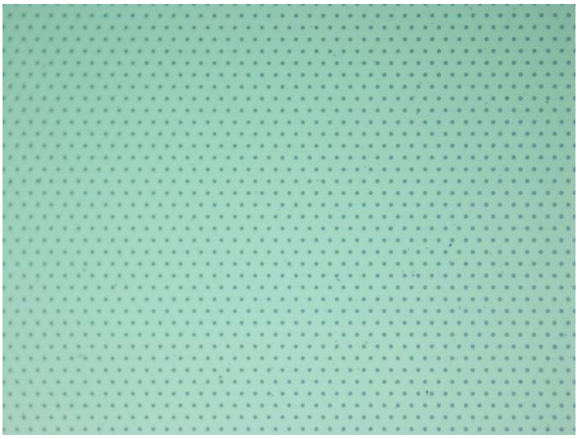

Figure 59. A released membrane of the MEMS FPI at the centre of the optical aperture. After release, the aperture membrane is blue-green in colour.

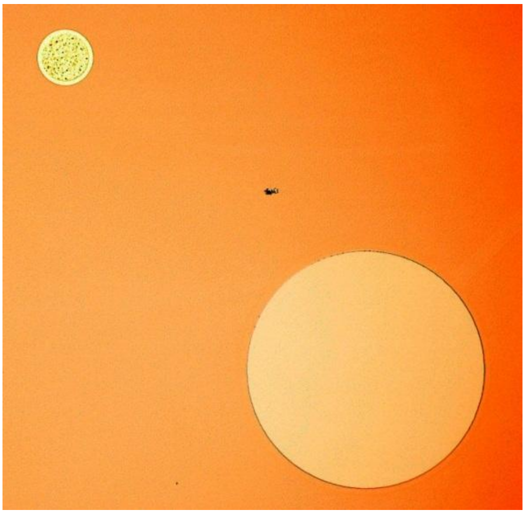

Figure 60. Microscope image of the photodiode structure.

The above process developed by this study thus demonstrates the fabrication of the first monolithically integrated microspectrometer chip for the visible wavelengths (measured device response shown in Figure 61). With good process yield and the mass-production capability of MEMS processing, these low-cost spectrometer chips might be used as a part of microfluidic cell sorters or growth platforms to enable miniaturized spectral point sensing.

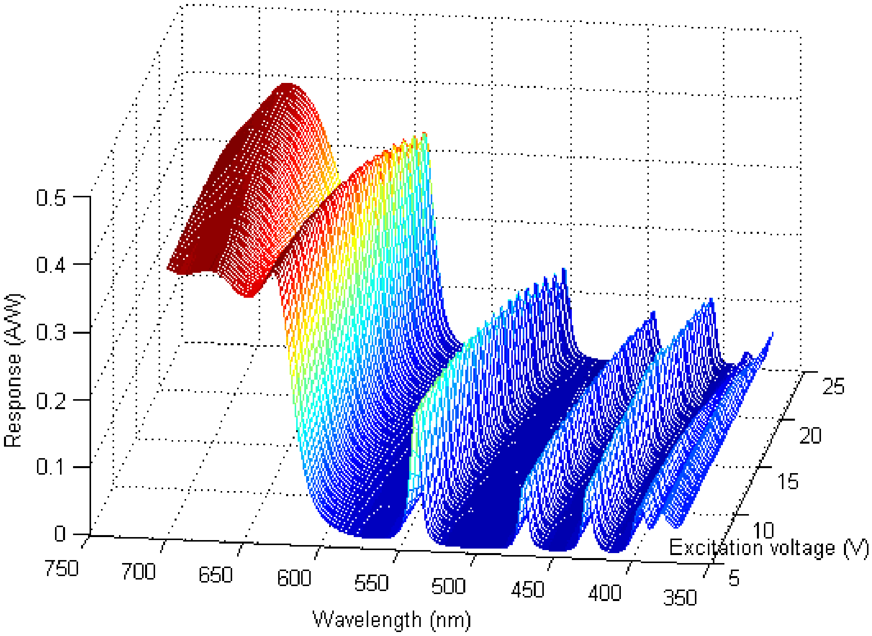

Figure 61. Measured performance of the integrated FPI for λ = 500 nm [6].

5.5.2 Fabrication process for separate FPIs

The fabrication of separate FPI filters offers the opportunity to use different detectors with optical filtering. In case of FPIs this means the possibility to perform spectral imaging [7], which is another important feature that cannot be achieved with visible light grating based spectrometers. Although there are many similarities in the processing of an FPI and the monolithic devices already covered above, there are certain differences that arise from using a quartz substrate. In process experiments it has been noticed that the yield from amorphous quartz substrates can be extremely poor compared to that of silicon substrates. The tensioned ALD layer stacks behave differently on amorphous quartz, which has a different thermal expansion coefficient as well as mechanical properties than silicon. On the other hand, the purpose is to develop a process that allows the fabrication of as large aperture FPI components as possible, and the following fabrication process aims at improving the previously developed 1 mm aperture FPIs by extending the optical aperture to 2 mm and allowing the use of these filters in hand-held imaging spectrometers. These FPI filters have now been realized for various wavelengths covering the visible wavelengths between 350 nm and 750 nm. The presented device is intended for a central wavelength of 670 nm, as such devices are more challenging to fabricate due to the increasing upper mirror stack thickness.

The process flow is shown in Figure 62. First, aluminium was sputtered on both sides of the amorphous quartz (fused silica) substrates. The alignment marks were etched in two separate plasma processes, first in a metal etcher and then an oxide etcher (Figure 62 a). The back side was then covered with protective photo resist and the front surface was cleaned in aluminium wet etch. The ALD stack was deposited with 72 nm of TiO_2, 101 nm of Al_2O_3, 72 nm TiO_2, 101nm of Al_2O_3 and 47 nm of TiO_2, after which the thin Al coating for the lower electrode was sputtered and patterned in wet etch (Figure 62 b). The remaining part of the topmost TiO_2 mirror layer (25 nm) was deposited to cover the electrodes and contact hole openings were etched. A thick aluminium film was sputtered and patterned to form the contact pads for the FPI AC voltage input (lower electrode) and the surrounding grounding electrode (light shield), shown in Figure 62 (c).

After formation of the metal contacts, a sacrificial polymer layer (~ 1350 nm) was spun on. After spinning and curing of the polyimide, the encapsulating TiO_2 film was grown in ALD (Figure 62 d). The upper mirror electrodes were patterned into the sputtered thin aluminium (Figure 62 e) and the rest of the upper mirror ALD stack was and patterned similarly as described for the monolithic FPI spectrometer (Figure 62 f). The back side was etched clear in the plasma process. At this point, an anti-reflective MgF_2 layer can be deposited on the back side to improve FPI functionality, if found necessary. The wafer was then diced into chips and the individual FPIs released in O_2 plasma.

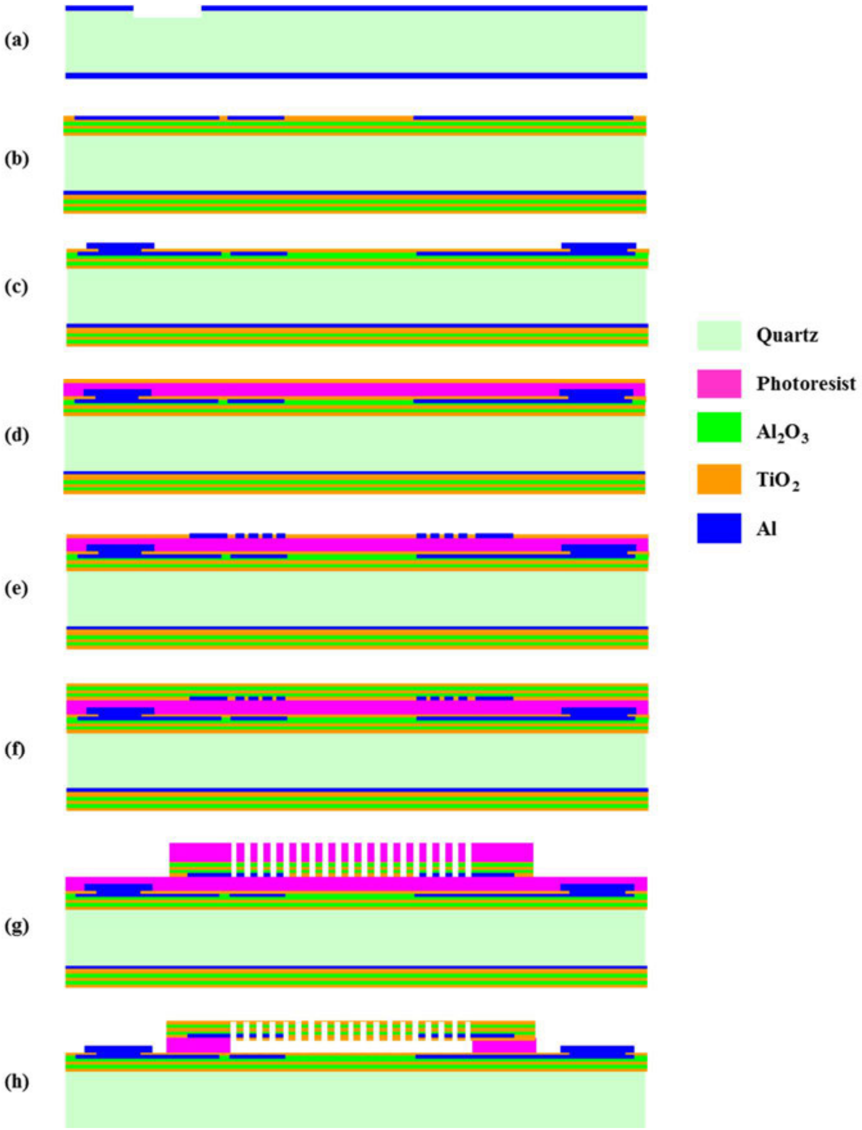

Figure 62. Process flow to fabricate tunable MEMS FPI filters. a) Etching of alignment marks, b) ALD deposition of the lower mirror structure and lower Al electrode sputtering and patterning and ALD TiO_2 capping c) contact hole etching in plasma, Al contact sputtering and patterning, d) sacrificial photoresist deposition and ALD TiO_2 deposition e) Al sputtering and upper electrode patterning, f) ALD deposition of the rest of the upper mirror structure, g) Upper mirror patterning, h) backside cleaning etch, dicing and sacrificial photoresist etching and release of the membrane.

Processing of the monolithic FPI structure on the photodiode was done solely at low temperature for the FPI part, but in some applications also higher temperature processing may be favourable. The optical properties of ALD deposited at T = 300 ºC are slightly different from films deposited at T = 110 ºC (Figure 50 and Figure 51), although the electrical properties also differ [134]. As the TiO_2 becomes much more conductive, effective insulation of the electrodes must be considered and alternative materials used in the optical thin films encapsulating the electrodes (the first and last TiO_2 films of the lower and upper Bragg mirror stack). That said, it is favourable to be able to process the FPI structure at higher temperatures, as that allows for a wider selection of materials to be used, for example, as hybrid stacks of ALD materials and conventional PECVD materials.

However, this higher temperature processing requires other sacrificial layer materials than the photoresist used in the FPI structure of the monolithic process. Thus, a commercial polyimide (PI2610 by HD MicroSystems with VM652 primer) with a low coefficient of thermal expansion (CTE) was also tested for a $\lambda = 670$ nm FPI structure [5]. This polyimide cannot be patterned by UV exposure such as conventional photoresists, so patterning of the sacrificial layer was not performed. In terms of upper mirror stability this proved not to be a problem, because the lower CTE also ensures less stress on the film stack when processed at different temperatures. In the case of ALD stacks deposited at T = 300 ºC there is no temperature limit and the polyimide is as easy to remove as the photoresist.

Figure 63. Completed and released MEMS FPI chips for $\lambda = 670$ nm.

5.5.3 Characterization

Both the monolithic FPI spectrometer and the separate FPI filters were characterized for their performance. The test setup platform for the monolithic FPI spectrometer is shown in Figure 64. A more detailed description of the measurement setup and methods can be found in Ref. [6].

The measured wavelength response of the monolithic FPI spectrometer for the central wavelength of λ = 500 nm is shown in Figure 61 and Figure 65. As the AC excitation voltage is swept between 0 and 25 V, the transmission peak shifts accordingly. The full width at half maximum (FWHM) is ~5 nm and the free spectral range (FSR) between the 5th order transmission peaks is ~70 nm (shown as a blue line in Figure 65). From these measurements it can be seen that the usable spectral measurement range of the spectrometer is between 450–550 nm. Outside this range, the FWHM of the peaks widens due to bending of the mirror and the transmission increases. The performance and IV-characteristics of the photodiode are shown in Figure 66 and Figure 67. Devices with 1 mm and 2 mm optical apertures are compared in terms of light intensity and dark current (illuminated vs. dark measurement).

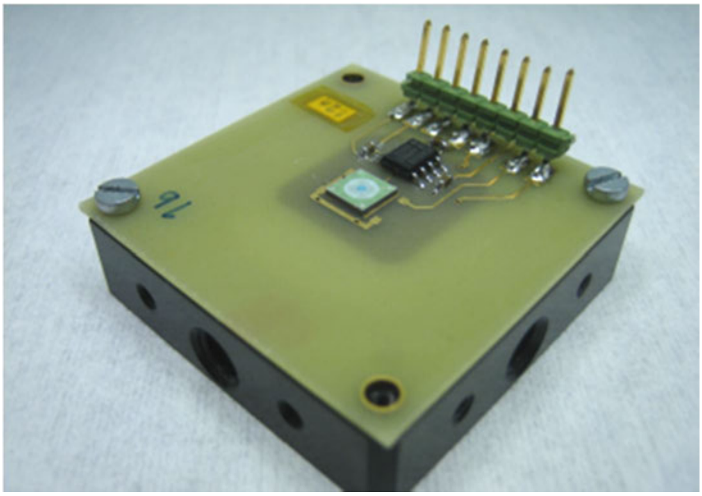

Figure 64. Test setup by Uula Kantojärvi for optical characterization of monolithic microspectrometers. The measurement platform is connected to the rest of the setup described in [6].

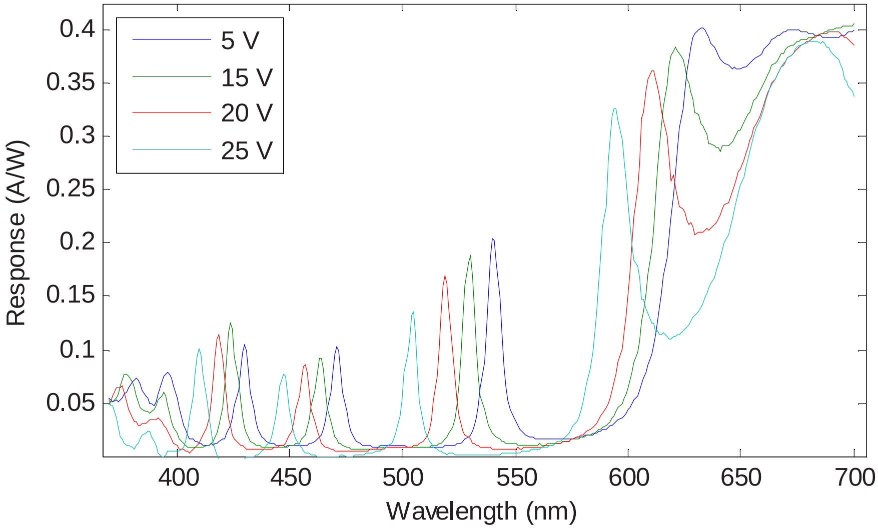

Figure 65. Measured spectral response of the integrated FPI for λ = 500 nm [6].

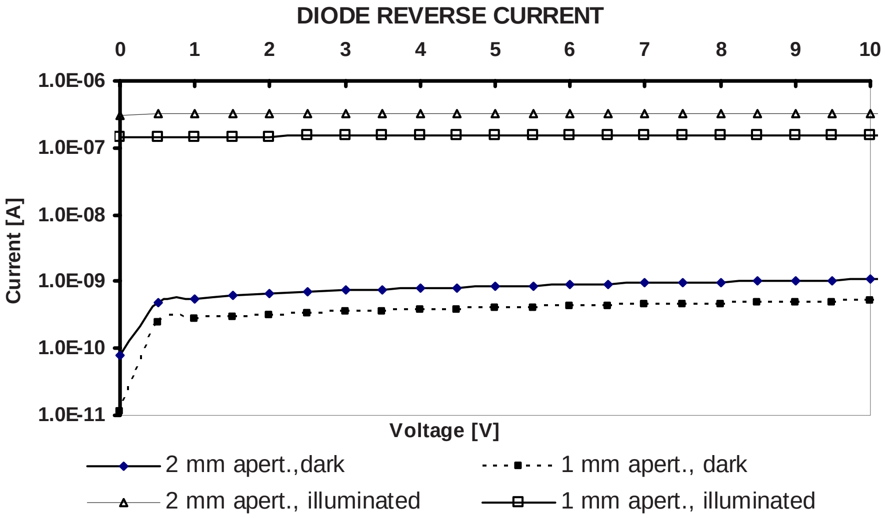

Figure 66. Reverse current measurements of the photodiode [6].

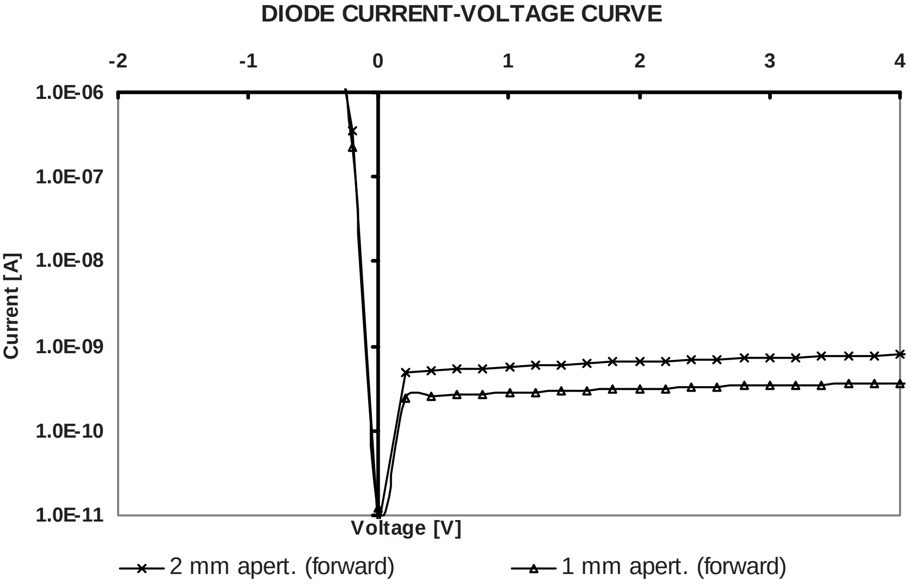

Figure 67. IV-characteristics of the photodiode [6].

The optical performance of the separate FPI for λ = 670 nm is shown in Figure 68. The maximum transmission is 75.5% at the central wavelength (0 V) and the FWHM is 5–7 nm. The rejection ratio (the passband transmission of the peak vs. the transmission at the stopband between the peaks) is ~$1.5 * 10^{-2}$. These characteristics are very similar to the other 2mm aperture ALD FPIs that have been fabricated for wavelengths of λ = 420 nm and λ = 500 nm [4]. The ALD stack membrane is highly tensioned, yielding a flat optical aperture. Any bending of the membrane leads to worse performance, as the FWHM increases and the transmission drops.

The obtained transmission peak widths of the monolithic FPI on photodiode as well as the separate FPI filter for λ = 670 nm are much narrower than the FWHMs typically reported for IR-range FPIs [87–90] and for the reported visible range FPI [91] (typically above 20 nm). The FWHMs reported with grating-based spectrometers can be very narrow (0.9 nm) [126], but the MEMS fabrication process is not monolithic (potential calibration offset by temperature) and cannot be used for imaging.

The major benefit of the separate FPI filters compared to the monolithic FPI spectrometer is the wide range of choice of detector to be used in conjunction with the FPI. Most importantly, this enables the use of imaging detectors, leading to the development of miniature hand-held spectrometers. This will be discussed in the next section.

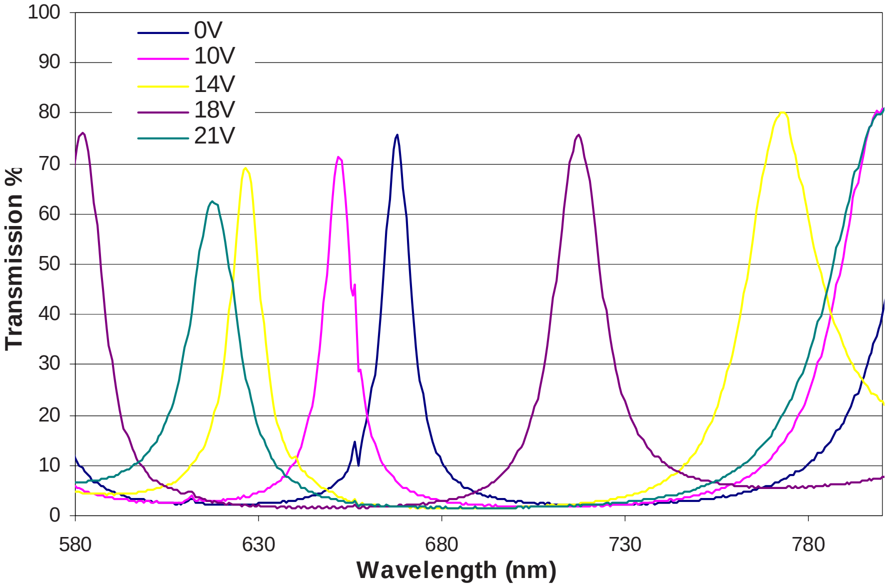

Figure 68. Measured performance of the separate FPI filter for λ = 670 nm (by A. Akujärvi).

5.6 MEMS FPI-based miniature spectrometers

The majority of MEMS-based microspectrometers developed to date are capable of performing measurements in the IR range. Grating-based spectrometers developed for the visible range, on the other hand, are not capable of spectral imaging. The movable 2 mm diameter mirror structure is highly suited for this purpose. Thus, combining a λ = 500 nm FPI with a CMOS imaging detector made it possible to realize the hand-held miniature imaging spectrometer shown in Figure 69. This spectral imager measures light between 430–570 nm, which is the operating range of one FPI chip [8]. Figure 70 shows the inside of the spectrometer, with several flashing LEDs that illuminate the measured object as well as the packaged FPI unit with moving aperture.

A pen-size spectrometer utilizing a MEMS FPI for λ = 500 nm has also been demonstrated. The device combines the FPI with a RGB photodetector, thus enabling single-point measurements (Figure 71).

Figure 69. MEMS FPI (λ = 500 nm) miniature imaging spectrometer [4].

Figure 70. Inside of the imaging spectrometer showing the LEDs that illuminate the object as well as the packaged MEMS FPI aperture in the middle.

Figure 71. Pen-size spectrometer with λ = 500 nm MEMS FPI for single-point spectral measurements [4].

5.6.1 Biological applications for MEMS FPI miniature spectrometers

The operating spectral range of MEMS FPI miniature spectrometers is ideal for biological measurement purposes. Most of the previously discussed commonly used fluorescent dyes operate in the visible light spectrum, making it possible to apply these spectral sensors in bioprocess monitoring or diagnostics. Colorimetric measurements are also widely used in enzyme activity analysis.

One interesting example of such an application is fluorescence monitoring of yeast cells. Fluorescence measurements in yeast cells have been used to detect various phenomena; Fehr et al. [136] used enhanced cyan fluorescent protein (ECFP), bacterial maltose binding periplasmic protein and enhanced yellow fluorescent protein (EYFP) to create a nanosensor which, on binding to maltose, led to more efficient fluorescence resonance energy transfer (FRET) from ECFP to EYFP. Thus, maltose uptake and compartmentation could be monitored in individual *S. cerevisiae* cells by monitoring ECFP/EYFP FRET ratios. Due to their tunability, FPI spectrometers have great potential for use in monitoring of gfp-mutant yeast cells for the detection of intracellular pH using multiwavelength fluorescence measurement. Although the excitation and emission wavelengths are in the operating range of the FPI, in terms of fluorescence detection, use of a single FPI chip as an optical filter is not necessarily sufficient. Cascaded solutions are therefore needed to optimize the rejection ratio of the spectrometer.

Current optical bioprocess monitoring is mostly based on gas concentration measurement (single-point spectroscopy) for monitoring of O_2 and CO_2 as well as turbidity and optical density (NIR range optical absorption measurements at one wavelength). An advantage of FPI is its ability to allow measurement not only of the absorption wavelength but also of a reference wavelength, which could enable internal calibration. Another important aspect is that, typically, colorimeters and spectrometers are used off-line, since especially spectrometers using traditional optical filter wheels are quite large in size as well as expensive. Low-cost miniature MEMS FPI spectrometers could be more easily integrated into on-line measuring sensors at several different locations in the process. However, the most interesting and unique potential of MEMS FPI spectrometers is in imaging; there is currently no process sensing device capable of spectral imaging of cells.

The imaging ability of MEMS FPI spectrometers is demonstrated in the following images of *Saccharomyces cerevisiae* in the different forms in which it is used in the food industry: as granules which store the living cells encapsulated in a body of dried dead cells, and in fresh form. The miniature imaging spectrometer is capable of sweeping the data for the entire spectral range of the FPI across the whole image. Then, using a pointer, the spectra for each individual point can be displayed (see Figure 72 to Figure 75). Alternatively, the image is taken at a couple different filtered wavelengths to emphasize features invisible to the naked eye (Figure 76). Rather than trying to show quantitative information, the purpose of these measurements is to show the versatility of the MEMS FPI measurements.

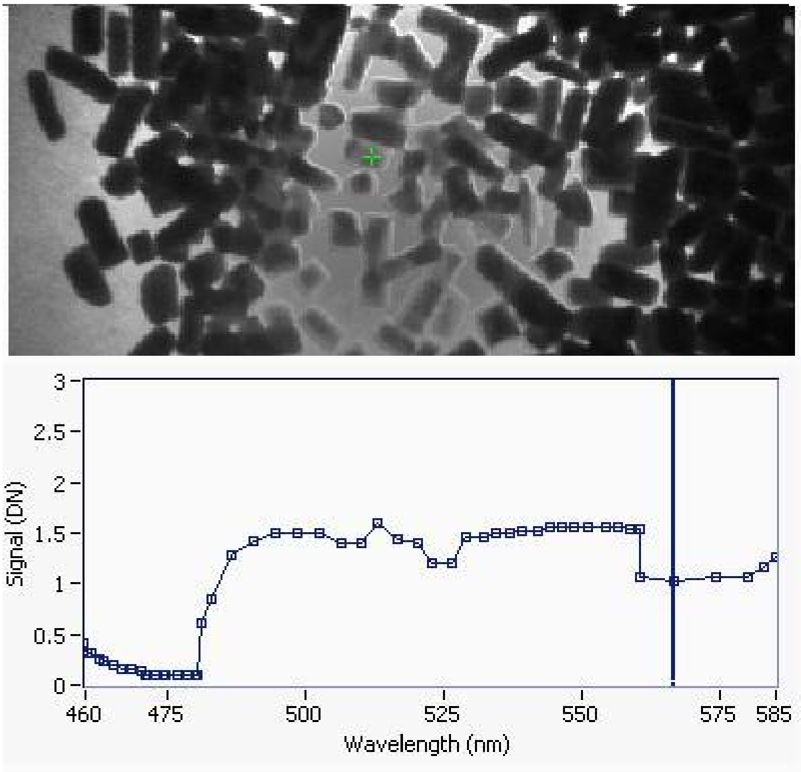

Figure 72. Imaging absorption spectra of dried *Saccharomyces cerevisiae*. The green cross corresponds to the point in the spectral data marked in the chart below.

When comparing the spectra of the seemingly transparent yeast granule in Figure 72 with the spectra of the background LED light in Figure 73, a distinct dip in the wavelength at around 525 nm can be noted, as well as stronger signals below 475 nm and above 560 nm. This could be used to detect different particles in liquid media. Furthermore, comparing the spectra of light transparent yeast in Figure 72 with the apparently non-transparent granule in Figure 74, the spectra show a sharper decline on both sides at around 515 nm.

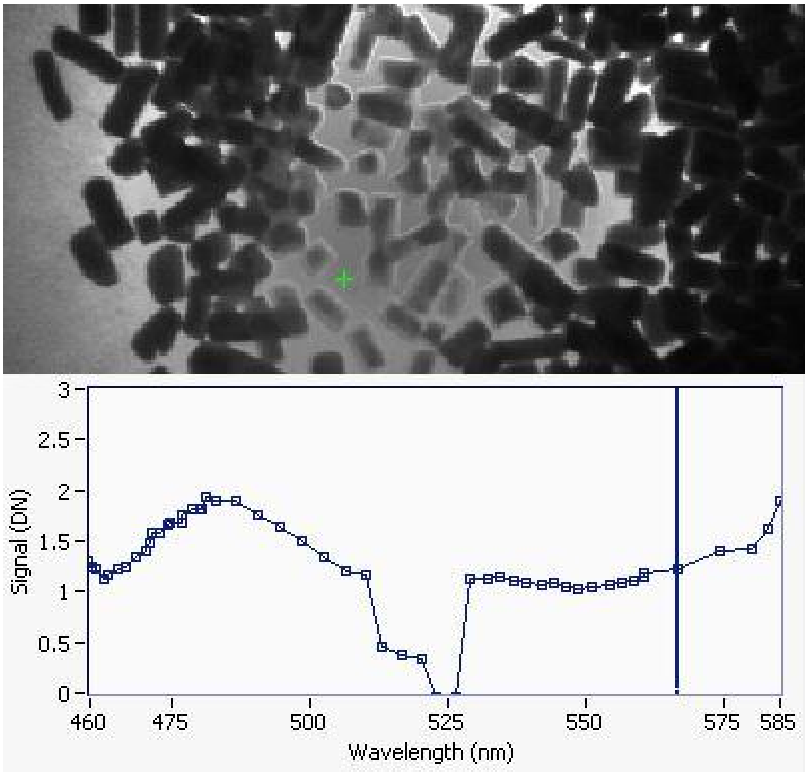

Figure 73. Processed yeast and the background LED light source spectra. The green cross corresponds to the point in the spectral data marked in the chart below.

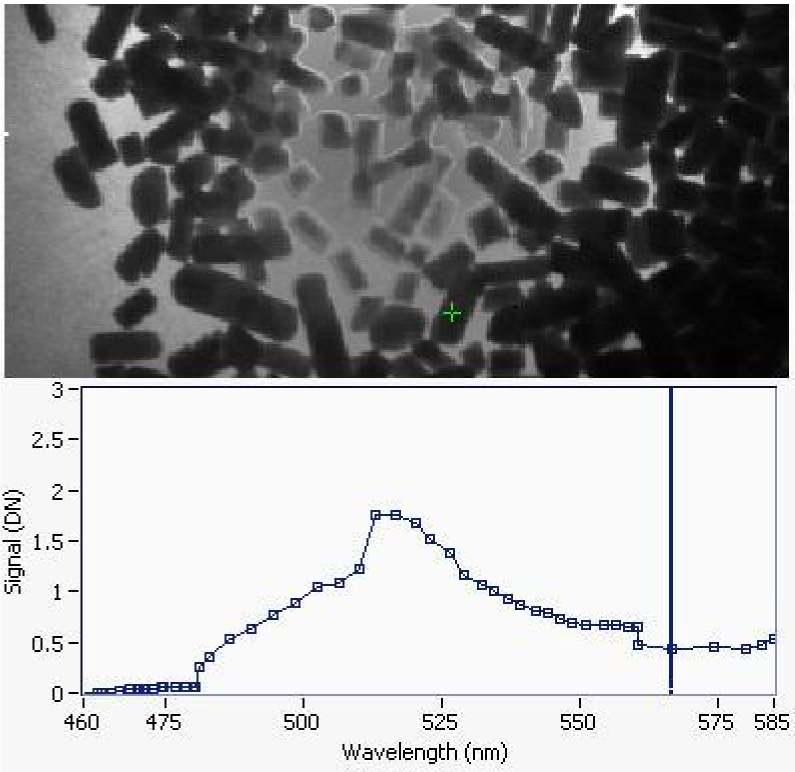

Figure 74. Processed *Saccharomyces cerevisiae*, absorption spectra. The green cross corresponds to the point in the spectral data marked in the chart below.

Moving from the absorption measurements of the previous images to reflection measurement in Figure 75, it can be seen that the spectral intensities vary between granules, possibly indicating slightly different compositions.

Figure 76 shows images of a bulk surface containing live yeast (*Saccharomyces cerevisiae*) filtered at two different wavelengths. Rather than sweeping through the entire spectral range, only two wavelengths are filtered. This helps to emphasize features that are difficult to distinguish without filtering, such as bacterial growth on the surface.

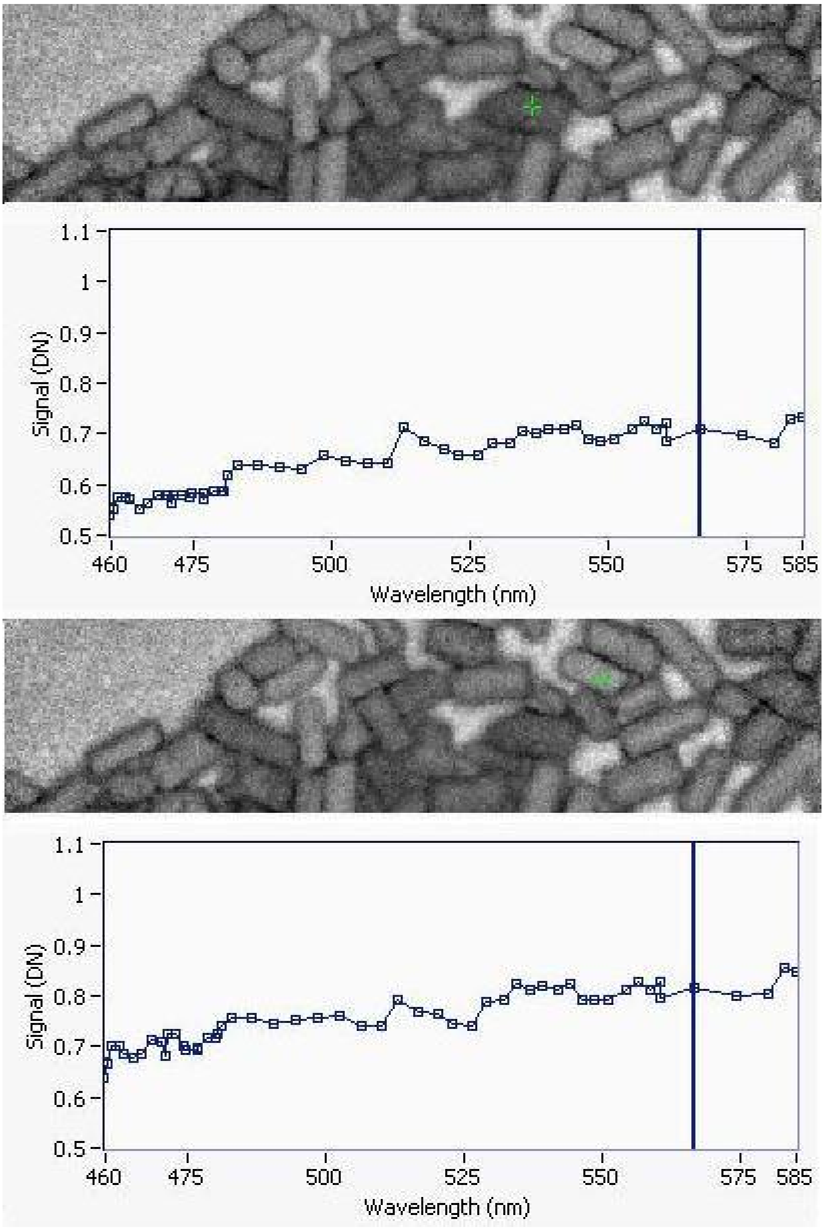

Figure 75. Reflection measurement showing the spectra for two different types of processed yeast.

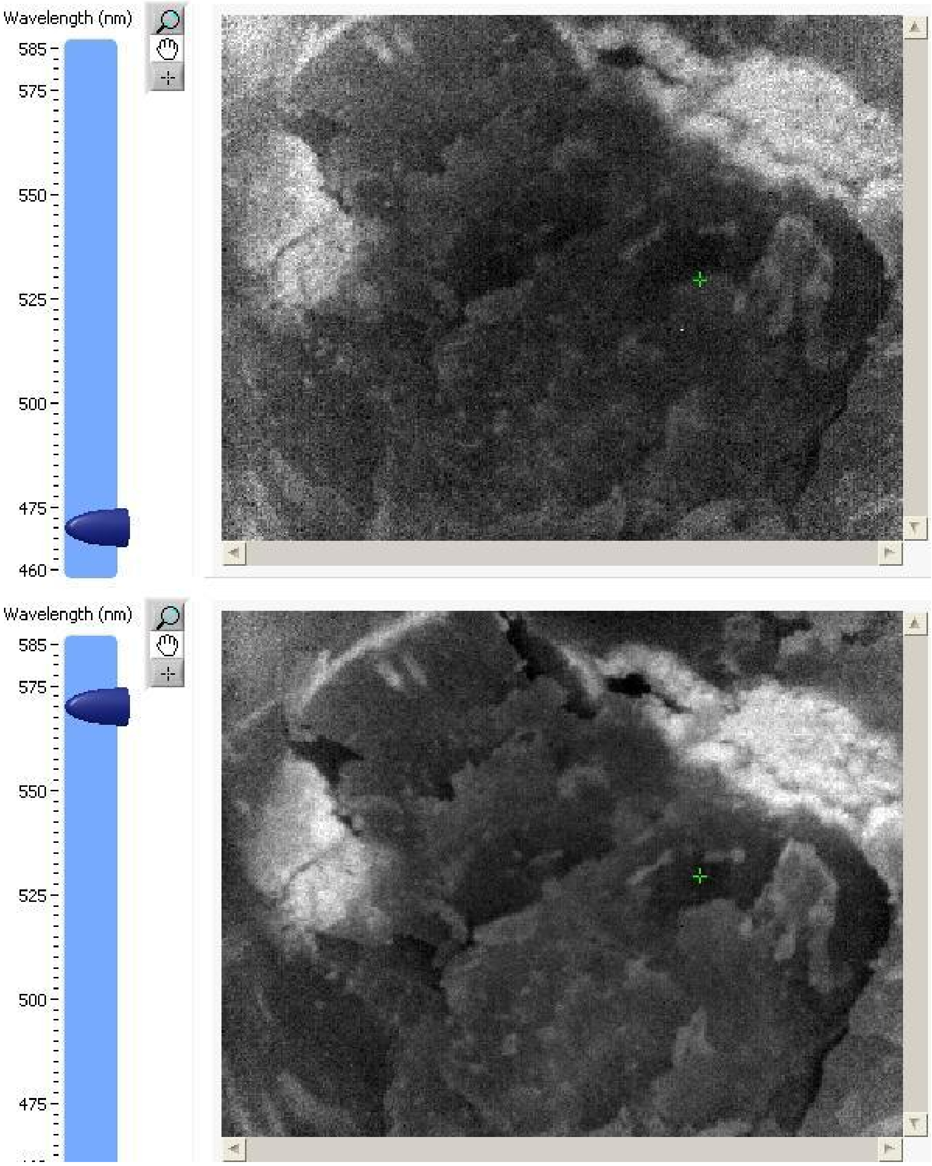

Figure 76. Spectral imaging of a yeast surface containing live Saccharomyces cerevisiae using a blue (470 nm) and green filter (570 nm). The green filter helps emphasize surface features such as white bacteria growth.

5.7 Conclusions

Novel MEMS-based optical filters have been developed for the visible spectral range. These FPIs use ALD Al_2O_3 and TiO_2 as Bragg mirror stack materials, and new sacrificial layer materials, such as polymers and polyimides, are being used to realize novel integrated structures. The low-temperature processing techniques of ALD at T = 110 °C combined with photoresist sacrificial layers have made it possible to realize the first FPI microspectrometer chip for visible light. Polyimide technology with T = 300 °C capability can also be used, giving potential for more versatile combinations of materials. The realized MEMS FPIs have a tunable operating range of 610% of the central wavelength, with a FWHM of ~5 nm, a FSR of ~70 nm and maximum transmission of 65–75%.

Separate MEMS FPIs can be used to realize different types of miniature spectrometers, from single-point pen spectrometers to imaging spectrometers. These spectrometers have high applicability in different types of biological cell measurement, ranging from fluorescence to absorption and reflection spectra measurements, as demonstrated with *Saccharomyces cerevisiae*.

6. Summary and discussion

At first glance, the focus of this thesis may appear to be divided. Closer examination, however, reveals this is not to be the case. Each of the three microsystems and sensors examined here shares the same purpose: extracting information from biological cells. Each method is different, ranging from impedance and thermal analysis to devices capable of spectral measurement, but in the field of micro total analysis systems, this is a clear advantage. Why rely on just one characterization technique when, by developing different miniaturized multiple-technique solutions, we can provide new ways of efficiently obtaining information to complement existing macroscopic/stand-alone methods? MEMS processing and microsystem technologies offer the potential to develop systems that can provide parallel information and, due to their small size and low cost, can be applied with disposable microfluidic platforms and perform on-line analysis from several locations.

This thesis has discussed the literature in the field of micro total analysis systems and the characterization and detection methods employed in them. In current research, much emphasis is placed on the microfabrication of cell handling structures, but the development of the characterization methods is also of importance. For this reason, electrical, thermal and spectral characterization techniques have been introduced and applied in this study using MEMS-based methods. The microsystem for measuring endothelial cell proliferation served its purpose very well. The impedance spectra showed significant differences according to the state of the cells, and it was possible to keep them alive and measure cells that are highly sensitive and difficult to grow to confluence. The MEMS nanocalorimeter, although sensitive, was very difficult to apply to small droplet measurements. The difficulties arising from droplet reproducibility and environmental factors were discussed, and this might be useful for researchers dealing with similar systems.

MEMS FPIs for the visible spectral range are completely new devices with a lot of potential as cell monitoring devices. A miniature imaging spectrometer is an ideal characterization method for any cell researcher, with the non-invasive nature of the optical measurements and the possibility to extract on-line spectral data from the whole surface of a microfluidic platform containing eukaryotic or animal cells. New characterization tools are also needed in the industrial life sciences. As stem cell therapy becomes an everyday treatment method, laboratories may have a new practical tool for monitoring the phases of individual cells in a culture. As bioprocess monitoring in the pharmaceutical industry needs more efficient tools for keeping track of cell production efficiency, these tiny spectrometers might be the answer.

During the last decade, the world of microfluidic total analysis systems has taken a great leap forward. Many different platforms exist for sorting and analyzing cells. Gradually, the emphasis has shifted from silicon-based fluidic systems to plastic platforms, which are much cheaper to produce with roll-to-roll or injection moulding processing technologies. However, many of the characterization techniques used in conjunction with these miniature systems are still in macroscopic form, or cannot be efficiently produced with plastic-based technology. There is a clear need to develop MEMS-based miniaturized characterization methods that can be applied, together or separately, in the analysis of cells in different types of fluidic systems. This thesis has shown the advantages, disadvantages and limits of three important biological cell characterization methods in their miniaturized form.

References

1. A. Rissanen, S. Ostrovidov, E. Lennon, V. Senez, J. Kim, B. Kim, K.S. Furukawa, T. Ushida, Y. Sakai and T. Fujii, "Monitoring capillary endothelial cell culture and capillary formation in a microdevice by impedance spectroscopy measurements", Proceedings of the 3rd IEEE/EMBS Special Topic Conference on Microtechnology in Medicine and Biology (MMB2005), Hawaii, pp. 201–204, 2005.

2. A. Rissanen, J. Saarilahti, E. Rintala, K. Kolari and H. Kattelus, "A Nanocalorimetric microsystem for monitoring yeast cell metabolism", Proceedings of the 20th workshop on micromachining, micro mechanics and micro systems, MME2009, B25, 1–4, pp. 228–231, 2009.

3. A. Rissanen, M. Blomberg, R. Puurunen and H. Kattelus, "ALD thin films in MEMS Fabry-Perot interferometers", 10th International Conference on Atomic Layer Deposition, ALD 2010, Seoul, Korea, June 20–23, 2010.

4. A. Rissanen, A. Akujärvi, J. Antila, M. Blomberg and H. Saari, "MOEMS miniature spectrometers using tuneable Fabry-Perot interferometers", J. Micro/Nanolith. MEMS MOEMS, Vol. 11 (2), pp. 023003/1–6, 2012.

5. A. Rissanen and R. Puurunen," Use of ALD thin film Bragg mirror stacks in tuneable visible light MEMS Fabry-Perot interferometers", Proc. SPIE 8249, pp. 82491A/1–4, 2012.

6. A. Rissanen, U. Kantojärvi, M. Blomberg, J. Antila and S. Eränen "Monolithically integrated microspectrometer-on-chip based on tuneable visible light MEMS FPI", Sensors and Actuators A: Physical (May 2012), doi:10.1016/j.sna.2012.05.023.

7. A. Rissanen, R. Mannila and J. Antila "Bragg reflectors for large optical aperture MEMS Fabry-Perot interferometers", Proc. SPIE 8373, pp. 83732R/1–4, 2012.

8. J. Antila, R. Mannila, U. Kantojärvi, C. Holmlund, A. Rissanen, I. Näkki, J. Ollila and H. Saari, "Spectral imaging device based on a tuneable MEMS Fabry-Perot interferometer", Proc. SPIE 8374, pp. 83740F/1-4, 2012.

9. J.C. McDonald, D.C. Duffy, J.R. Anderson, D.T. Chiu, H. Wu, O.J.A. Schueller and G.M. Whitesides, "Fabrication of microfluidic systems in poly(dimethylsiloxane)", Electrophoresis, Vol. 21, pp. 27–40, 2000.

10. S.K. Sia and G.M. Whitesides, “Microfluidic devices fabricated in Poly(dimethylsiloxane) for biological studies”, Electrophoresis, Vol. 24 (21), pp. 3563–3576, 2003.

11. P. Abgrall and A.-M. Gué, “Lab-on-chip technologies: making a microfluidic network and coupling it into a complete microsystem – a review”, J. Micromech. Microeng., Vol. 17, pp. R15–R49, 2007.

12. A. Rissanen, “Market Research: Microspectrometers for UV, Vis and NIR Spectra”, VTT internal report, pp. 1–35, 2009.

13. A.C. Grayson, R.S. Shawgo, A.M. Johnson, N.T. Flynn, Y. Li, M.J. Cima and R. Langer, “A BioMEMS review: MEMS technology for physiologically integrated devices”, Proceedings of the IEEE, Vol. 92 (1), pp. 6–21, 2004.

14. J. El-Ali, P.K. Sorger and K.F. Jensen, “Cells on chips”, Nature, Vol. 442, pp. 403–411, 2006.

15. H. Andersson and A. van den Berg, “Microtechnologies and nanotechnologies for single-cell analysis”, Current Opinion in Biotechnology, pp. 15, pp. 44–49, 2004.

16. T. Lehnert, M. Gijs, R. Netzer and U. Bischoff, “Realization of hollow SiO_2 nozzles for electrical measurements on living cells”, Applied Physics Letters, Vol. 81 (24), pp. 5063–5065, 2002.

17. A. Han, E. Moss, R. Rabbitt and B. Frazier, “A multi-purpose micro system for electrophysiological analyses of single cells”, Proceedings of MicroTAS 2002, pp. 805–807.

18. Y. Wakamoto, I. Inoue, H. Moriguchi and K. Yasuda, “Analysis of single cell differences by use of an on-chip microculture system and optical trapping”, J. Anal. Chem, Vol. 371, pp. 276–281, 2001.

19. H. Andersson and A. van den Berg, “Microfluidic devices for cellomics: a review”, Sensors and Actuators B, Vol. 92, pp. 315–325, 2003.

20. P. Telleman, U. Larsen, J. Philip and G. Blankenstein, “Cell sorting in microfluidic systems”, microTAS 1998, pp. 39–44.

21. M. Berger, J. Castelino, R. Huang, M. Shah and R.H. Austin, “Design of a microfabricated magnetic cell separator”, Electrophoresis, Vol. 22 (18), pp. 3883–3892, 2001.

22. V.I. Furdui and D.J. Harrison, "Immunomagnetic T cell capture from blood for PCR analysis using microfluidic systems", Lab On Chip, Vol. 4, pp. 614–618, 2004.

23. J. Enger, M. Goksör, K. Ramser, P. Hagberg and D. Hanstorp, "Optical tweezers applied to a microfluidic system", Lab On Chip, Vol. 4, pp. 196–200, 2004.

24. Y. Huang, S. Joo, M. Duhon, M. Heller, B. Wallace and X. Xu, "Dielectrophoretic cell separation and gene expression profiling on microelectronic chip arrays", Anal. Chem., Vol. 74, pp. 3362–3371, 2002.

25. C. Yi, C.-W. Li, S. Ji and M. Yang, "Microfluidics technology for manipulation and analysis of biological cells", Anal. Chim. Acta, Vol. 560, pp. 1–23, 2006.

26. Y. Tanaka, K. Sato, T. Shimizu, M. Yamato, T. Okano and T. Kitamori, "Biological cells on microchips: New technologies and applications", Biosensors and Bioelectronics, Vol. 23, pp. 449–458, 2007.

27. S. Nishimura, S. Yasuda, M. Katoh, K. Yamada, H. Yamashita, Y. Saeki, K. Sunagawa, R. Nagai, T. Hisada and S. Sugiura, "Single cell mechanics of rat cardiomyocytes under isometric, unloaded, and physiologically loaded conditions", Am. J. Physiol. Heart Circul. Physiol., Vol. 287, pp. 196–202, 2004.

28. M. Goto, K. Sato, A. Murakami, M. Toksehi and T. Kitamori, "Development of a microchip-based bioassay system using cultured cells", Anal. Chem., Vol. 74, pp. 2125–2131, 2005.

29. D. Erickson and D. Li, "Integrated microfluidic devices", Analytica Chimica Acta, Vol. 507, pp. 11–26, 2004.

30. R. Kurita, K. Hayashi, X. Fan, K. Yamamoto, T. Kato and O. Niwa, "Microfluidic device integrated with pre-reactor and dual enzyme-modified microelectrodes for monitoring in vivo glucose and lactate", Sens. Actuators B, Vol. 87, pp. 296–303, 2002.

31. I. Moser, G. Jobst and G.A. Urban, "Biosensor arrays for simultaneous measurement of glucose, lactate, glutamate, and glutamine", Biosens. Bioelectron., Vol. 17, pp. 297–302, 2002.

32. J. Wu, J. Suls and W. Sansen, "The glucose sensor integratable in the microchannel", Sens. Actuators B, Vol. 78, pp. 221–227, 2001.

33. M.L. Adams, M. Enzelberger, S. Quake and A. Scherer, "Microfluidic integration on detector arrays for absorption and fluorescence microspectrometers", Sens. Actuators A, Vol. 104, pp. 25–31, 2003.

34. S. Camou, H. Fujita and T. Fujii, “PDMS 2D optical lens integrated with microfluidic channels: principle and characterization”, Lab Chip, Vol. 3, pp. 40–45, 2003.

35. A. Cleary, A. Glidle, P. Laybourn, S. García-Blanco, S. Pellegrini, C. Helfter, G.S. Buller, J.S. Aitchison and J.M. Cooper, “Integrating optics and microfluidics for time-correlated single-photon counting in lab-on-a-chip devices”, Appl. Phys. Lett., Vol. 91, pp. 071123–071123-3, 2007.

36. G. Velve-Casquillas, M. Le Berre, M. Piel and P.T. Tran, “Microfluidic tools for cell biological research”, Nano Today, Vol. 5, pp. 28–47, 2010.

37. Y.S. Liu, T.M. Walter, W.J. Chang, K.S. Lim, L. Yang, S.W. Lee, A. Aronson and R. Bashir, “Electrical detection of germination of viable model *Bacillus anthracis* spores in microfluidic biochips”, Lab on Chip, Vol. 7, pp. 603–610, 2007.

38. M. Varshney, Y. Li, B. Srinivasan and S. Tung, “A label-free, microfluidics and interdigitated array microelectrode-based impedance biosensor in combination with nanoparticles immunoseparation for detection of *Escherichia coli* O157:H7 in food samples”, Sens. Actuators B, Vol. 128, pp. 99–107, 2007.

39. G.B. Salieb-Beugelaar, G. Simone, A. Arora, A. Philippi and A. Amnz, “Latest developments in microfluidic cell biology and analysis systems”, Anal. Chem., Vol. 82, pp. 4848–4864, 2010.

40. G. Huang, Y. Mei, D. Thurmer, E. Coric and O. Schmidt, “Rolled-up transparent microtubes as two-dimensionally confined culture scaffolds of individual yeast cells”, Lab on Chip, Vol. 9, pp. 263–268, 2009.

41. N. Westcott, B. Lamb and M. Yousaf, “Electrochemical and chemical microfluidic gold etching to generate patterned and gradient substrates for cell adhesion and cell migration”, Anal.Chem., Vol. 81 (9), pp. 3297–3303, 2009.

42. L. Segerink, A. Sprenkels, P. Braak, I. Vermes and A. v.d. Berg, “On-chip determination of spermatozoa concentration using electrical impedance measurements”, Lab Chip, Vol. 10, pp. 1018–1024, 2010.

43. A. Shabani, M. Zourob, B. Allain, C. Marquette, M. Lawrence and R. Mandeville, “Bacteriophage-modified microarrays for the direct impedimetric detection of bacteria”, Anal. Chem., Vol. 80 (24), pp. 9475–9482, 2008.

44. S. Hua and T. Pennell, “A microfluidic chip for real-time studies of the volume of single cells”, Lab Chip, Vol. 9 (5), pp. 251–256, 2009.

45. Y. Gao, S. Bhattacharya, X. Chen, S. Barizuddin, S. Gangopadhyay and K. Gillis, "A microfluidic cell trap device for automated measurement of quantal catecholamine release from cells", Lab Chip, Vol. 9 (23), pp. 3442–3446, 2009.

46. S. Zhao, X. Li and Y.-M. Liu, "Integrated microfluidic system with chemiluminescence detection for single cell analysis after intracellular labeling", Anal. Chem., Vol. 81 (10), pp. 3873–3878, 2009.

47. Z. Lin, T. Cherng-Wen, P. Roy and D. Trau, "In-situ measurement of cellular microenvironments in a microfluidic device", Lab Chip, Vol. 9 (23), pp. 257–262, 2008.

48. H. Cho, Y. Zhang, B. Lee, A. Kimteng, J. Bearinger, B. Baker, T. Laurence, S. Lane and I. Lee, "Integrated microfluidic platform with nanoplasmonic aptasensor for on-chip label-free VEGF detection in dynamic tumour microenvironment", Proceedings of micro total analysis systems, Jeju, Korea, pp. 1482–1484, 2009.

49. G. Ferrier, S. Romanuik, D. Thomson, G. Bridges and M. Freeman, "A microwave interferometric system for simultaneous actuation and detection of single biological cells", Lab Chip, Vol. 9 (23), pp. 3406–3412, 2009.

50. G. Charvi, F. Cros and E. Siggia, "A microfluidic device for temporally controlled gene expression and long-term fluorescent imaging in unperturbed dividing yeast cells", PLoS ONE, Vol. 3 (1), pp. e1468:1–12, 2008.

51. A. Funfak, J. Cao, O.S. Wolfbeis, K. Martin and J.M. Köhler, "Monitoring cell cultivation in microfluidic segments by optical pH sensing with a micro flow-through fluorometer using dye-doped polymer particles", Microchimica Acta, Vol. 164 (3–4), pp. 279–286, 2009.

52. A. Huebner, D. Bratton, G. Whyte, M. Yang, A.J. deMello, C. Abell and F. Hollfelder, "Static microdroplet arrays: a microfluidic device for droplet trapping, incubation and release for enzymatic and cell-based assays", Lab Chip, Vol. 9, pp. 692–698, 2009.

53. E. Krommenhoek, M. van Leeuwen, H. Gardeniers, W.M. van Gulik, A. van den Berg, X. Li, M. Ottens, L.A.M. van der Wielen and J.J. Heijnen, "Lab-scale fermentation tests of microchip with integrated electrochemical sensors for pH, temperature, dissolved oxygen and viable biomass concentration", Biotechnology and Bioengineering, Vol. 99 (4), pp. 88–892, 2008.

54. J. Wegener, M. Sieber and H.-J. Galla, “Impedance analysis of epithelial and endothelial cell monolayers cultured on gold surfaces”, J. Biochem. Biophys. Methods, Vol. 32, pp. 151–170, 1996.

55. R. Ehret, W. Baumann, M. Brischwein, A. Schwinde, K. Stegbauer and B. Wolf, “Monitoring of cellular behaviour by impedance measurements on interdigitated electrode structures”, Biosensors et Bioelectronics, Vol. 12 (1), pp. 29–41, 1997.

56. C. Xiao, B. Lachance, G. Sunahara and J.H.T. Luong, “An in-depth analysis of electric cell-substrate impedance sensing to study the attachment and spreading of mammalian cells”, Anal. Chem., Vol. 74, pp. 1333–1339, 2002.

57. K. Asami, E. Gheorghiou and T. Yonezawa, “Real time monitoring of yeast cell division by dielectric spectroscopy”, Biophysical Journal, Vol. 76, pp. 3345–3348, 2005.

58. A. Soley, M. Lecina, X. Gamez, J.J. Cairo, P. Riu, X. Rosell, R. Bragos and F. Godia, “On-line monitoring of yeast cell growth by impedance spectroscopy”, J. Biotechnology, Vol. 118, pp. 398–405, 2005.

59. E. Gheorghiu and K. Asami, “Monitoring cell cycle by impedance spectroscopy”, Bioelectrochemistry and Bioenergetics, Vol. 45, pp. 139–143, 1998.

60. C. Xiao and J.H.T. Luong, “Assessment of cytotoxicity by emerging impedance spectroscopy”, Toxicology and Applied Pharmacology, Vol. 206, pp. 102–112, 2006.

61. K. Cheung, S. Gawad and P. Renaud, “Impedance spectroscopy flow cytometry: on-chip label-free cell differentiation”, Cytometry Part A, Vol. 65A, pp. 124–132, 2005.

62. A. Han and B. Frazier, “Ion channel characterization using single cell impedance spectroscopy”, Lab Chip, Vol. 6, pp. 1412–1414, 2006.

63. A.R.A. Rahman, D.T. Price and S. Bhansali, “Effect of electrode geometry on the impedance evaluation of tissue and cell culture”, Sens. Actuators B, Vol. 127, pp. 89–96, 2007.

64. A.R.A. Rahman, C.M Lo and S. Bhansali, “A microelectrode array biosensor for impedance spectroscopy of human umbilical vein endothelial cells”, Sens. Actuators B, Vol. 118, pp. 115–120, 2006.

65. S. Chung, R. Sudo, I.K. Zervantonakis, T. Rimchala and R.D. Kamm, “Surface-treatment-induced three-dimensional capillary morphogenesis in a microfluidic platform”, Advanced Materials, Vol. 21 (47), pp. 4863–4867, 2009.

66. E.A. Olson, M.Y. Efremov, M. Zhang, Z. Zhang and L.H. Allen, “The design and operation of a MEMS differential scanning nanocalorimeter for high speed heat capacity measurements of ultrathin films”, J. of Microelectromechanical Systems, Vol. 12 (3), pp. 355–364, 2003.

67. W. Lee, W. Fon, B.W. Axelrod and M.L. Roukes, “High-sensitivity microfluidic calorimeters for biological and chemical applications”, PNAS, Vol. 106 (36), pp. 15225–15230, 2009.

68. L. Wang, D.M. Sipe, Y. Xu and Q. Lin, “A MEMS thermal biosensor for metabolic monitoring applications“, J. of Microelectromechanical Systems, Vol. 17 (2), pp. 318–327, 2008.

69. V.L. Singer, L.J. Jones, S.T. Yue and R.P. Haugland, “Characterization of PicoGreen Reagent and Development of a Fluorescence-Based Solution Assay for Double-Stranded DNA Quantitation”, *Analytical Biochemistry*, Vol. 249, Issue 2, pp. 228–238, 1997.

70. M.I. Recht, D. De Bruyker, A.G. Bell, M.V. Wolkin, E. Peeters, G.B. Anderson, A.R. Kolatkar, M.W. Bern, P. Kuhn, R.H. Bruce and F.E. Torres, “Enthalpy array analysis of enzymatic and binding reactions”, Anal. Biochemistry, Vol. 377, pp. 33–39, 2008.

71. J.D. Hybl, S.M. Tysk, S.R. Berry and M.P. Jordan, “Laser-induced fluorescence-cued, laser-induced breakdown spectroscopy biological-agent detection”, Applied Optics, Vol. 45, No. 34, 2006.

72. S. Marose, C. Lindemann, R. Ulber and T. Scheper, “Optical sensor systems for bioprocess monitoring”, TIBTECH, Vol. 17, pp. 30–34, 1999.

73. W. Hellmicha, D. Greifa, C. Pelargusa, D. Anselmettia and A. Ros, “Improved native UV laser induced fluorescence detection for single cell analysis in poly(dimethylsiloxane) microfluidic devices”, J. of Chromatography A, Vol. 1130 (2), pp. 195–200, 2006.

74. H. Teichert, T. Fernholz and V. Ebert, “Simultaneous in situ measurement of CO, H_2O, and gas temperatures in a full-sized coal-fired power plant by near-infrared diode lasers”, *Applied Optics*, Vol. 42 (12), pp. 2043–2051, 2003.

75. Y. Ishihara, H. Masusaki, S.-Q. Wu, K. Matsumoto and T. Kimijima, “Trace Moisture Measurement in HCl Gas by Near-InfraRed Diode Laser Spectroscopy”, International Symposium on Semiconductor Manufacturing, 1995.

76. K.M. Smith and D.A. Newnham, “Near-infrared absorption spectroscopy of oxygen and nitrogen gas mixtures”, Chemical Physics Letters, Vol. 308, No. 1–2, pp. 1–6, 1999.

77. V. Vojinovic, J.M.S. Cabral and L.P. Fonseca, “Real-time bioprocess monitoring Part I: In situ sensors”, Sensors & Actuators B, Vol. 114, pp. 1083–1091, 2006.

78. L. Noui, J. Hill, P.J. Keay, R.Y. Wang, T. Smith, K. Yeung, G. Habib and M. Hoare, “Development of high resolution UV spectrophotometer for at-line monitoring of bioprocesses”, Chem. Eng. and Proc., Vol. 41, pp. 107–114, 2002.

79. J. Antila, A. Miranto, J. Mäkynen, M. Laamanen, A. Rissanen, M. Blomberg, H. Saari and J. Malinen, “MEMS and piezo actuator based fabry-perot interferometer technologies and applications at VTT”, Next-Generation Spectroscopic Technologies III. Proceedings of SPIE – The International Society for Optical Engineering. Vol. 7680, Article number 76800U, 2010.

80. C.B. Ojeda and F. Sanchez, “Recent developments in derivative ultraviolet/visible absorption spectrophotometry”, Analytica Chimica Acta, Vol. 518 (1–2), pp. 1–24, 2004.

81. B.F. Brehm-Stecher and E.A. Johnson, “Single-cell microbiology: tools, technologies and applications“, Microbiology and Molecular Biology Rev., Vol. 68 (3), pp. 539–559, 2004.

82. H.M. Davey and D.B. Kell, “Flow cytometry and cell sorting of heterogeneous microbial populations: the importance of single cell analysis”, Microbial Rev., Vol. 60, pp. 641–696, 1996.

83. J. Zhang, R.E. Campbell, A.Y. Ting and R.Y. Tsien, “Creating new fluorescent probes for cell biology”, Nature Rev., Vol. 3, pp. 906–918, 2002.

84. E. Skibsted, C. Lindemann, C. Roca and L. Olsson, “On-line bioprocess monitoring with a multi-wavelength fluorescence sensor using multivariate calibration”, J. of Biotechnology, Vol. 88, pp. 47–57, 2001.

85. A. Surribas, D. Geissler, A. Gierse, T. Scheper, B. Hitzmann, J.L. Montesinos and F. Valero, “State variables monitoring by in situ multi-wavelength flu-

orescence spectroscopy in heterologous protein production by Pichia pastoris", J. of Biotechnology, Vol. 124, pp. 412–419, 2006.

86. M.B. Haack, A. Eliasson and L. Olsson, "On-line cell mass monitoring of *Saccharomyces cerevisiae* cultivations by multi-wavelength fluorescence", J. of Biotechnology, Vol. 114, pp. 199–208, 2004.

87. H. Carson, "CARBOCAP® – new carbon dioxide sensor – electrically tuneable interferometer for infrared gas analysis", Sensor Review, Vol. 17 (4), pp. 304–306, 1997.

88. R.F. Wolffenbuttel, "MEMS-based optical mini- and microspectrometers for the visible and infrared spectral range", J. Micromech. Microeng., Vol. 15, pp. 145–152, 2005.

89. A. Keating, D. Silva, J. Dell, C. Musca and L. Faraone, "Optical characterization of Fabry-Pérot MEMS filters integrated on tunable short-wave IR detectors", IEEE Photonics Technology Letters, Vol. 18 (9), pp. 1079–1081, 2006.

90. J. Antoszewski, A. Keating, K. Winchester, T. Nguyen, D. Silva, C. Musca, J. Dell and L. Faraone, "Tunable Fabry-Perot filters operating in 3 to 5 μm range for infrared micro-spectrometer applications", Photonics Europe 2006, 3–4 Apr 2006, Strasbourg, France, SPIE Proc. 6186, MEMS, MOEMS, and Micromachining II, pp. 618608-1–618608-9, 2006.

91. M. Bartek, J.H. Correia and R.F. Wolffenbuttel, "Silver-based reflective coatings for micromachined optical filters", J. Micromech. Microeng., Vol. 9, pp. 162–165, 1999.

92. J. Kiihamäki, H. Kattelus, M. Blomberg, R. Puurunen, M. Laamanen, P. Pekko, J. Saarilahti, H. Ritala and A. Rissanen, "Low temperature processes for MEMS device fabrication", Advanced Materials and Technologies for Micro/Nano-Devices, Sensors and Actuators, NATO Science for Peace and Security Series B: Physics and Biophysics, Part 3, pp. 167–178, 2010.

93. M. Blomberg, H. Kattelus and A. Miranto, "Electrically tunable surface micromachined Fabry–Perot interferometer for visible light", Sens. Actuators A, Vol. 162 (2), pp. 184–188, 2010.

94. J. Folkman, "Angiogenesis in cancer, vascular, rheumatoid and other disease", Nat. Med., Vol. 1, pp. 27–31, 1995.

95. O. Cleaver and D. Melton, “Endothelial signalling during development”, Nature Medicine, Vol. 9 (6), pp. 661–668, 2003.

96. M. Rahmanian, H. Pertoft, S. Kanda, R. Christofferson, L. Claesson-Welsh and P. Heldin, “Hyaluronan oligosaccharides induce tube formation of a brain endothelial cell line in vitro”, Experimental Cell Research, Vol. 237, pp. 223–230, 1997.

97. R. Pasqualini, W. Arap and D. McDonald, “Probing the structural and molecular diversity of tumour vasculature”, Trends. Mol. Med., Vol. 8, pp. 563–571, 2002.

98. C.S. Chen, M. Mrksich, S. Huang, G.M. Whitesides and D.E. Ingber, “Geometric control of cell life and death”, Science, Vol. 276, pp. 1425–1428 (1997).

99. J. Glienke, A. Sturz, A. Menrad and K.H. Thierauch, “CRIM1 is involved in endothelial cell capillary formation in vitro and is expressed in blood vessels in vivo”, Mech Dev., Vol. 119 (2), pp. 165–75, 2002.

100. L. Claesson-Welsh, M. Welsh, N. Ito, B. Anand-Apte, S. Soker, B. Zetter, M. O’Reilly and J. Folkman, “Angiostatin induces endothelial cell apoptosis and activation of focal adhesion kinase independently of the integrin-binding motif RGD”, Proc. Natl. Acad. Sci. USA, Vol. 95, pp. 5579–5583, 1998.

101. R. Lin, J. LeCouter, J. Kowalski and N. Ferrara, “Characterization of endocrine gland-derived vascular endothelial growth factor signalling in adrenal cortex capillary endothelial cells”, The Journal of Biological Chemistry, Vol. 277 (10), pp. 8724–8729, 2002.

102. A. Anagnostou, E.S. Lee, N. Kessimian, R. Levinson and M. Steiner, “Erythropoietin has a mitogenic and positive chemotactic effect on endothelial cells”, Proc. Natl. Acad. Sci. USA, Vol. 87, pp. 5978–5982, 1990.

103. K. Jaquet, K. Krause, M. Tawakol-Khodai, S. Geidel and K.-H. Kuck, “Erythropoietin and VEGF exhibit equal angiogenic potential”, Microvascular Research, Vol. 64 (2), pp. 326–333.

104. M. Mrksich, C.S. Chen, Y. Xia, L.E. Dike, D.E. Ingber and G.M. Whitesides, “Controlling cell attachment on contoured surfaces with self-assembled monolayers of alkanethiolates on gold”, Proc. Natl. Acad. Sci. USA, Vol. 93, pp. 10775–1077, 1996.

105. N.i Kataoka, K. Iwaki, K. Hashimoto, S. Mochizuki, Y. Ogasawara, M. Sato, K. Tsujioka and F. Kajiya, “Measurements of endothelial cell-to-cell and

cell-to-substrate gaps and micromechanical properties of endothelial cells during monocyte adhesion", The National Academy of Sciences of the United States of America, Vol. 99 (24), pp. 15638–15643, 2002.

106. F. Asphahani, M. Thein, O. Veiseh, D. Edmondson, R. Kosai, M. Veiseh, J. Xu and M. Zhang, "Influence of cell adhesion and spreading on impedance characteristics of cell-based sensors", Biosens. Bioelectr., Vol. 23, pp. 1307–1313, 2008.

107. A. Bouafsoun, S. Helali, A. Othmane, A. Kerkeni, A.-F. Prigent, N. Jaffrezic-Renault, F. Bessueille, D. Leonard, L. Ponsonnet, "Evaluation of endothelial cell adhesion onto different protein/gold electrodes by EIS", Macrom. Bioscience, Vol. 7, pp. 599–610, 2007.

108. S.-H. Yoon, J. Chang, L. Lin and M. Mofrad, "A biological breadboard platform for cell adhesion and detachment studies", Lab Chip, Vol. 11, pp. 3555–3562, 2011.

109. H.P. Schwan, "Determination of biological impedances", Physical Techniques in Biological Research, Vol. 6 B, pp. 323–408, 1963.

110. L. Wang, B. Wang and Q. Lin, "Demonstration of MEMS-based differential scanning calorimetry for determining thermodynamic properties of biomolecules", Sensors and Actuators B: Chemical, Vol. 134, pp. 953–958, 2008.

111. G.A. Gross and J.M. Köhler, "Fast determination of evaporation enthalpies of solvents and binary mixtures using a microsilicon chip device with integrated thin film transducers", Thermochimica Acta, Vol. 432, pp. 229–240, 2005.

112. C. Larsson, G. Linden, A. Blomberg, C. Niklasson and L. Gustaffson, "Monitoring and control of batch and fed-batch cultures of Saccharomyces cerevisiae by calorimetry", Pure et Appl. Chem., Vol. 65 (9), pp. 1933–1937, 1993.

113. A. Blomberg, C. Larsson and L. Gustafsson, "Microcalorimetric monitoring of growth of *Saccharomyces cerevisiae*: Osmotolerance in relation to physiological state", J. of Bacteriology, Vol. 170 (10), pp. 4562–4568, 1998.

114. M. Krantz, B. Nordlander, H. Valadi, M. Johansson, L. Gustafsson and S. Hohmann, "Anaerobicity prepares Saccharomyces cerevisiae for faster adaptation to osmotic shock", Eukaryotic Cell, Vol. 3 (6), pp. 1381–1390, 2004.

115. P. Duboc, I. Marison and U. von Stockar "Physiology of *Saccharomyces cerevisiae* during cell cycle oscillations", J. of Biotechnology, Vol. 51, pp. 57–72, 1996.

116. P. Duboc, L. Casao-Pereira and U. von Stockar, "Identification and control of oxidative metabolism in Saccharomyces cerevisiae during transient growth using calorimetric measurements", Biotechnology and bioengineering, Vol. 57 (5), pp. 610–619, 1998.

117. P. Duboc and U. von Stockar, "Modeling of oscillating cultivations of Saccharomyces cerevisiae: Identification of population structure and expansion kinetics based on on-line measurements", Chem. Eng. Science, Vol. 55, pp. 149–160, 2000.

118. H. Anuilaniu, L. Gustafsson, M. Rigoulet and T. Nyström, "Protein oxidation in G_0 cells of *Saccharomyces cerevisiae* depends on the state rather than the rate of respiration and is enhanced in pos9 but not yap1 mutants", J. of Biological Chemistry, Vol. 276 (38), pp. 35396–35404, 2001.

119. A. Nilsson, I.-L. Påhlman, P.-Å. Jovall, A. Blomberg, C. Larsson and L. Gustafsson "The catabolic capacity of *Saccharomyces cerevisiae* is preserved to a higher extent during carbon compared to nitrogen starvation", Yeast, Vol. 18, pp. 1371–1381, 2001.

120. L. Guosheng, L. Yi, C. Xiandong, L. Peng, S. Ping and Q. Songsheng, "Study on interaction between T4 phage and *Escherichia coli* B by microcalorimetric method", J. of Virological Methods, Vol. 112, pp. 137–143, 2003.

121. E. Johannessen, J. Weaver, P. Cobbold and J. Cooper, "Heat conduction nanocalorimeter for pl-scale single cell measurements", Applied Physics Letters, Vol. 80 (11), pp. 2029–2031, 2002.

122. J. Saarilahti, "Nanocalorimeter final technical report", VTT internal reports, 2001.

123. H. Välimäki, M. Albers and J. Tuppurainen, "Glucose sensor final report", VTT internal reports, 2004.

124. J. Xu, R. Reiserer, J. Tellinghuisen, J.P. Wikswo and F.J. Baudenbacher, "A microfabricated nanocalorimeter: design, characterization and chemical calibration", Anal.Chem., Vol. 80, pp. 2728–2733, 2008.

125. F. Yi and D.A. La Van, "Nanoscale thermal analysis for nanomedicine by nanocalorimetry", Nanomed. Nanobiotechnol., DOI:10.1002.

126. S. Grabarnik, A. Emadi, H. Wu, G. de Graaf and R.F. Wolffenbuttel, "Microspectrometer with a concave grating fabricated in a MEMS technology", Pro. Chem., Vol. 1, pp. 401–404, 2009.

127. R. Ulber, J.-G. Frerichs and S. Beutel, "Optical sensor systems for bioprocess monitoring", Anal. Bioanal. Chem., Vol. 376, pp. 342–348, 2003.

128. H. Lam and Y. Kostov, "Optical instrumentation for bioprocess monitoring", Adv. Biochem. Engin./Biotechnol., Vol. 116, pp. 1–28, 2009.

129. R.A. Crocomble, "MEMS technology moves process spectroscopy into a new dimension", Spectroscopy Europe, pp. 15–19, July 2004.

130. J.H. Correia, M. Bartek and R.F. Wolffenbuttel, "Bulk-micromachined tunable Fabry–Perot microinterferometer for the visible spectral range", Sens. Actuators A, Vol. 76 (1–3), pp. 191–196, 1999.

131. E. Garmire, "Theory of quarter-wave-stack dielectric mirrors used in a thin Fabry-Perot filter", Applied Optics, Vol. 42 (27), pp. 5442–5449, 2003.

132. S.D. Senturia, "Microsystems Design", Kluwer Academic Publishers, Boston, pp. 249–259, 2000.

133. E.K. Chan and R.W. Dutton, "Electrostatic micromechanical actuator with extended range of travel", J. of Microelectromechanical Systems, Vol. 9 (3), pp. 321–328, 2000.

134. R.L. Puurunen, "Surface chemistry of atomic layer deposition: A case study for the trimethylaluminum/water process", Journal of Applied Physics, Vol. 97, pp. 1–52, 2005.

135. R.L. Puurunen, M. Blomberg and H. Kattelus, "ALD layers in MEMS fabrication", 9th International Conference on Atomic Layer Deposition, ALD 2009, Monterey, California, July 19–22, 2009 Technical Program et Abstracts. American Vacuum Society AVS (2009), 33.

136. M. Fehr, W.B. Brommer and S. Lalonde, "Visualization of maltose uptake in living yeast cells by fluorescent nanosensors", Proc. Nat. Acad. Sci. USA, Vol. 99, pp. 9846–9851, 2002.

Series title and number
VTT Science 14

Title	**Microsystems for Biological Cell Characterization**
Author(s)	Anna Rissanen
Abstract	This thesis describes three techniques for the characterization of living cells using micro-electro-mechanical systems (MEMS) based devices. The study of cellular function and structure is essential for bioprocess control, disease diagnosis, patient treatment and drug discovery. Microsystem technology enables characterization of very small samples, minimal use of expensive reagents, testing of multiple samples in parallel, and point-of-care testing, all of which increase throughput and reduce the analysis cost. The three characterization techniques presented in this thesis could be integrated into a microfluidic cellular total analysis system to obtain complementary information of cellular function. The first part of the thesis presents the characterization of bovine adrenal cortex capillary endothelial cells by impedance spectroscopy in a microsystem which was realized using microfabrication techniques. The microsystem consists of a small-volume cell culture area defined on PDMS walls on a glass substrate with gold electrodes coated with a self-assembled monolayer to enable cell attachment. As the main result, it was possible to monitor the capillary formation of BACC endothelial cells in a microsystem using impedance spectroscopy. The second part describes calorimetric characterization of *Saccharomyces cerevisiae* yeast cells using a MEMS-based nanocalorimetric microsensor. The cells are introduced to the sensor membrane in small droplets (~1 µl), and the sensor thermopile voltage output is compared to the output of the reference water droplet to extract the effect of sample evaporation. The third part describes the design, process integration and fabrication of an electrically tunable Fabry-Perot interferometer (FPI) monolithically integrated on a photodiode for visible spectrum measurements. The options for the process integration of separate FPI optical filters are presented. The application of miniature spectrometers based on MEMS FPI technology in biological cell characterization is discussed.
ISBN, ISSN	ISBN 978-951-38-7475-9 (soft back ed.) ISSN 2242-119X (soft back ed.) ISBN 978-951-38-7931-0 (URL: http://www.vtt.fi/publications/index.jsp) ISSN 2242-1203 (URL: http://www.vtt.fi/publications/index.jsp)
Date	October 2012
Language	English, Finnish abstract
Pages	130 p.
Keywords	BioMEMS, impedance spectroscopy, MEMS nanocalorimeter, Fabry-Perot interferometer, microspectrometers, *Saccharomyces cerevisiae*, yeast, cell measurement
Publisher	VTT Technical Research Centre of Finland P.O. Box 1000, FI-02044 VTT, Finland, Tel. 020 722 111

Julkaisun sarja ja numero

VTT Science 14

Nimeke	**Mikrosysteemit solujen karakterisointiin**
Tekijä(t)	Anna Rissanen
Tiivistelmä	Tämä väitöskirja käsittää kolme erilaista mikroelektromekaanisiin systeemeihin (MEMS) perustuvaa menetelmää elävien solujen karakterisoimiseksi. Solutoimintojen ja rakenteen karakterisointi on tärkeää bioprosessien kontrolloinnissa, sairauksien diagnosoinnissa, potilaiden hoidossa ja uusien lääkkeiden tutkimuksessa. Mikrosysteemitekniikka mahdollistaa hyvin pienien näytteiden yhtäaikaisen karakterisoinnin, minimoi kalliiden reaktioaineiden käytön ja paikan päällä testauksen ja lisää näin läpimenoa ja vähentää analyysin hintaa. Nämä kolme tässä väitöskirjassa esitettyä karakterisointitekniikka on mahdollista yhdistää osaksi mikrofluidistista solujen kokonaisanalyysisysteemiä ja saada näin toinen toistaan täydentävää mittausinformaatiota solujen toiminnoista. Ensimmäinen osa käsittää naudan lisämunuaiskuoren kapillaariendoteelisolujen (BACC) monitoroinnin impedanssispektrometrialla mikrosysteemissä, joka on toteutettu mikrotyöstötekniikoita käyttäen. Mikrosysteemi koostuu pienen tilavuuden PDMS (polydimetyylisiloksaani) seinillä rajatusta soluviljelyalueesta lasialustalle, johon on kuvioitu kultaelektrodit ja SAM-kalvo solujen kiinnittymisen mahdollistamiseksi. Keskeisenä tuloksena voitiin todeta, että BACC-endoteelisolujen kapillaarien muodostumista oli mahdollista monitoroida mikrosysteemissä käyttäen impedanssispektrometriaa. Toisessa osiossa kuvataan *Saccharomyces cerevisiae* -hiivasolujen kalorimetristä monitorointia käyttäen nanokalorimetristä MEMS mikroanturia. Solut tuodaan anturille pienissä pisaroissa (~µl) ja anturin termoparin jänniteulostuloa verrataan referenssinestepisaran jännitteeseen jotta haihtumisen aiheuttama lämpöhäviö voidaan kompensoida. Kolmas osio käsittää näkyvän valon spektrin mittaamiseen tarkoitetun monoliittisesti fotodiodille integroidun sähköisesti säädettävän Fabry-Perot-interferometrin (FPI) suunnittelun, prosessi-integraation ja valmistuksen. Myös erillisten FPI-suodattimien prosessi-integraation vaihtoehdot esitetään. Mikromekaanisiin FPI-suodattimiin perustuvien miniatyyrispektrometrien soveltamista biologisiin solumittauksiin käsitellään ja havainnollistetaan esimerkein.
ISBN, ISSN	ISBN 978-951-38-7475-9 (nid.) ISSN 2242-119X (nid.) ISBN 978-951-38-7931-0 (URL: http://www.vtt.fi/publications/index.jsp) ISSN 2242-1203 (URL: http://www.vtt.fi/publications/index.jsp)
Julkaisuaika	Lokakuu 2012
Kieli	Englanti, suomenkielinen tiivistelmä
Sivumäärä	130 s.
Avainsanat	BioMEMS, impedance spectroscopy, MEMS nanocalorimeter, Fabry-Perot interferometer, microspectrometers, *Saccharomyces cerevisiae*, yeast, cell measurement
Julkaisija	VTT PL 1000, 02044 VTT, Puh. 020 722 111

Microsystems for Biological Cell Characterization

During the last decade, the world of microfluidic total analysis systems has taken a great leap forward. Various approaches exist for mechanical sorting and manipulation of cells within microsystems. However, many of the characterization techniques used in conjunction with these miniature systems are still in macroscopic form. There is a need to develop miniaturized characterization methods that can be applied, together or separately, in the analysis of cells in different types of fluidic systems, as well as increase understanding of their advantages and disadvantages. This thesis studies microsystems that use different types of characterization techniques for cell analysis and monitoring. The topic is interdisciplinary, ranging in scope from the optical, electrical and materials science of microelectromechanical systems (MEMS) and sensor measurement technology to cell biology. In addition, the devices and characterization methods also represent different technologies and approaches.

Topics covered within this thesis include impedance spectroscopy characterization of bovine adrenal cortex capillary endothelial cells within a microsystem specifically developed for the cell culture and measurements, calorimetric characterization of *Saccharomyces cerevisiae* yeast cells using a MEMS-based nanocalorimetric microsensor, as well as the design, process integration and fabrication of electrically tunable MEMS Fabry-Perot interferometers (FPIs) utilized in miniature spectrometers with potential capability of optical characterization of cells.

ISBN 978-951-38-7475-9 (soft back ed.)
ISBN 978-951-38-7931-0 (URL: http://www.vtt.fi/publications/index.jsp)
ISSN 2242-119X (soft back ed.)
ISSN 2242-1203 (URL: http://www.vtt.fi/publications/index.jsp)